

The
**PHILOSOPHICAL
MAGAZINE**

FIRST PUBLISHED IN 1798

L. 42 SEVENTH SERIES No. 329

June, 1951

*A Journal of
Theoretical Experimental
and Applied Physics*

EDITOR

PROFESSOR N. F. MOTT, M.A., D.Sc., F.R.S.

EDITORIAL BOARD

SIR LAWRENCE BRAGG, O.B.E., M.C., M.A., D.Sc., F.R.S.

ALLAN FERGUSON, M.A., D.Sc.

SIR GEORGE THOMSON, M.A., D.Sc., F.R.S.

PROFESSOR A. M. TYNDALL, C.B.E., D.Sc., F.R.S.

PRICE 12s. 0d.

Annual Subscription £6 0s. 0d. payable in advance.

UNIVERSITY LIBRARY
JUL 16 1951

Early Scientific Publications



DIARY OF ROBERT HOOKE M.A., M.D., F.R.S.

1672-1680

25/-

net

Edited by **H. W. ROBINSON** and **W. ADAMS**
Recommended for publication by the Royal Society,
London

"This vivid record of the scientific, artistic and social activities of a remarkable man during remarkable years has too long remained in obscurity."—Extract from foreword by Sir Frederick Gowland Hopkins, O.M., President of the Royal Society.

MATHEMATICAL WORK OF JOHN WALLIS, D.D., F.R.S.

12/6

net

By **J. F. SCOTT, Ph.D., B.A.**

"His work will be indispensable to those interested in the early history of The Royal Society. I commend to all students of the Seventeenth Century, whether scientific or humane, this learned and lucid book."—Extract from foreword by Prof. E. N. da C. Andrade, D.Sc., Ph.D., F.R.S.
Recommended for publication by University of London

CORRESPONDENCE AND PAPERS OF EDMOND HALLEY

21/-

net

Arranged and Edited by **EUGENE FAIRFIELD MACPIKE**

First published on behalf of The History of Science Society by Oxford University Press. Now re-issued by Taylor & Francis, Ltd.

MEMOIRS OF SIR ISAAC NEWTON'S LIFE

5/-

net

By **WILLIAM STUKELEY, M.D., F.R.S., 1752**

From an Original Manuscript

Now in the possession of the Royal Society, London

HEVELIUS, FLAMSTEED AND HALLEY

12/6

net

Three Contemporary Astronomers and their Mutual Relations

By **EUGENE FAIRFIELD MACPIKE**

Published by arrangement with The History of Science Society

Established
over 150 years

TAYLOR & FRANCIS, LTD.
RED LION COURT, FLEET ST., LONDON E.C.
PRINTERS & PUBLISHERS OF SCIENTIFIC BOOKS

LX. *A Mechanism for the Growth of Deformation Twins in Crystals.*

By A. H. COTTRELL and B. A. BILBY,
Department of Metallurgy, University of Birmingham *.

[Received February 24, 1951.]

SUMMARY.

The principal difficulty in developing a dislocation theory of mechanical twinning has been to explain how a twin grows through a finite thickness of crystal. By extending the recent theory of slip bands, proposed by Frank and Read, it is possible to show that a dislocation can move steadily from plane to plane in a crystal. A theory of mechanical twinning, which is formally analogous to Frank's theory of crystal growth, can then be developed. The theory is applied to the body-centred and face-centred cubic lattices.

§ 1. INTRODUCTION.

THE idea that mechanical twinning takes place in crystals by the continuous growth on an atomic scale of twinned material, and not by the simultaneous movement of all the atoms involved, has often been suggested; for example, by Frenkel and Kontorova (1939), Seitz and Read (1941), and Frank and van der Merwe (1949). The general arguments for a dislocation mechanism of mechanical twinning are the same as those for the dislocation theory of slip. First, it is scarcely believable that the atoms concerned should all move simultaneously, and second, twinning takes place at stresses far below the theoretical shear strength of a perfect lattice.

In some examples of mechanical twinning the atomic movements required to produce the twinned lattice from the original one are more complicated than those that produce slip. The movements can usually be described in terms of a homogeneous shear of all the atoms involved, together with localized rearrangements in which neighbouring atoms move in different directions from one another. The twinning shear of one plane of atoms over another can be produced by the movement in the twinning plane of a dislocation of the usual type, but with a Burgers vector that is not a lattice vector (an "imperfect dislocation"). On the other hand, the localized rearrangements cannot be described formally in terms of a dislocation. In practice, of course, these rearrangements will usually be produced automatically by the passage of the dislocation, because the arrangement of atoms is almost certainly mechanically unstable until the transformation is completed. In this paper a dislocation mechanism is suggested for the shear component of the twinning movements, and the extension of the theory to those cases where localized rearrangements also

* Communicated by the Authors.

take place is not considered. The theory is thus most directly applicable to those twinning deformations, such as that of α -iron, or shear transformations where the atom movements are completely resolvable into homogeneous shears on crystallographic planes.

It is usually not difficult to discover a suitable imperfect dislocation to cause the required shear of neighbouring planes as it passes between them. The important problem is to explain how twinning develops homogeneously through successive lattice planes, in contrast to the behaviour in slip, where the deformation is concentrated on a single plane. In terms of dislocations the homogeneous twinning shear requires either an avalanche of dislocations, one on every lattice plane without exception, or the motion of a single dislocation successively from one plane to the next in a regular manner. It is the purpose of this paper to show that the latter process can occur naturally in certain crystals containing dislocations.

§ 2. THE POLE MECHANISM.

Frank and Read (1950) have recently proposed a mechanism whereby unlimited amounts of slip can be produced by a single dislocation moving in a single slip plane. The essential idea is that the line of this dislocation does not lie for the whole of its length in the slip plane; at some point, or at two points if the line does not extend to the surface of the crystal, the line turns out of the plane along some intersecting direction. Thus consider a dislocation line of arc element $d\mathbf{s}$ and Burgers vector \mathbf{b} which, for part of its length, lies in a slip plane of unit normal \mathbf{v} , where $\mathbf{b} \cdot \mathbf{v} = 0$. Then repeated rotation in the slip plane of this part of the line about the interior point (or points) of emergence of the line from the plane can cause an amount of slip on the plane which is limited only by boundary conditions. This process requires the part of the dislocation line that leads out of the slip plane (which we shall call the "pole" dislocation) to be in some way anchored; the moving part of the line ("sweeping" dislocation) then forms a plane spiral about the fixed point of emergence.

It is not essential that the pole dislocation should end in the slip plane. Consider for example three straight dislocation lines lying along \mathbf{s}_1 , \mathbf{s}_2 , \mathbf{s}_3 and meeting at a point O (fig. 1). Frank (private communication) calls such a meeting of dislocations a "node". A convenient convention, due to Frank, for defining the Burgers vectors of dislocations at a node is to look outwards from the nodal point O and describe a closed clockwise circuit round each line; in the case of an imperfect dislocation the circuit should begin in the stacking fault associated with the dislocation. The same circuit repeated in the lattice as it existed before the dislocation was made will not be closed and the Burgers vector of the dislocation is the additional displacement needed to close it. With this convention the Burgers vectors \mathbf{b}_1 , \mathbf{b}_2 , \mathbf{b}_3 of the lines meeting at O must satisfy the relation

$$\sum_{n=1}^3 \mathbf{b}_n = 0. \quad \dots \quad \dots \quad \dots \quad \dots \quad \dots \quad (1)$$

If dislocation 3 is perfect it can move in any plane ν where $\mathbf{b}_3 \cdot \nu = 0$, and if neither \mathbf{s}_1 nor \mathbf{s}_2 lie in the plane ν then \mathbf{s}_3 can spiral in this plane, producing repeated increments of slip on it. It is essential, if this process is to produce a simple multiplication of slip on this plane, that the vectors \mathbf{b}_1 and \mathbf{b}_2 should also lie in the plane. However, relation (1) requires only that

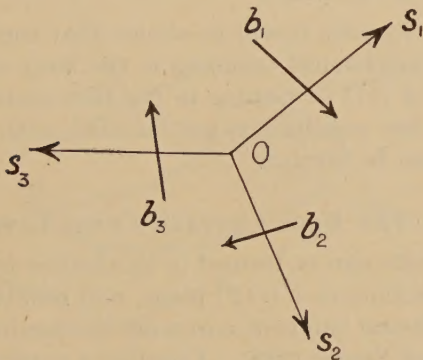
$$\nu \cdot (\mathbf{b}_1 + \mathbf{b}_2) = 0, \dots \dots \dots \quad (2)$$

and interesting topological consequences follow if we extend Frank and Read's mechanism to the case where \mathbf{b}_1 and \mathbf{b}_2 do not lie in the plane ν . There is then a component

$$\mathbf{t} = (\mathbf{b}_1 \cdot \nu) \nu = (-\mathbf{b}_2 \cdot \nu) \nu, \dots \dots \dots \quad (3)$$

perpendicular to the plane, and the dislocation line \mathbf{s}_3 is displaced by \mathbf{t} for every complete revolution that it makes about \mathbf{s}_1 . Hence, instead of repeated slip on the original plane ν , a slip \mathbf{b}_3 takes place on each of a

Fig. 1.



series of planes parallel to ν and spaced \mathbf{t} apart. The sweeping dislocation climbs, as it were, round the helical surface that is formed because the Burgers vector of the pole dislocation has a component perpendicular to the sweeping plane. The shear deformation which results is thus of the homogeneous type that occurs in twinning and shear transformations.

A mechanical twin or transformed structure generated by this process will build up conically in a way similar to the pyramids suggested by Frank (1949) in his theory of crystal growth, and the sweeping dislocation will rapidly assume the form of a helix, since the parts near the pole will have the highest angular velocity. The formation of twins from sweeping dislocations connecting two poles is also to be expected. There is thus a close formal correspondence with the theory of crystal growth, the terraced steps of the latter being replaced in the present case by imperfect dislocations separating the transformed and untransformed material.

The usual elastic interactions will occur between the sweeping dislocations and other singularities in the crystal, while the final shape and size of the twinned piece of the crystal will be determined by its strain energy and by the positions of large obstacles in the material.

If mechanical twinning in a given crystal is to occur by this process, several conditions must be satisfied :

1. The sweeping dislocation must produce the right shear displacement to generate the transformed structure on the sweeping plane.
2. The Burgers vector of the pole dislocation must have a component perpendicular to the sweeping planes that is equal to the spacing of these planes.
3. The pole dislocation must be anchored strongly enough to prevent it from moving under the stress causing the sweeping dislocation to move. Strong anchoring is ensured if the pole dislocation is of the sessile type.
4. The sweeping and pole dislocations, together perhaps with other associated dislocation lines, must form a node and in this node the sweeping dislocation must be free to move in a sweeping plane which is intersected by the pole.

In the following sections it will be shown that these conditions can be satisfied for {112} mechanical twinning in the body-centred cubic lattice, while in the case of {111} twinning in the face-centred cubic lattice the second part of the last condition is not satisfied, with the result that only monolayer twins can be formed.

§ 3. THE BODY-CENTRED CUBIC LATTICE.

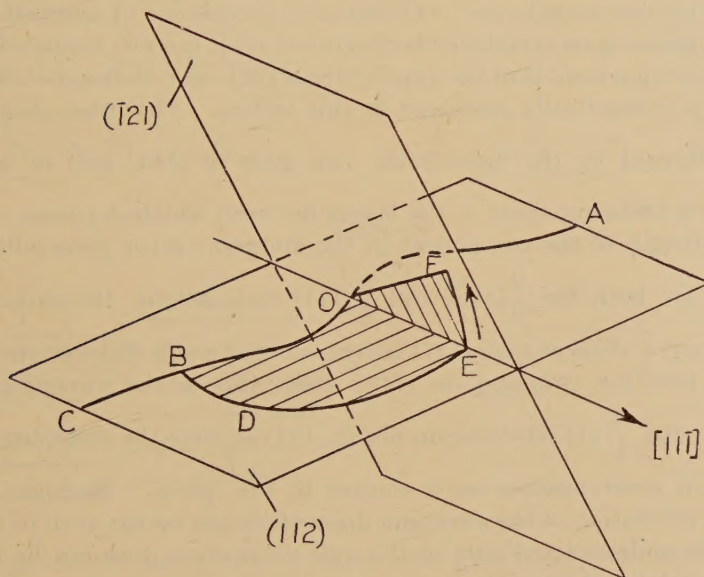
A twinned structure can be formed in this lattice by a shear of $1/\sqrt{2}$ or $\sqrt{2}$ in a $\langle 111 \rangle$ direction on a {112} plane, and reliable evidence exists to show that the Neumann bands in α -iron are mechanical twins of this type (*e.g.* Smith, Dee and Young 1928). Consider a portion of a line of perfect dislocation of $\frac{a}{2}[111]$ type which lies in (112) but not along [111]. Then (fig. 2), if sufficient energy is available from external sources, a dissociation of the type :

$$\frac{a}{2}[111] \rightarrow \frac{a}{3}[112] + \frac{a}{6}[11\bar{1}] \quad \dots \quad (4)$$

can occur along a length BO of the line, forming nodes at B and O. Suppose for definiteness that the Burgers vectors of the lines OA, OB and OFEDB are, using the nodal convention of §2, $\frac{a}{2}[111]$, $-\frac{a}{3}[112]$ and $-\frac{a}{6}[11\bar{1}]$. Then the line OB is pure edge and sessile, while the line BDEO, in moving away from OB, has formed a sheet of stacking fault in (112). This stacking fault is, in fact, the simplest possible on the (112) planes if the planes are to retain the original packing of nearest neighbours,

and corresponds to the insertion of two fault planes in the (112) stacking sequence ; this sequence is a congruence to modulus 6 and the stacking fault is of the type 12345616123456. Since the line BDEO is glissile it may in its motion become pure screw ; a length OE can then move into either ($\bar{1}21$) or ($2\bar{1}1$), since it is a twinning dislocation for these planes. On account of the unidirectional character of the twinning movement the line OE must move so that the new stacking faults generated on ($\bar{1}21$) or ($2\bar{1}1$) make acute angles with the original fault in (112). The node at O can now produce twinning if OF sweeps about AOB as pole, since the components of the Burgers vector of OA perpendicular to ($\bar{1}21$) and ($2\bar{1}1$) are $\frac{a}{6}[\bar{1}21]$ and $\frac{a}{6}[2\bar{1}1]$, respectively. The sweeping dislocation thus

Fig. 2.



Dissociation in the body-centred cubic lattice of a unit dislocation. AO=unit dislocation $\frac{a}{2}[111]$; OB=sessile dislocation $-\frac{a}{3}[112]$; OFEDB=twinning dislocation $-\frac{a}{6}[11\bar{1}]$.

climbs along OB into the stacking fault as it rotates ; it can pass through the latter since this is identical with a mono-layer twin on (112) and the twins on the three planes (112), ($\bar{1}21$) and ($2\bar{1}1$) have the same direction of twinning movement. The movements possible at the node O have been described explicitly but complementary movements can also occur at B, again causing a macroscopic twin on ($\bar{1}21$) or ($2\bar{1}1$) to grow into the stacking fault.

§ 4. THE FACE-CENTRED CUBIC LATTICE.

The analogous dissociation in this case is

$$\frac{a}{2}[110] \rightarrow \frac{a}{3}[111] + \frac{a}{6}[1\bar{1}\bar{2}] \quad \dots \dots \dots \quad (5)$$

Here, $\frac{a}{2}[110]$ represents a unit, perfect dislocation; the line of this dislocation could lie in any direction and the two $\{111\}$ type slip planes on which it could glide are $(1\bar{1}1)$ and $(\bar{1}11)$. When the line lies in the (111) plane the above dissociation is possible because $\frac{a}{3}[111]$ represents a sessile dislocation in this plane. It forms the boundary of a fault, such as 1231231312312, in the stacking of successive (111) layers on one another. This fault has low energy because it preserves the close-packed arrangement of nearest neighbours; the frequent occurrence of annealing twins on $\{111\}$ planes in recrystallized face-centred cubic metals, across which the stacking arrangement is of the type 12312321321, also shows that this type of fault is energetically preferred in this lattice. The other dislocation, $\frac{a}{6}[1\bar{1}\bar{2}]$, formed by the dissociation can glide in (111) and in so doing produces a twinning shear of the layers between which it passes.

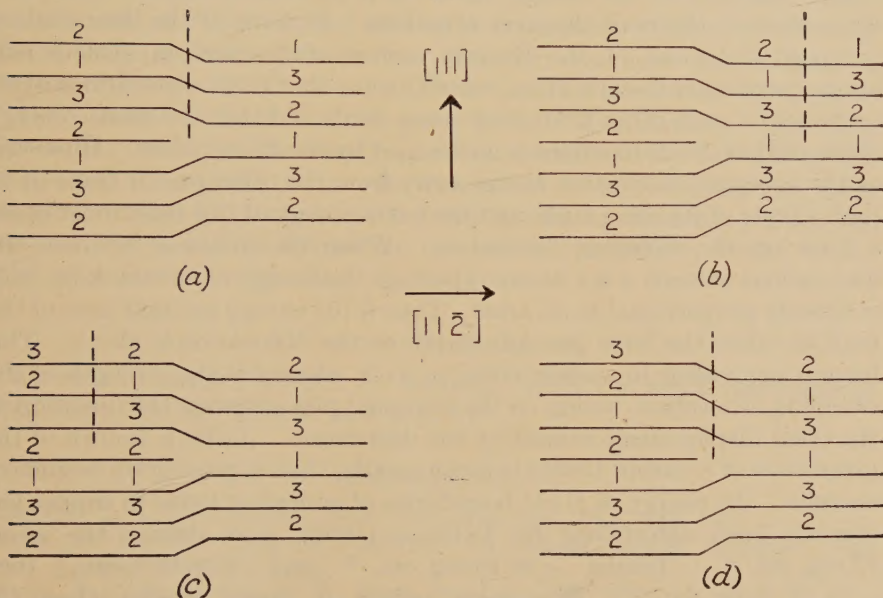
The strength of the component of the Burgers vector perpendicular to (111) is, for both the $\frac{a}{2}[110]$ and $\frac{a}{3}[111]$ dislocations, the same as the spacing $a/\sqrt{3}$ of successive (111) layers, so that these dislocations form a suitable pole for twinning on (111) when this is the sweeping plane. However, the $\frac{a}{3}[111]$ dislocation lies in (111) so that the sweeping $\frac{a}{6}[1\bar{1}\bar{2}]$ dislocation must meet it as it rotates in this plane. Because of this, only one revolution of the sweeping dislocation can occur, even in the case where the undissociated part of the unit dislocation does not lie in (111) and the nodal point can then act as a point of emergence from the plane. Thus only a monolayer stacking fault can be formed.

That repeated rotation of the sweeping dislocation is impossible may be seen by considering fig. 3. These diagrams show a set of (111) planes viewed from the side, perpendicularly to $[1\bar{1}\bar{2}]$. Diagram (a) shows the unit $\frac{a}{2}[110]$ dislocation before it dissociates; here the numbers refer to the stacking positions of the (111) layers and the broken vertical line is a boundary across which the stacking numbers are changed. By crossing this line from left to right the number of a layer is increased by 2; since the sequence 123123 forms a congruence to modulus 3, then $4 \equiv 1$ and $5 \equiv 2$, etc. The dissociation occurs when the broken line is moved to the right, as in diagram (b). The sessile $\frac{a}{3}[111]$ dislocation remains in the site

of the original dislocation, while the sweeping $\frac{a}{6} [1\bar{1}\bar{2}]$ dislocation is situated at the lower end of the broken line. In the region between these dislocations the stacking sequence contains the fault 12313123.

As the sweeping dislocation moves away it extends this stacking fault between the central (111) layers. By rotating about the point of emergence it eventually approaches the sessile dislocation again, and from the left-hand side. It reappears here between either the central 2 and 3, or 1 and 2, layers, respectively, according as the undissociated section of the dislocation line emerges from the (111) plane on its lower or upper side. Diagram (c) illustrates the first of these possibilities. The final diagram

Fig. 3.



Stages in the formation of a stacking fault on (111) by the dissociation of an $\frac{a}{2}[110]$ unit dislocation in the face-centred cubic lattice.

shows the arrangement when the sweeping dislocation has rejoined the sessile one, after forming a stacking fault over the entire plane. The sweeping dislocation cannot continue the same movement further because if it did, it would then be making a second circuit between the same layers, and would create a fault of the type 1231123 in which nearest neighbours are not packed correctly.

The single rotation just described is the only possible motion for the sweeping dislocation. The dislocation cannot move towards the left, starting from its position in diagram (a), because this would create a fault of the forbidden type (either 2311231 or 2312231) between the central (111) half-layer and one of its neighbours. Furthermore, it cannot move in any

other type of {111} plane because it can only glide into a different plane from (111) when it is of pure screw type, *i. e.* when its line lies along [112], and {111} planes do not intersect one another along this direction.

It follows that this pole mechanism produces only monolayer stacking faults in the face-centred cubic lattice, and cannot cause the growth of mechanical twins. It is interesting that, while stacking faults are known to be formed by cold working metal crystals with this lattice, no-one so far has demonstrated unambiguously that mechanical twins can also be formed in them (Barrett 1950).

§5. DISCUSSION OF THE PROPOSED TWINNING MECHANISM.

The question of the energy involved in the dissociation of the unit dislocation at the node deserves attention. In both of the dissociations proposed in §3 and §4, the Burgers vectors of the resultant dislocations are perpendicular to each other, which means that these dislocations exert no forces on each other from their stress fields and that the elastic energy of the field of the dislocations is unchanged by the dissociation. However, as the sweeping dislocation moves away from the other one, it trails in its path a layer of stacking fault, and the extra energy of this fault must cause a force on the sweeping dislocation. When the distance between the dislocations exceeds a few atomic spacings the energy of the stacking fault is directly proportional to its area. Thus if the energy per unit area of the fault is ϵ then the force per unit length on the dislocation is also ϵ . This force is equivalent to a shear stress $\sigma_s = \epsilon/b$, where b is the strength of the sweeping dislocation, acting on the sweeping plane against the direction of the shear displacement caused by the dislocation. Little is known of the magnitude of ϵ , except that it is much smaller than typical grain boundary energies; the energy of {111} boundaries of annealing twins in copper has recently been determined by Fullman (1950), who obtains the value 17 erg. cm.^{-2} . Taking $\epsilon \approx 10 \text{ erg. cm.}^{-2}$ and $b \approx 10^{-8} \text{ cm.}$, then $\sigma_s \approx 10^9 \text{ dyne. cm.}^{-2}$. This value, which is much smaller than the theoretical shear strength, is not unreasonable.

The formation of the first layer of a twin will be more difficult than the subsequent growth of successive layers, because the addition of more twinned layers to an existing twin crystal does not increase appreciably the area of misfit between the twin and matrix. It follows that, if the stress needed to drive a twinning dislocation through the fields of various obstacles (other dislocations, faults, precipitates, etc.) in the crystal is σ_i , then the applied stress needed to start twinning is $\sigma_i + \sigma_s$, while that needed to continue the growth of a twin is only σ_i . Twinning resembles the yield phenomenon in this respect and it may be useful to define upper and lower twinning stresses for the start and propagation of the process. The characteristically rapid formation of twinned crystals, accompanied by discontinuities in the stress-strain relation, is almost certainly due to this effect.

It is well-known that twins can form extremely quickly and the work of Mason, McSkimin and Shockley (1948) on tin, and Millard (private communication 1950) on zinc, shows that they can form in times of the order of a few microseconds. It is important to consider how quickly a twin could form by the pole mechanism. Here we may take advantage of the analogy between the pole mechanism and the theory of crystal growth proposed by Frank (1949). When a steady spiral has built up the process of growth continues by a rotation of this spiral. The spiral makes $v/\pi l$ turns per second, where, in the present case, v refers to the velocity of the dislocation normal to itself and l is twice the limiting radius of curvature about which a section of the line can be bent by the applied stress. One layer is added to the twinned crystal for each rotation of the spiral. Following Mott and Nabarro (1948) we take $l=2(\mu/\sigma)b$, where μ is the shear modulus and σ is the applied stress; a reasonable value is $l=10^{-5}$ cm. The velocity v cannot exceed that of sound and we shall assume a limiting value $v=10^4$ cm. sec.⁻¹. Then the time needed for the twin to grow by one atom layer is of the order 3×10^{-3} microseconds. The time required to build up the steady spiral is determined by the size of the crystal and the applied stress. In the case of a 1 mm. crystal, and using the above value for l , about 1000 turns would be required. Thus the twinned crystal can be formed by the pole mechanism in a time of the order of a few microseconds.

ACKNOWLEDGMENTS.

We wish to thank Professor D. Hanson, Director of the Department of Metallurgy, for his interest and support.

REFERENCES.

- BARRETT, C. S., 1950, *Trans. Amer. Inst. Min. Met. Eng.*, **188**, 123.
FRANK, F. C., 1949, *Report of Conference on Crystal Growth* (London : The Faraday Society), p. 48.
FRANK, F. C., and READ, W. T., 1950, *Phys. Rev.*, **79**, 722.
FRANK, F. C., and VAN DER MERWE, J. H., 1949, *Proc. Roy. Soc. A*, **198**, 205.
FRENKEL, J., and KONTOROVA, T., 1939, *Journal Phys. U.S.S.R.*, **1**, (2), 137.
FULLMAN, R. L., 1950, *U.S. Atomic Energy Commission, Unclassified Report*, RL-351.
MASON, W. P., MCSKIMIN, H. J., and SHOCKLEY, W., 1948, *Phys. Rev.*, **73**, 1213.
MOTT, N. F., and NABARRO, F. R. N., 1948, *1947 Bristol Conference Report* (London : The Physical Society), p. 1.
SEITZ, F., and READ, T. A., 1941, *J. App. Phys.*, **12**, 470.
SMITH, S. W. J., DEE, A. A., and YOUNG, J., 1928, *Proc. Roy. Soc. A*, **121**, 477.

LXI. *On Virial Coefficients and the Born-Green Theory of Fluids.*

By G. S. RUSHBROOKE and H. I. SCOINS,
Clarendon Laboratory, Oxford *.

[Received January 31, 1951.]

SUMMARY.

The validity of the superposition approximation used in the Born-Green theory of classical fluids is examined by obtaining a virial expansion of the pressure in powers of the density. It is found that the second and third virial coefficients are given correctly, but that the fourth is not. The discrepancy is illustrated numerically by considering explicitly the case of a gas of rigid spheres.

The corresponding equations for a two-component mixture are also considered and it is shown that the equations are mutually consistent only when linearized.

§ 1. INTRODUCTION.

As is well known, the Born-Green theory of classical fluids embodies a so-called "superposition approximation", first introduced by Kirkwood and Boggs (1942, 1949). In the notation of Born and Green, this is expressed by the equation

$$n_3^{(123)} = n_2^{(12)} n_2^{(23)} n_2^{(31)} / n_1^3, \quad \dots \quad (1)$$

where the n 's denote appropriately normalized configurational distribution functions. And it has been asserted (see, for instance, Rodriguez 1949) that this approximation is valid at sufficiently low and sufficiently high temperatures : *i.e.* for almost perfect crystals and near-perfect gases. It is our present purpose to examine in some detail the validity of equation (1) at high temperatures or, more precisely, at low values of the density of the assembly. We shall, in fact, examine how far the Born-Green theory predicts expressions for the successive virial coefficients of an imperfect gas in agreement with the exact expressions for these coefficients that have been given by Mayer (1937-8).

We shall find that, if the pressure is written in the form

$$p = \rho kT(1 + B\rho + C\rho^2 + D\rho^3 + \dots), \quad \dots \quad (2)$$

where ρ denotes the number of systems (atoms) per unit volume in the assembly, then B and C are given correctly by the Born-Green theory

* Communicated by the Authors.

but D is not. The discrepancy will be illustrated numerically by considering explicitly the case of a gas of rigid spheres, for which the calculations can be performed very simply.

Finally, we shall consider the corresponding equations for a two-component mixture, and shall see that in this case a consistent formalism can be obtained only by subsequently linearizing the equations.

§ 2. BORN-GREEN EQUATIONS AND VIRIAL COEFFICIENTS.

Using a slightly different notation from that of (1), we denote $n_2(r)/n_1^2$ by $g(r)$ or, more precisely, $g(r, \rho, T)$. The radial distribution function, $g(r)$, is then so normalized that $g(r) \rightarrow 1$ as $r \rightarrow \infty$. Also, of course, $n_1 = \rho$.

Then the equation for the pressure, p , is

$$p = \rho kT - \frac{\rho^2}{6} \int_0^\infty g(r, \rho, T) \phi'(r) 4\pi r^3 dr, \quad \dots \quad (3)$$

where $\phi(r)$ is the interaction energy between two systems distance r apart. This equation is exact, and does not depend on any of the subsequent approximations of the Born-Green theory. This theory, which makes use of equation (1), is essentially epitomized in a non-linear integral equation for $g(r)$, namely

$$\log g(r) + \frac{\phi(r)}{kT} = \pi \rho \int_0^\infty \int_{-s}^s (s^2 - t^2) \frac{t+r}{r} [g(t+r) - 1] dt g(s) \frac{\phi'(s)}{kT} ds. \quad \dots \quad (4)$$

In order to obtain from (3) and (4) a virial expansion of the form (2), we must expand $g(r, \rho, T)$ as a power series in ρ . Following de Boer (1949), we write

$$g(r, \rho, T) = \left[\exp [-\phi(r)/kT] \right] \left[1 + a_1 \rho + a_2 \frac{\rho^2}{2} + \dots + a_n \frac{\rho^n}{n!} + \dots \right] \quad \dots \quad (5)$$

and then (4) gives a set of equations for the $a_n(r, T)$. Substitution in (3) then yields the requisite virial expansion.

Writing $\exp [-\phi(r)/kT] - 1 = \alpha(r)$, it is easily verified that the equations for a_1 and a_2 are

$$a_1(r) = -\pi \int_0^\infty \int_{-s}^s (s^2 - t^2) \frac{t+r}{r} \alpha(t+r) dt \alpha'(s) ds \quad \dots \quad (6)$$

and

$$a_2(r) - a_1^2(r) = -2\pi \int_0^\infty \int_{-s}^s (s^2 - t^2) \frac{t+r}{r} \alpha(t+r) dt a_1(s) \alpha'(s) ds \\ - 2\pi \int_0^\infty \int_{-s}^s (s^2 - t^2) \frac{t+r}{r} a_1(t+r) [\alpha(t+r) + 1] dt \alpha'(s) ds. \quad \dots \quad (7)$$

Consequently, if we denote the result of substituting these expressions in (3) by

$$p = \rho kT(1 + B_1\rho + C_1\rho^2 + D_1\rho^3 + \dots),$$

then

$$B_1 = \frac{1}{6} \int_0^\infty 4\pi r^3 \alpha'(r) dr, \quad \dots \dots \dots \quad (8)$$

$$C_1 = \frac{1}{6} \int_0^\infty 4\pi r^3 \alpha'(r) a_1(r) dr, \quad \dots \dots \dots \quad (9)$$

$$D_1 = \frac{1}{12} \int_0^\infty 4\pi r^3 \alpha'(r) a_2(r) dr. \quad \dots \dots \dots \quad (10)$$

These formulæ, which give the successive virial coefficients on the basis of the Born-Green theory, embodying the Kirkwood-Boggs superposition approximation, have now to be compared with the exact formulæ for these virial coefficients which we know from Mayer's work are

$$B = -2\pi \int_0^\infty r^2 \alpha(r) dr, \quad \dots \dots \dots \dots \dots \quad (11)$$

$$C = -\frac{1}{3} \int \int \alpha_{12} \alpha_{23} \alpha_{31} d\tau_2 d\tau_3 \quad \dots \dots \dots \dots \quad (12)$$

and

$$\begin{aligned} D = & -\frac{1}{8} \int \int \int [\alpha_{12} \alpha_{23} \alpha_{31} \alpha_{41} \alpha_{42} \alpha_{43} + 6\alpha_{12} \alpha_{23} \alpha_{31} \alpha_{41} \alpha_{42} \\ & + 3\alpha_{12} \alpha_{23} \alpha_{34} \alpha_{41}] d\tau_2 d\tau_3 d\tau_4, \quad \dots \quad (13) \end{aligned}$$

where $\alpha_{ij} = \alpha(|\mathbf{r}_j - \mathbf{r}_i|)$, and $d\tau_i$ denotes a volume element at the point \mathbf{r}_i .

It is obvious at once, by partial integration, that $B_1 = B$. Before proceeding further with the comparison, however, it is convenient to derive some useful mathematical formulæ involving Fourier transforms.

§ 3. SOME MATHEMATICAL LEMMAS.

I. With the notation illustrated by fig. 1

$$\begin{aligned} & \int \dots \int_{(n)} f_1(r_1) f_2(r_2) \dots f_n(r_n) f_{n+1}(r_{n+1}) d\tau_1 d\tau_2 \dots d\tau_n \\ & = (2\pi)^{\frac{3n-1}{2}} \int_{-\infty}^{\infty} u \mathcal{F}_1(u) \mathcal{F}_2(u) \dots \mathcal{F}_{n+1}(u) \frac{\sin ux}{x} du \end{aligned}$$

where

$$u \mathcal{F}_i(u) = \frac{1}{\sqrt{(2\pi)}} \int_{-\infty}^{\infty} r f_i(r) \sin ur dr$$

and the f_i are even functions of r .

This result is easily obtained by induction. We start by considering the case illustrated in fig. 2. Since

$$d\tau = r_1 r_2 dr_1 dr_2 d\chi/s,$$

where χ denotes an angle of rotation about AB, we have

$$\int f_1(r_1) f_2(r_2) d\tau = 2\pi \int_0^\infty \int_{s-r_1}^{s+r_2} \frac{r_1 f_1(r_1) r_2 f_2(r_2)}{s} dr_1 dr_2.$$

Writing $r_1 f_1(r_1) = \frac{1}{\sqrt{(2\pi)}} \int_{-\infty}^{\infty} u \mathcal{F}_1(u) \sin r_1 u du$, and interchanging the

Fig. 1.

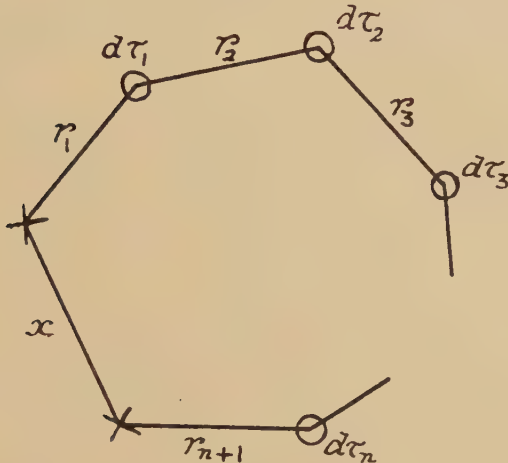
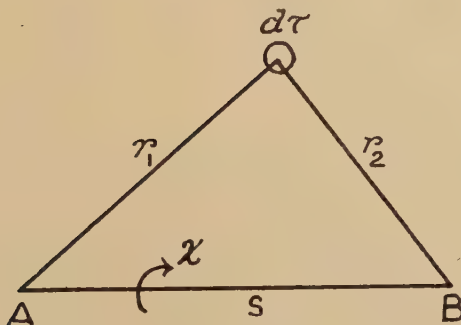


Fig. 2.



order of integration, we find

$$\begin{aligned} \int f_1(r_1) f_2(r_2) d\tau &= 2\pi \frac{2}{\sqrt{(2\pi)}} \int_0^\infty dr_2 \int_{-\infty}^{\infty} \frac{\sin su}{su} u \mathcal{F}_1(u) r_2 f_2(r_2) \sin r_2 u du \\ &= 2\pi \int_{-\infty}^{\infty} u \mathcal{F}_1(u) \mathcal{F}_2(u) \frac{\sin su}{s} du. \end{aligned}$$

Considering next the integral (see fig. 3)

$$I \equiv \iint f_1(r_1) f_2(r_2) f_3(r_3) d\tau d\tau'.$$

we have

$$\begin{aligned} I &= (2\pi)^2 \int \dots \int dr_1 dr_2 \frac{r_1 f_1(r_1) r_2 f_2(r_2)}{s} \frac{s r_3 f_3(r_3)}{t} ds dr_3 \\ &= (2\pi)^2 \int_{-\infty}^{\infty} \int_0^{\infty} \int_{t-r_3}^{t+r_3} u \mathcal{F}_1(u) \mathcal{F}_2(u) \frac{\sin su}{t} r_3 f_3(r_3) ds dr_3 du \\ &= (2\pi)^{5/2} \int_{-\infty}^{\infty} u \mathcal{F}_1(u) \mathcal{F}_2(u) \mathcal{F}_3(u) \frac{\sin tu}{t} du. \end{aligned}$$

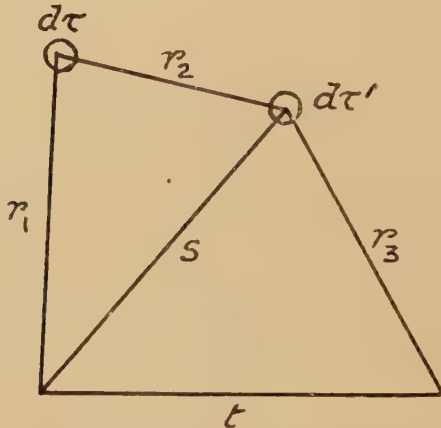
The general result stated in I. follows by simply repeating the argument.

Letting $x \rightarrow 0$, we have

II. With the notation illustrated by fig. 4

$$\begin{aligned} \int \dots \int_{(n)} f_1(r_1) f_2(r_2) \dots f_{n+1}(r_{n+1}) d\tau_1 d\tau_2 \dots d\tau_n \\ = (2\pi)^{\frac{3n-1}{2}} \int_{-\infty}^{\infty} u^2 \mathcal{F}_1(u) \mathcal{F}_2(u) \dots \mathcal{F}_{n+1}(u) du. \end{aligned}$$

Fig. 3.



These results are also proved in a paper by Montroll and Mayer (1941), but their method of derivation is considerably longer than ours. For the formulæ to be valid the interatomic potential must decrease more rapidly than for purely ionic interactions, which is certainly so for the van der Waal's forces normally responsible for gaseous imperfections.

§ 4. DISCUSSION OF C AND C₁.

On account of II. above, equation (12) gives at once

$$C = -\frac{1}{3}(2\pi)^{5/2} \int_{-\infty}^{\infty} u^2 [\beta(u)]^3 du, \quad \dots \quad (14)$$

where

$$u\beta(u) = \frac{1}{\sqrt{(2\pi)}} \int_{-\infty}^{\infty} r\alpha(r) \sin ur dr, \quad \dots \quad (15)$$

$\alpha(r)$ being regarded as an even function of r .

To obtain from (9) an analogous equation for C_1 we must first consider $a_1(r)$. On replacing $(t+r)\alpha(t+r)$ in (6) by its Fourier transform according to (15), namely

$$\frac{1}{\sqrt{(2\pi)}} \int_{-\infty}^{\infty} u\beta(u) \sin u(t+r) du$$

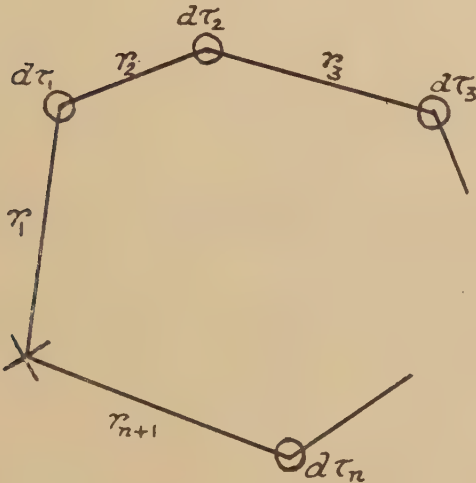
and integrating first with respect to t and then with respect to s , we find that

$$ra_1(r) = 2\pi \int_{-\infty}^{\infty} u[\beta(u)]^2 \sin ur du. \quad \quad (16)$$

Consequently, by (9),

$$C_1 = \frac{4\pi^2}{3} \int_0^{\infty} r^2 \alpha'(r) \int_{-\infty}^{\infty} u[\beta(u)]^2 \sin ur du dr.$$

Fig. 4.



Integrating partially with respect to r we have, since $\alpha(r)$ vanishes at infinity,

$$C_1 = -\frac{4\pi^2}{3} \int_{-\infty}^{\infty} \left\{ \sqrt{(2\pi)} u^2 [\beta(u)]^3 + \frac{\sqrt{(2\pi)}}{2} u^2 [\beta(u)]^2 \frac{d}{du} (u\beta(u)) \right\} du$$

and the second term on the right vanishes since for interaction potentials of the type under consideration $u\beta(u)$ vanishes at infinity. Thus

$$C_1 = -\frac{1}{3}(2\pi)^{5/2} \int_{-\infty}^{\infty} u^2 [\beta(u)]^3 du = C$$

and the third virial coefficient is given correctly by the non-linear integral equation of the Born-Green theory.

§ 5. DISCUSSION OF D AND D₁.

On account of II., and by applying Parseval's theorem to equation (16), we have for the last term on the right hand side of (13),

$$\begin{aligned} -\frac{3}{8} \iiint \alpha_{12}\alpha_{23}\alpha_{34}\alpha_{41} d\tau_2 d\tau_3 d\tau_4 &= -\frac{3}{8}(2\pi)^4 \int_{-\infty}^{\infty} u^2 [\beta(u)]^4 du \\ &= -\frac{3\pi}{2} \int_0^{\infty} r^2 a_1^2(r) dr. \quad . . . \quad (17) \end{aligned}$$

For the second term on the right hand side of (13), application of I. and II. leads to

$$-\frac{3}{4} \iiint \alpha_{12}\alpha_{23}\alpha_{34}\alpha_{41}\alpha_{42} d\tau_1 d\tau_2 d\tau_3 = -\frac{3}{4}(2\pi)^{2/5} \int_{-\infty}^{\infty} u^2 \mathcal{F}(u) [\beta(u)]^2 du,$$

where

$$u\mathcal{F}(u) = \frac{1}{\sqrt{(2\pi)}} \int_{-\infty}^{\infty} tf(t) \sin ut dt \text{ and } tf(t) = 2\pi\alpha(t) \int_{-\infty}^{\infty} u[\beta(u)]^2 \sin ut du.$$

Using Parseval's theorem, and (16), we thus obtain

$$-\frac{3}{4} \iiint \alpha_{12}\alpha_{23}\alpha_{31}\alpha_{41}\alpha_{42} d\tau_2 d\tau_3 d\tau_4 = -3\pi \int_0^{\infty} r^2 \alpha(r) a_1^2(r) dr. \quad . . . \quad (18)$$

We have not been able to obtain any such simple formula for the first term on the right hand side of (13), but we shall find that the expressions involving $a_1(r)$ in (17) and (18) arise naturally in the evaluation of D_1 , to which we now turn.

From equations (7) and (10) we obtain, after partial integrations of (7),

$$\left. \begin{aligned} D_1 &= \frac{\pi}{3} \int_0^{\infty} r^3 \alpha'(r) a_1^2(r) dr && \text{(i.)} \\ &+ \frac{2\pi^2}{3} \int_0^{\infty} r^2 \alpha'(r) \int_0^{\infty} \int_{-s}^s (s^2 - t^2)(t+r)\alpha(t+r) dt \cdot a_1(s)\alpha(s) ds dr && \text{(ii.)} \\ &+ \frac{4\pi^2}{3} \int_0^{\infty} r^2 \alpha'(r) \int_0^{\infty} \int_{-s}^s (t+r)\alpha(t+r) dt \cdot s a_1(s)\alpha(s) ds dr && \text{(iii.)} \\ &+ \frac{4\pi^2}{3} \int_0^{\infty} r^2 \alpha'(r) \int_0^{\infty} \int_{-s}^s (t+r)\alpha(t+r)a_1(t+r) dt \cdot s\alpha(s) ds dr && \text{(iv.)} \\ &+ \frac{4\pi^2}{3} \int_0^{\infty} r^2 \alpha'(r) \int_0^{\infty} \int_{-s}^s (t+r)a_1(t+r) dt \cdot s\alpha(s) ds dr. && \text{(v.)} \end{aligned} \right\} \quad (19)$$

It is convenient to number the successive terms on the right hand side of (19), (i.), (ii.), . . . (v.).

Then using the techniques already illustrated above, we can show without difficulty that

$$(v.) = -\frac{3\pi}{2} \int_0^{\infty} r^2 a_1^2(r) dr = (17)$$

and

$$(iii.) = (iv.) = -\pi \int_0^\infty r^2 \alpha(r) a_1^2(r) dr + \frac{\pi}{3} \int_0^\infty r^3 \alpha(r) a_1(r) a_1(r) dr$$

so that

$$(i.) + (iii.) + (iv.) = -3\pi \int_0^\infty r^2 \alpha(r) a_1^2(r) dr = (18).$$

Thus the second and third terms on the right hand side of (13) are accounted for by the terms (i.), (iii.), (iv.) and (v.) of (19). But the remaining part of D_1 , namely term (ii.) in (19), is *not* equal to the remaining part of D , *i.e.* to the first term on the right hand side of (13). This is clear from dimensional arguments and, as we shall see, is confirmed when we make explicit calculations for the case of hard spheres in §7 below. For the purposes of calculation it is convenient to write (ii.) in the form

$$(ii.) = -\frac{2\pi^2}{3} \int_0^\infty r^2 a_1'(r) \alpha(r) \frac{d}{dr} \left[r^6 \frac{d}{dr} \left\{ \frac{1}{r^6} \int_{-\infty}^\infty \frac{[\beta(u)]^2}{u} \sin ur du \right\} \right] dr. \quad (20)$$

We thus see that the Born-Green non-linear integral equation, (4), for $g(r)$, deriving from the superposition approximation, fails to give correctly the fourth virial coefficient, D , of an imperfect gas; and that the reason for this failure is that it does not do justice to the term involving $\iiint \alpha_{12}\alpha_{23}\alpha_{34}\alpha_{41}\alpha_{42}\alpha_{43} d\tau_2 d\tau_3 d\tau_4$ in the correct expression for this virial coefficient.

Before giving the results of explicit calculations for the simple case of a gas of hard spheres it will be well to consider how these results are affected, if at all, if we base discussion not on (4) but on a linear approximation to this non-linear equation. Most of the attempts made so far to determine explicit distribution functions for a given intermolecular potential have been based on such a linearization technique. We confine our discussion to the particular method of linearization used by Rodriguez (1949).

§ 6. EFFECT OF LINEARIZING THE EQUATION FOR $g(r)$.

Rodriguez has shown that if, in (4), we write

$$g(r) = \exp [f(r) - \phi(r)/kT], \quad \dots \dots \dots \quad (21)$$

keep only terms linear in $f(r)$ and replace certain products $f(r)\alpha(r)$ and $f(r)\alpha'(r)$ by $(\epsilon-1)\alpha(r)$ and $(\epsilon-1)\alpha'(r)$, respectively, where

$$\epsilon - 1 = \frac{\int_0^\infty r^2 f(r) \alpha(r) dr}{\int_0^\infty r^2 \alpha(r) dr}, \quad \dots \dots \dots \quad (22)$$

then the resulting linear equation can be solved, the solution being given by

$$rf(r) = \frac{1}{\sqrt{(2\pi)}} \int_{-\infty}^\infty \frac{\epsilon^2 s [\beta(s)]^2 \sin rs}{\lambda - \epsilon \beta(s)} ds, \quad \dots \dots \dots \quad (23)$$

where $\lambda^{-1} = (2\pi)^{3/2}\rho$. The precise nature of these approximations is not at all clear, but our final paragraph will suggest that when dealing with binary mixtures some such technique is not only convenient but necessary, and it will be well therefore to discuss briefly the virial coefficient problem on the basis of equations (23), (22), (21) and (3).

The procedure is exactly as before, except that now we must also expand ϵ as

$$\epsilon = 1 + c_1\rho + c_2\rho^2 + \dots \quad \dots \quad \dots \quad \dots \quad \dots \quad (24)$$

There is no need to enter into the details of the calculation. It is sufficient to state that if we express the pressure p as

$$p = \rho kT[1 + B_2\rho + C_2\rho^2 + D_2\rho^3 + \dots].$$

Then we find

$$B_2 = B_1 = B,$$

$$C_2 = C_1 = C,$$

but

$$\left. \begin{aligned} D_2 &= \frac{8\pi^2}{3} c_1 \int_0^\infty r^2 \alpha'(r) \int_{-\infty}^\infty s [\beta(s)]^2 \sin rs \, ds \, dr \\ &\quad + \frac{2\pi}{3} (2\pi)^{5/2} \int_0^\infty r^2 \alpha'(r) \int_{-\infty}^\infty s [\beta(s)]^3 \sin rs \, ds \, dr \\ &\quad + \frac{4\pi^3}{3} \int_0^\infty r \alpha'(r) \left[\int_{-\infty}^\infty s [\beta(s)]^2 \sin rs \, ds \right]^2 \, dr, \end{aligned} \right\} \begin{matrix} (a) \\ (b) \\ (c) \end{matrix} \quad (25)$$

where

$$c_1 = (2\pi)^{3/2} \int_0^\infty u^2 [\beta(u)]^3 \, du / \int_0^\infty r^2 \alpha(r) \, dr = 3C/2B. \quad \dots \quad (26)$$

It is then not difficult to show that, comparing the terms of (25) and (19),

$$(b) = (v.),$$

$$(c) = (i.)$$

but

$$(a) \neq (ii.) + (iii.) + (iv.).$$

In fact

$$(a) = 3C^2/B. \quad \dots \quad \dots \quad \dots \quad \dots \quad \dots \quad (27)$$

Thus linearization does not affect the second and third virial coefficients B and C , but does affect the fourth virial coefficient.

We shall now illustrate these results by using the above formulæ to calculate B , C , D_1 and D_2 for a gas of hard spheres. The value of D (as also B and C) for such a hypothetical gas has already been calculated by Happel and by Majumdar : see Fowler and Guggenheim (1939).

§ 7. CALCULATIONS FOR A GAS OF HARD SPHERES.

We consider hard spheres of diameter a . Then $\phi(r) = \infty$, $r < a$ and $\phi(r) = 0$, $r > a$. Whence

$$\alpha(r) = -1, \quad 0 < r < a; \quad \alpha(r) = 0, \quad a < r.$$

Then

$$u\beta(u) = \sqrt{\left(\frac{2}{\pi}\right) \frac{d}{du} \left(\frac{\sin ua}{u}\right)}$$

and, by (16),

$$\begin{aligned}ra_1(r) &= 0, \quad |r| > 2a \\&= \frac{\pi}{12} r(r-2a)^2(r+4a), \quad |r| < 2a.\end{aligned}$$

From (11),

$$B = \frac{2\pi a^3}{3} = 4v = b \text{ say,}$$

where v is the volume of one of the spheres.

From (14),

$$C = \frac{5\pi^2 a^6}{18} = \frac{5}{8} b^2.$$

We now consider the various contributions to D_1 and D_2 . They are given in Table I. below :

TABLE I.

D_1	Value	D_2	Value
(i.) + (iii.) + (iv.) from (18)	$\frac{6347}{4480} b^3$	(a) from (27)	$\frac{75}{64} b^3$
(v.) from (17)	$-\frac{34}{35} b^3$	(b) from (17)	$-\frac{34}{35} b^3$
(ii.) from (20)	$-\frac{493}{2240} b^3$	(c) from (i.)	$\frac{25}{128} b^3$
Total D_1 =	$\frac{1009}{4480} b^3$ $0.2252 b^3$	Total D_2 =	$\frac{1773}{4480} b^3$ $0.3958 b^3$

These values have to be compared with the value $D=0.2869b^3$ calculated by Happel and by Majumdar. We see that the non-linear integral equation leads to rather too small a value for D , while Rodriguez's method of linearization yields too large a value.

Finally we would observe that (26) shows that for hard spheres ϵ should increase with the density ρ . If, however, we adopt the crudest form of linearization and take $\epsilon=1$ throughout, then B_2 and C_2 are unchanged, but D_2 loses the contribution (a) and becomes $D'_2=-\frac{3477}{4480} b^3$, which has the wrong sign. Here we have not ignored f^2 in finding p ; if we do so we get $D'_2=-\frac{34}{35} b^3$, which is also negative.

§ 8. BINARY MIXTURES.

In this discussion we shall try to keep the mathematical exposition as short as possible since the calculations though essentially straightforward are necessarily cumbersome if presented at all fully. To obtain the

equations we have simply to follow Born and Green's procedure. We derive first an infinite set of equations for the equilibrium distribution functions, and then cut these off by means of the superposition approximation. We now need, however, four equations of type (1), namely (with a self-explanatory notation)

$$\left. \begin{aligned} n_{\text{AAA}}(123) &= n_{\text{AA}}(12)n_{\text{AA}}(23)n_{\text{AA}}(31)/n_A^3, \\ n_{\text{AAB}}(123) &= n_{\text{AA}}(12)n_{\text{AB}}(23)n_{\text{AB}}(13)/n_A^2 n_B, \end{aligned} \right\} \quad . . . \quad (28)$$

and the two equations which result from interchanging A and B.

We then obtain, in place of (4), four non-linear integral equations which may be written

$$\begin{aligned} \log g_{ij}(r) + \frac{\phi_{ij}(r)}{kT} = & \pi \rho_A \int_0^\infty \int_{-s}^s (s^2 - t^2) \frac{t+r}{r} [g_{iA}(t+r) - 1] dt g_{jA}(s) \frac{\phi'_{jA}(s)}{kT} ds \\ & + \pi \rho_B \int_0^\infty \int_{-s}^s (s^2 - t^2) \frac{t+r}{r} [g_{iB}(t+r) - 1] dt g_{jB}(s) \\ & \times \frac{\phi'_{jB}(s)}{kT} ds, \quad . . . \end{aligned} \quad (29)$$

where $i=A$ or B , $j=A$ or B , and the order of the suffices is immaterial. In terms of the n 's, $g_{ij}(r) = n_{ij}(r)/n_i n_j$ and $\rightarrow 1$ as $r \rightarrow \infty$. Moreover

$$n_A = N_A/V = \rho_A \quad \text{and} \quad n_B = N_B/V = \rho_B.$$

The equation for the pressure is

$$\begin{aligned} \frac{p}{kT} = & \rho - \frac{\rho^2}{6kT} \int_0^\infty [x_A^2 g_A(r) \phi'_{AA}(r) + 2x_A x_B g_{AB}(r) \phi'_{AB}(r) \\ & + x_B^2 g_{BB}(r) \phi'_{BB}(r)] 4\pi r^3 dr, \quad . . . \end{aligned} \quad (30)$$

where $\rho = (N_A + N_B)/V$, $x_A = N_A/(N_A + N_B)$ and $x_B = N_B/(N_A + N_B)$.

To obtain a virial expansion we proceed exactly as before except that now we have to use double power series in the two variables ρ_A and ρ_B instead of simply power series in ρ . If we write

$$p = \rho kT [1 + B\rho + C\rho^2 + D\rho^3 + \dots]$$

then we find

$$B = -2\pi \left[x_A^2 \int_0^\infty \alpha_{AA}(r) r^2 dr + 2x_A x_B \int_0^\infty \alpha_{AB}(r) r^2 dr + x_B^2 \int_0^\infty \alpha_{BB}(r) r^2 dr \right] \quad . . . \quad (31)$$

and

$$\begin{aligned} C = & -\frac{1}{3} \left[x_A^3 \iint \alpha_{AA}(r_{12}) \alpha_{AA}(r_{23}) \alpha_{AA}(r_{13}) d\tau_2 d\tau_3 \right. \\ & + 3x_A^2 x_B \iint \alpha_{AA}(r_{12}) \alpha_{AB}(r_{23}) \alpha_{AB}(r_{13}) d\tau_2 d\tau_3 \\ & + 3x_A x_B^2 \iint \alpha_{BB}(r_{12}) \alpha_{AB}(r_{23}) \alpha_{AB}(r_{13}) d\tau_2 d\tau_3 \\ & \left. + x_B^3 \iint \alpha_{BB}(r_{12}) \alpha_{BB}(r_{23}) \alpha_{BB}(r_{13}) d\tau_2 d\tau_3 \right]. \quad . . . \quad (32) \end{aligned}$$

And these are the correct expressions for the second and third virial coefficients of a binary mixture (Mayer 1939).

To this stage the calculations, though laborious, are essentially straightforward. The only mathematical tool required, apart from algebraic manipulation, is the result

$$\int_0^\infty \int_{-s}^s (s^2 - t^2)(t+r)f(t+r)g'(s) dt ds \\ = \int_0^\infty \int_{-s}^s (s^2 - t^2)(t+r)g(t+r)f'(s) dt ds, \dots \quad (33)$$

which is easily proved by introducing the Fourier transforms of $rf(r)$ and $rg(r)$. We need (33) in order to show that the two equations of type (29) for $g_{AB}(r)$, obtained by taking $i=A$, $j=B$ and $i=B$, $j=A$ respectively, are mutually consistent as far as terms linear in ρ are concerned.

When however, we proceed to calculate D we meet an entirely new difficulty. For we now find that these two equations for $g_{AB}(r)$ are not mutually consistent when we include terms quadratic in ρ . Indeed, it can be shown that the reason for the inconsistency can be traced to precisely the same defect in the superposition principle that led to $D_1 \neq D$ for a one-component assembly.

We thus find that when the Born-Green formalism is extended to binary mixtures the superposition approximation leads to four non-linear equations for the three equilibrium radial distribution functions, and that these four equations are not mutually consistent. If, however, we linearize the equations in the manner due to Rodriguez, then in place of (29) we have the four equations

$$rf_{ij}(r) = 2\pi\rho_A \int_0^\infty \int_{-s}^s (t+r)[f_{iA}(t+r) + \epsilon_{iA}\alpha_{iA}(t+r)] dt \epsilon_{jA}s\alpha_{jA}(s) ds \\ + 2\pi\rho_B \int_0^\infty \int_{-s}^s (t+r)[f_{iB}(t+r) + \epsilon_{iB}\alpha_{iB}(t+r)] dt \epsilon_{jB}s\alpha_{jB}(s) ds, \quad (34)$$

$i=A, B$ and $j=A, B$; and it is easy to show that these equations are entirely mutually consistent. Their solution, by the method of Fourier transforms, can be found without difficulty: we shall not, however, give it here as the expressions are rather unwieldy and we do not wish to discuss them further at present.

REFERENCES.

- DE BOER, J., 1949, *Reports on Progress in Physics*, **12**, (London : The Physical Society), p. 305.
 BORN, M., and GREEN, H. S., 1949, *A General Kinetic Theory of Liquids*, (Cambridge : University Press), Ch. I. and II.
 FOWLER, R. H., and GUGGENHEIM, E. A., 1939, *Statistical Thermodynamics*, (Cambridge : University Press), § 717.
 KIRKWOOD, J. G., and BOGGS, E. M., 1942, *J. Chem. Phys.*, **10**, 394.
 MAYER, J. E. et al., 1937-8, *J. Chem. Phys.*, **5**, 67, 74 ; **6**, 87 ; 1939, *Ibid.*, **43**, 71.
 MONTROLL, E. W., and MAYER, J. E., 1941, *J. Chem. Phys.*, **9**, 626.
 RODRIGUEZ, A. E., 1949, *Proc. Roy. Soc. A*, **196**, 73.

LXII. *The Critical Magnetic Fields of Aluminium, Cadmium, Gallium and Zinc.*

By B. B. GOODMAN and E. MENDOZA *,
Royal Society Mond Laboratory, Cambridge †.

[Received March 7, 1951.]

ABSTRACT.

The low temperatures produced by the adiabatic demagnetization of a paramagnetic salt have been used to cool specimens of aluminium, cadmium, gallium and zinc, and their critical fields have been measured down to 0.1°K . The magnetic measurements on the metal and the salt were made independently and the experimental arrangement had the further advantage that the quality of the thermal contact between the metal and the salt could be studied. The results could be accurately expressed by relations of the form $H_c = H_0(1 - (T/T_c)^2)$; values of H_0 and T_c for each metal are tabulated.

§ 1. INTRODUCTION.

COMPARATIVELY little information is at present available on the critical fields of superconductors with low transition temperatures. In this paper measurements of the critical fields of aluminium, cadmium, gallium and zinc are described. The low temperatures were produced by the adiabatic demagnetization of a paramagnetic salt, using a technique already described briefly by one of us (Mendoza 1948), in which the metal specimen and the salt were separated but were in thermal contact through a long copper rod. This arrangement has the advantage that it is possible to make magnetic observations on the metal specimen and the salt independently. Moreover the condition of the specimen can be more easily controlled than in the method used by Kurti and Simon (1935 b) and more recently by Daunt and Heer (1949 a, b), where the salt and chips of the metal were pressed together into a pill. The superconducting transitions in various steady magnetic fields were studied by measuring the effective susceptibility of the metal in a low-frequency alternating field; the specific resistance of the normal metal could also be deduced from these measurements.

§ 2. THE EXPERIMENTAL ARRANGEMENT.

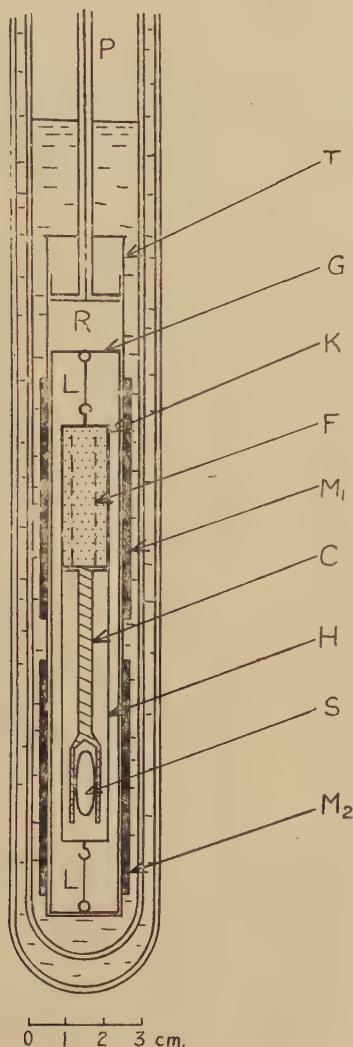
A diagram of the low temperature part of the apparatus is shown in fig. 1. The salt-tube T stood in a Dewar flask of liquid helium, itself surrounded by a Dewar of liquid air. The metal specimen S was gripped in the cup at the lower end of the copper rod C. Strips of copper foil F with a total area of about 6 cm^2 were hard soldered to the top of C:

* Now at the H. H. Wills Physical Laboratory, Bristol.

† Communicated by Dr. D. Shoenberg.

there was no evidence that the magnetic observations were affected by the hard solder. A paste of powdered paramagnetic salt (either ferric ammonium alum or chromium potassium alum) mixed with a solution of a plastic cement in acetone was pressed around the foil in a cylindrical

Fig. 1.



The low temperature part of the apparatus.

die under a pressure of 2000 atm.; the resulting pill K was 1.6 cm. in diameter and about 4 cm. long. It was found that this arrangement gave adequate thermal contact between the salt and the superconductor, and that within five minutes of demagnetizing the salt to 0.1°K. good thermal equilibrium had been reached. The amount of heat reaching

S and C from stray sources was reduced by a cylindrical shield of copper foil H in good thermal contact with the salt K. Vertical slots were cut in H and in the cup holding S in order to reduce the effect of eddy currents; the slots in the cup also made it easier to grip S. The whole system was suspended by cotton threads L from the framework G which stood inside the salt-tube T. Hot gas molecules coming down the pumping tube P were prevented from impinging on the cold salt K by the radiation shutter R.

The longitudinal magnetic field needed for the critical field determinations was provided by a solenoid which could be suspended around the liquid air Dewar. This solenoid gave a field which was uniform within $\frac{1}{2}$ per cent over a length of 3·0 cm., and the effect of its field on the temperature of the salt was always negligible.

M_1 and M_2 are mutual inductances surrounding the salt and the superconductor respectively. Since the value of the empty mutual inductance was not known very accurately, only changes in susceptibility of K or S could be deduced from measurements of the mutual inductance. Owing partly to losses in the circuit and partly to losses in the specimen (particularly for the metal in the normal state) each mutual inductance can be regarded as complex and will be denoted by $M' - jM''$. Values of M' and M'' for both mutual inductances were measured by a Hartshorn A.C. bridge. The measuring current was supplied by a 40 c./s. frequency-stabilized alternator and detection was by means of an amplifier and a vibration galvanometer.

The contribution to M'_1 was of order $(400/T)\mu\text{H}$ from the salt and the change of M'_2 corresponding to the transition of the metal from the normal to the superconducting state was of order $40\mu\text{H}$. By using a measuring field of amplitude 1 gauss the bridge could be set to an accuracy of $0\cdot05\mu\text{H}$ in the absence of a steady magnetic field, but only to $0\cdot3\mu\text{H}$ in a field owing to the effect on the galvanometer of fluctuations in the field.

TABLE I.
Characteristics of the Metal Specimens.

	Source	Estimated % purity	Length (mm.)	Diam. (mm.)	n	$(\rho/\rho_{273}) \times 10^4$
Aluminium	J 1011	99.995	26·2	6·5	0·074	18
Cadmium	N	99.996	28·5	7·1	0·074	3·1
Gallium	J 3419	~99.99	26·8	3·00	0·023	1·0
Zinc	J 1790	99.999	27·5	6·8	0·074	14

J=Johnson, Matthey & Co.

N=New Jersey Zinc Co.

The quantities n and ρ/ρ_{273} are referred to later in the paper.

§ 3. THE SPECIMENS.

The characteristics of the metal specimens are given in Table I. The aluminium and zinc specimens were both turned to an accurately ellipsoidal shape. The cadmium and gallium specimens were cast in

thin-walled glass tubes which were approximately ellipsoidal in internal shape, and the glass was afterwards cracked away. Each specimen was annealed in a helium atmosphere to remove internal strains, and then lightly etched in acid to remove surface impurities.

§ 4. EXPERIMENTAL PROCEDURE.

(a) *The temperature of the specimen.*

The demagnetizations were made from magnetic fields of up to 20 kilogauss provided by a water-cooled solenoid which could be raised into position around the liquid air Dewar. It was found that unless demagnetizations were carried out from a helium bath temperature of about 1.5°K . or more the rate of warming of the cold salt was rapid above about 0.7°K . It seems probable that at lower initial temperatures the out-gassing of the salt tube was much less complete, and after demagnetization helium from the salt-tube wall condensed on the cold salt, only to evaporate and destroy the thermal vacuum when the salt warmed to about 0.7°K . Under the best conditions the natural heat input into the cold system was about 3 ergs sec. $^{-1}$.

The temperature of the salt after demagnetization was determined by standard procedure (Kurti and Simon 1935 b). The mutual inductance of M_1 was first measured at three or four temperatures in the helium range, while helium gas in the salt-tube at a pressure of about 0.1 mm. of mercury maintained the salt in thermal equilibrium with the helium bath. The helium bath temperature was deduced from the pressure in the cryostat using the 1949 scale of temperature (van Dijk and Shoenberg 1949). A graph was plotted of M'_1 against $1/(T - \Delta)$, where $\Delta = \lambda f(4\pi/3 - N)$; f is the filling factor, λ the Curie constant per c.c. and N is the demagnetizing factor of the external shape of the pill; the parameter Δ which was usually about 0.02°K . was introduced in order to allow for the non-spherical shape of the specimen. The graph was a straight line as was to be expected for a salt obeying a Curie law. After demagnetization the value of M' was again measured and a magnetic temperature T^* was deduced from the value of $1/(T - \Delta)$ given by linear extrapolation of the graph. The values of T^* obtained at low temperatures differed slightly from thermodynamic temperatures T owing to departures from Curie's law and were corrected on the basis of various published data (Casimir, de Haas and de Klerk 1939, Cooke 1949). The reliability of this procedure for deducing T is indicated by the agreement between estimates of T for a given critical field of a zinc specimen using ferric ammonium alum and chromium potassium alum respectively. At 0.2°K . the two sets of measurements were in agreement to better than 10^{-2} deg. although the values of $T^* - T$ were of order 3×10^{-2} deg.

(b) *Measurement of the critical field.*

After the demagnetization the specimen was superconducting and measurements of M'_2 and M''_2 were made as the magnetic field of the

solenoid B was steadily increased. The real part M'_2 was constant as long as the specimen was wholly superconducting, but owing to coupling with the solenoid there was a small increase in M''_2 as the resistance of the solenoid circuit was lowered. At the entry to the intermediate state a sharp rise of both M'_2 and M''_2 was observed, and the steady field corresponding to this was assumed to be $(1-n)$ times the critical field H_c of the superconductor, where $4\pi n$ was the demagnetizing coefficient of the specimen. The cadmium and gallium specimens were not accurately ellipsoidal but the resulting uncertainty in allowing for the demagnetizing effect was only of order $\frac{1}{2}$ per cent. Immediately after the sharp rise in M'_2 and M''_2 had been observed the value of M'_1 was measured, thus giving the temperature at which H_c had been measured. Owing to the gradual warming of the salt a small correction was necessary to allow for the rise in temperature between the measurement of H_c and the measurement of M'_1 . By repeating the whole procedure as the salt warmed up to bath temperature a series of values of H_c at various temperatures between 0.1°K . and the transition temperature was obtained.

The transitions in the absence of an applied magnetic field were studied by following M'_2 and M''_2 as the metal warmed through the transition temperature. Values of T_c deduced in this way agreed well with those obtained by extrapolation of the critical field curves. From the change of M'_2 and M''_2 between the superconducting and normal state the value of the specific resistance of the normal metal could be calculated using standard eddy current theory. For this purpose the specimens were treated as if they were long cylinders; the error due to this assumption is probably not more than a few per cent. Values of the ratio ρ/ρ_{273} of this resistivity to the resistivity at 273°K . which are a guide to the quality of the specimens, are given in Table I.

§ 5. CORRECTIONS AND SOURCES OF ERROR.

The measurements of the specimen temperature and the corresponding critical field were subject to a number of corrections and sources of error which need discussion.

(a) Temperature.

In preliminary measurements by one of us (Mendoza 1948) it was found that the thermal contact between the copper rod and the salt was inadequate for the amount of heat being developed in the rod by eddy currents (no heat of course was developed in the superconductor). This was revealed by the fact that the values of T recorded for a given H_c increased when a ge measuring currents were used. In the present arrangement the thermal contact between the copper rod and the salt was improved; a correction was applied for the temperature difference between the rod and the salt produced by eddy current heating but this was only of order 10^{-2} deg. for the measuring currents actually used.

There remains the possibility that the temperatures of the specimen and the salt may differ owing to a thermal gradient set up by the natural warming of the whole system. Estimates of the probable value of the temperature difference between the salt and the specimen due to this cause showed that under the actual experimental conditions and at temperatures above 0.1°K . it was unlikely to exceed 10^{-3} deg. and no correction was therefore applied.

Taking into account these possible sources of error and possible inaccuracies in the 1949 scale of temperature, the final values of the temperature of the specimens can probably be considered reliable to within 10^{-2} deg.

(b) *Critical field.*

The effect on the earth's field was allowed for by making the measurements with the solenoid field alternately with and against the vertical component of the earth's field. In order to allow for the finite amplitude of the measuring field the peak value was added as a correction to the applied field. Measuring fields of between 0.5 and 5 gauss r.m.s. were used in the experiments and after the application of this correction results were obtained with an internal consistency of better than 0.5 gauss.

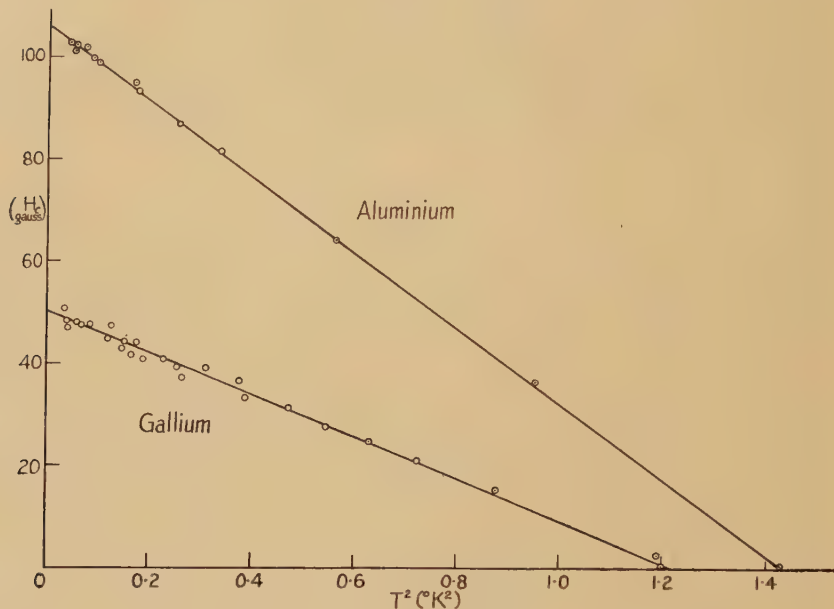
The main uncertainty of interpreting the critical field measurements lies in assessing the effect of strains and impurities in the specimen. Since the value of M_2 was determined by the currents flowing in the specimen and not by its magnetic moment it follows that the present method studies the electrical resistance of the specimen rather than its magnetization, and the effect of strains or impurities in the specimens is to give values of H_c which are larger than the true values. An estimate of the magnitude of this effect is provided by the behaviour of the zinc specimen. The effect of annealing was to reduce H_c at 0.2°K . by only 4 per cent while the breadth of the zero field transition was reduced from about 4×10^{-2} deg. to not more than 5×10^{-3} deg. If a single mechanism is responsible in a superconductor for the broadening of the zero field transition and for raising the critical field above its true value then it seems probable that systematic errors in the values of H_c for the annealed specimen of zinc due to this uncertainty do not amount to more than about 2 per cent. All the other specimens had zero field transitions at least as sharp as the zinc specimen, and it seems plausible to assume that errors in H_c values for those metals due to strains and impurities are of the same order of magnitude as for zinc.

§ 6. RESULTS.

It was found that the temperature variation of the critical fields could be represented by the formula $H_c = H_0(1 - (T/T_c)^2)$; this is illustrated in figs. 2 and 3 where H_c has been plotted against T^2 , and it can be seen that the points lie well on straight lines. Values of H_0 and T_c deduced from these graphs are given in Table II.

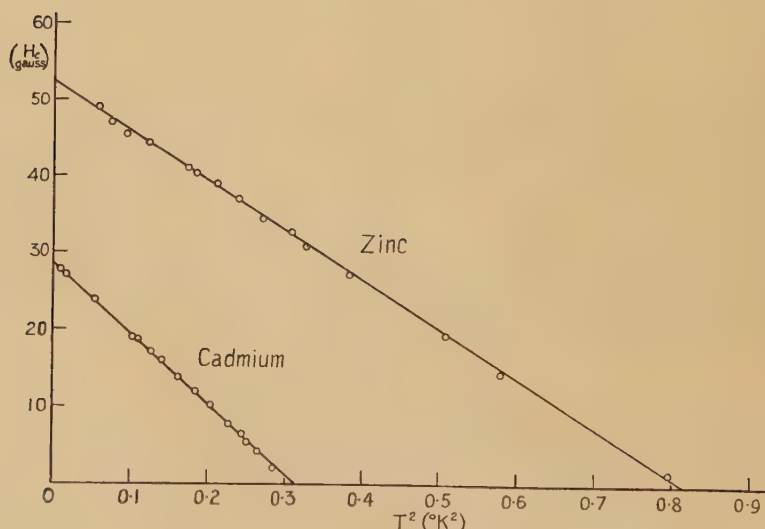
Measurements on aluminium and gallium have previously been made by Shoenberg (1940) and appear to differ appreciably from the present results. The discrepancies are much reduced however when due account is taken of the differences between the 1932 and 1949 scales of temperature,

Fig. 2.



Variation of H_c with T^2 for aluminium and gallium.

Fig. 3.



Variation of H_c with T^2 for cadmium and zinc.

and of the fact that no allowance was made in Shoenberg's measurements for the pressure drop between the liquid helium level and the top of the Dewar flask*. In fact, the diameter of his flask was only 9 mm. and a pressure drop of order 0.07 mm. of mercury could have been expected at the lowest temperatures, corresponding to an error in temperature determination of order 3×10^{-2} deg. Thus Shoenberg's measurements may be regarded as supporting the present results. Kurti and Simon (1935 b) obtained in measurements on cadmium $T_c = 0.54 \pm 0.02$ ° K. and an initial slope of the critical field curve of order 100 gauss deg.⁻¹; the present values of $T_c = 0.560$ ° K. and 103 gauss deg.⁻¹ respectively are in good agreement.

TABLE II.

	T_c (° K.)	H_0 (gauss)	$\gamma \times 10^4$ cal. mole. $^{-1}$ deg. $^{-2}$	$\frac{\gamma}{VT_c} \times 10^6$ cal. cm. $^{-3}$ deg. $^{-3}$	
			(a)	(b)	(a)
Aluminium	1.197	106.0	2.95	3.48*	24.9
Cadmium	0.560	28.8	1.28	—	17.9
Gallium	1.103	50.3	0.91	—	7.2
Zinc	0.905	52.5	1.16	1.25†	14.1
				1.5‡	

γ is the coefficient of T in the expression for the specific heat of the normal metal, and V is the atomic volume.

(a) Calculated from the present results.

(a) Calculated from the present results.
 (b) Calorimetric measurements: * Kok and Keesom (1937); † Keesom and van den Ende (1932) recalculated by Silvidi and Daunt (1950); ‡ Silvidi and Daunt (1950).

The values of H_c obtained by Daunt and Heer (1949 b) using Kurti and Simon's method are of order 4 gauss lower than the present results for aluminium and are of order 8 gauss higher than the present results for zinc. It therefore seems improbable that a single factor is responsible for these discrepancies. It is possible that the stresses the metal is subjected to when pressed into a pill with the salt may be responsible for the high values of H_c recorded for zinc. Furthermore, the difficulty of interpreting the complex magnetic behaviour of the mixed pills of salt and metal used may possibly be responsible for unsuspected errors in measuring both H_c and T.

The critical field measurements may also be compared with various calorimetric data. The difference in entropy per unit volume between the normal and superconducting states is given by the thermodynamical relation

$$s_s + s_n = \frac{H_c}{4\pi} \left(\frac{dH_c}{dT} \right).$$

* This possibility was pointed out to us by Dr. Shoenberg.

The experiments of Keesom and Kok (1934) on thallium and of Keesom and van Laer (1938) on tin suggest there is no linear term in the specific heat of a metal in the superconducting state. Therefore for those metals for which a relation of the type $H_c = H_0(1 + (T/T_c)^2)$ holds the linear term in the specific heat of the normal metal must be of the form $(VH_0^2/2\pi T_c^2)T$ erg mole.⁻¹ deg.⁻¹, where V is the molecular volume. Values of γ , the coefficient of T in this expression, calculated from the present results are in fair agreement with calorimetric data as can be seen from Table II.

Evidence for an empirical correlation among superconductors has recently been put forward by Daunt (1950). He observes from a plot of γ/V and T_c that the elements for which reliable information is available fall on one of two straight lines through the origin. In other words he suggests that $\gamma/V = KT_c$ where $K = 30 \times 10^{-6}$ cal. cm.⁻³ deg.⁻³ for the hard group of superconductors and $K = 6.7 \times 10^{-6}$ cal. cm.⁻³ deg.⁻³ for the soft superconductors. The values of γ/VT_c in Table II. calculated from the measurements on the four soft superconductors studied in this paper suggest that the correlation is at best only approximate.

ACKNOWLEDGMENTS.

We should like to thank Dr. J. Ashmead and Dr. D. Shoenberg for many valuable discussions, and Dr. C. G. B. Garrett for his practical assistance and advice. We have also to thank the Department of Scientific and Industrial Research for maintenance grants received while carrying out this work.

REFERENCES.

- CASIMIR, H. B. G., DE HAAS, W. J., and DE KLERK, D., 1939, *Physica*, **6**, 365.
- COOKE, A. H., 1949, *Proc. Phys. Soc. A*, **62**, 269.
- DAUNT, J. G., 1950, *Phys. Rev.*, **80**, 911.
- DAUNT, J. G., and HEER, C. V., 1949 a, *Phys. Rev.*, **76**, 715 ; 1949 b, *Ibid.*, **76**, 1324.
- VAN DIJK, H., and SHOENBERG, D., 1949, *Nature, Lond.*, **164**, 151.
- KEESOM, W. H., and VAN DEN ENDE, J. N., 1932, *Commun. Phys. Lab. Univ. Leiden*, No. 219 b ; *Proc. Roy. Acad., Amsterdam*, **35**, 143.
- KEESOM, W. H., and VAN LAER, P. H., 1938, *Physica*, **5**, 193.
- KEESOM, W. H., and KOK, J. A., 1934, *Physica*, **1**, 175.
- KOK, J. A., and KEESOM, W. H., 1937, *Physica*, **6**, 835.
- KURTI, N., and SIMON, F. E., 1935 a, *Proc. Roy. Soc. A*, **149**, 152 ; 1935 b, *Ibid.*, **151**, 610.
- MENDOZA, E., 1948, *Cérémonies Langevin-Perrin, Paris*, 53.
- SHOENBERG, D., 1940, *Proc. Camb. Phil. Soc.*, **36**, 85.
- SILVIDI, A. A., and DAUNT, J. G., 1950, *Phys. Rev.*, **77**, 125.

LXIII. A Mechanical Kick-sorter (Pulse Size Analyser).

By S. G. F. FRANK, O. R. FRISCH and G. G. SCARROTT.
Cavendish Laboratory, Cambridge*.

[Received March 15, 1951.]

SUMMARY.

This instrument serves to obtain the size distribution of electric pulses coming, for example, from an ion chamber or counter. Each pulse causes a small steel ball to be propelled along an inclined board; the ball describes a parabolic path and lands in one of 30 parallel grooves. As balls accumulate in the grooves a histogram of the pulse size distribution is built up.

The paper describes the mechanical construction and the associated electronic circuits. The latter serve, among other things, to eliminate pulses which are either too large or too small to be recorded, or which follow too close upon the last recorded pulse.

INTRODUCTION.

A KICK-SORTER (or pulse size analyser, also pulse spectrograph) serves to obtain the amplitude distribution of electric pulses, *e.g.* from an ion chamber or proportional counter. The pulses must first be amplified by a standard pulse amplifier (see Sands and Elmore 1949); the kick-sorter then sorts them into a number of channels (size groups), recording the number in each channel separately.

It occurred to one of us (O. R. F.) in 1947 that a mechanical system might be cheaper and more reliable than the usual electronic gear which involves a great many valves (usually several per channel). In the meantime electronic kick-sorters have been much improved (see in particular Wilkinson 1950, Hutchinson and Scarrott 1951), but the instrument described here (in use since 1949) has still some advantages, chiefly cheapness and the fact that the information it contains is displayed as a histogram all the time. Its main disadvantage is low storage capacity (about 100 per channel) and slowness: pulses are sorted at most at the rate of about 6 a second. However, in many cases that is enough.

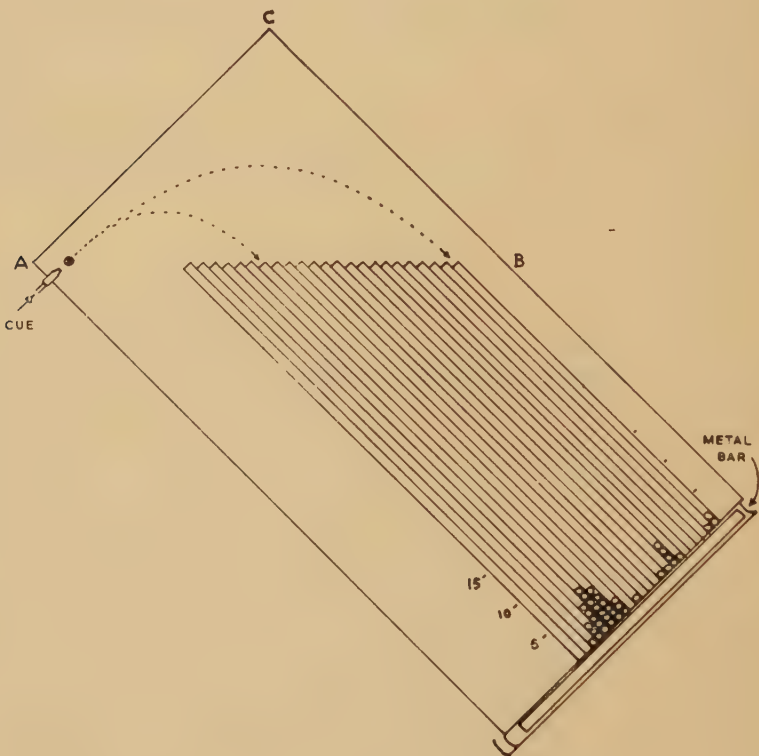
GENERAL DESCRIPTION.

Each pulse suitable for recording (see later) causes a steel ball ($\frac{1}{8}$ in. diameter) to be propelled along an inclined board (1) with 30 parallel grooves (fig. 1). The ball describes a parabolic path and lands in one groove, depending on its initial speed which in turn depends on the

* Communicated by the Authors.

amplitude of the pulse. As balls accumulate in the grooves a histogram of the pulse size distribution is built. Immediately after one ball has been fired a new one is deposited by an electrically operated "feeder" (2). The balls are projected by a little "billiard cue" (3) mounted on a coil which is driven like the coil in a dynamic loudspeaker. The current pulse which makes the coil move, and the one which actuates the feeder, come from the electronic pre-sorter (4) which contains some twenty valves. Here the pulses issuing from the standard amplifier are first lengthened (4.1) to $100 \mu\text{sec}$.; if they are bigger than an adjustable

Fig. 1.

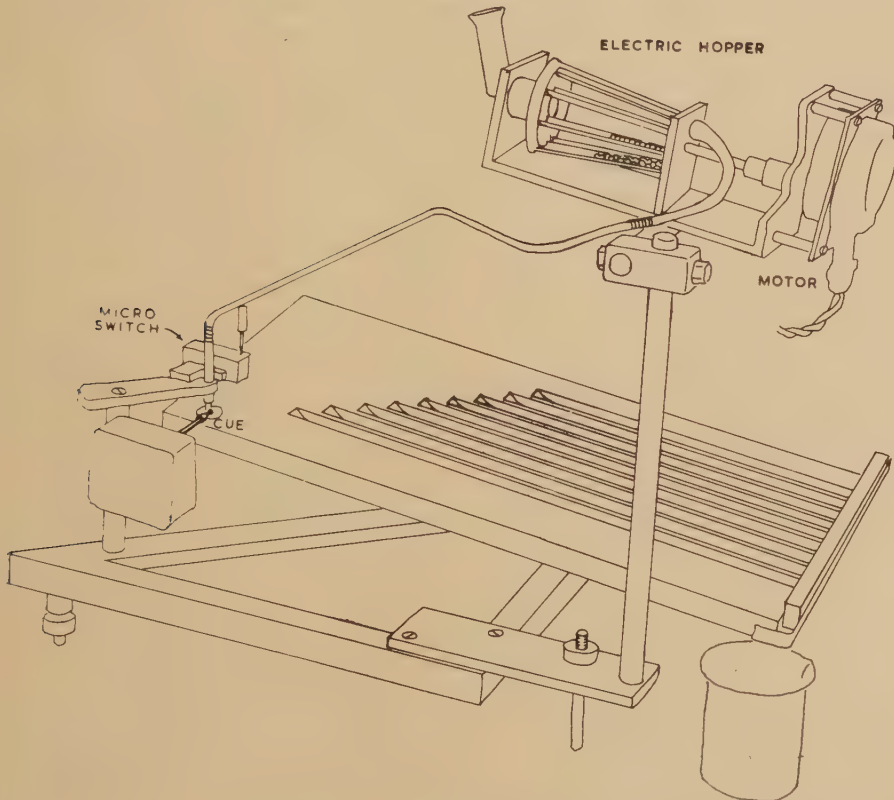


bias B their excess over B is then further amplified (4.2). The next section (4.3) selects pulses whose amplitudes lie within a certain range; the limits of this range can be adjusted so that they correspond to the first and the last groove on the board. The waiting-time unit (4.4) closes a gate after each pulse, for a time T (0.1 to 0.2 seconds) which is adjusted to make sure that the next pulse does not arrive before the next ball is in position to be fired. The output unit (4.5) lengthens the pulse further and gives it enough power to drive the billiard cue; it also produces a suitable pulse to actuate the "feeder".

DETAILED DESCRIPTION.

1. *The Board* (see figs. 1 and 2) was made of polystyrene, 23 cm. by 48 cm., $\frac{1}{2}$ in. thick. Thirty grooves just over $\frac{1}{8}$ in. wide and $\frac{1}{8}$ in. deep were cut in with a miller; this tapers the upper end of the groove and allows the ball to enter without bouncing. The board is mounted on three adjustable legs and is tilted by about 10 degrees in such a way that the line AB remains horizontal. The balls are propelled parallel to AC and hence describe parabolas each of which enters the appropriate

Fig. 2.



groove without a break. If a ball describes a parabola which leads to the ridge between two grooves, then it will be caught in the lower groove a little lower down.

At the lower end the grooves are closed by a removable metal bar. As more and more balls accumulate in the grooves, they build up a histogram of the pulse size distribution. Lines corresponding to 5, 10, 15 etc. ball diameters are drawn on the board so that the number of balls in each groove can be quickly read off after a run. This done, the metal bar is removed, and the balls run out into a gutter and from there into a beaker, ready to be used again.

On dry days the top ball in a groove often comes to rest several millimetres above the remainder, presumably due to electric charge acquired by friction. Such a charge may slightly influence the path of the ball though we have no evidence that it does. A board made of metal rather than polystyrene would eliminate this.

2. *The feeder* is a simple escape mechanism, connected to the armature of a small electromagnet (a commercial relay). When the armature is attracted the lowest ball is released; on the return motion the whole line of balls in the feeding tube is allowed to advance one unit, making a fresh ball ready for release. On being released, the ball drops by about $1\frac{1}{2}$ diameters, on the spot from which its predecessor has just been fired.

To prevent bouncing, the platform on which the ball drops is a mica membrane cemented over a metal ring and smeared thickly with grease from below. This has proved very durable and is remarkably bounce-free; balls are stopped dead even if dropped from a height of several inches. There is some slight bouncing from the two locating posts which prevent the balls from rolling off. This could probably be improved by suitable design of the posts, and then a waiting time of 0.05 seconds between balls should suffice. As it is, we find operation getting erratic if the waiting time is made shorter than 0.15 second.

The feeding tube can only hold a few dozen balls, otherwise the pressure on the release mechanism gets too heavy. The electrically operated hopper shown can store many hundred balls and is very reliable. It consists of a hollow cone (its walls transparent for convenience) with a number of scoopers on its inside. The cone is slowly turned by a small motor and gear (4 revs./min.). Each scooper picks up some twenty balls, carries them to the top where it becomes suitably inclined because of the conical arrangement, and feeds them into the feeding tube. The latter has a crooked section which is hinged to the remainder by two short lengths of spiral spring (or soft rubber tube). When this section contains enough balls it presses upon a microswitch and turns off the motor which drives the hopper; when it is partly emptied the motor starts again.

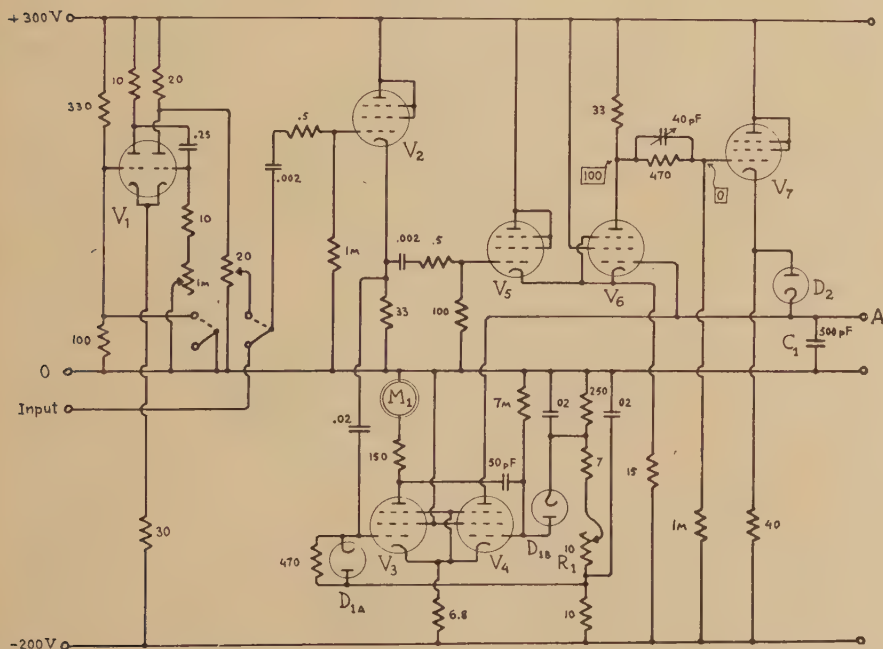
3. The propelling mechanism is a little billiard cue, driven electro-dynamically. The tip of the cue was made of polystyrene and seems quite satisfactory. The shaft is an aluminium rod, 2 mm. thick, threaded over its whole length (of about 7 cm.). It is clamped, with the help of four nuts, onto two V-shaped supports of beryllium copper foil so that it can move lengthwise only. Its other end is screwed on the driving coil (22 mm. diameter, 800 turns of 48 S.W.G. enamelled wire) which moves in the annular gap of a commercial loudspeaker magnet.

When the cue strikes it gives the ball a velocity which is in a fixed proportion to its own (twice if the cue were much heavier than the ball, and perfectly elastic). The distance the ball will travel is proportional to the square of its speed (neglecting friction). In order to make that distance proportional to the pulse amplitude the speed of the ball (and

hence that of the cue as it strikes) must be proportional to the square root of the pulse amplitude. This will be so if the cue is uniformly accelerated from rest until it touches the ball, by a force proportional to the pulse amplitude. To achieve uniform acceleration, one has to avoid all damping and friction; yet the return motion ought to be damped to avoid bouncing. This damping was produced by a 5 Kohm resistor parallel to the coil, the resistor being in series with a diode which becomes conducting during the return motion only.

4. The valves of the electronic presorter are contained in one standard chassis; a second chassis contains a power supply of standard design, supplying +300 volts (up to 300 mA.) and -200 volts (up to 150 mA.), both stabilized.

Fig. 3.

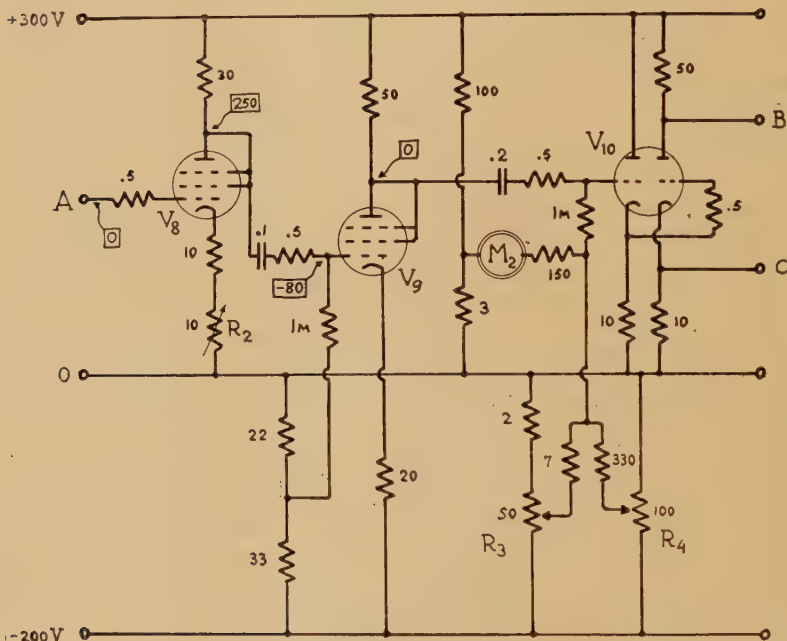


Standard pulse generator and pulse lengthener. All resistances are in kilohm and capacities in μF except where otherwise stated. M means megohms pF means $\mu\mu\text{F}$; numbers given thus [20] indicate steady state voltages.

4.1. (See fig. 3.) The input pulses must be positive and between 7 and 50 volts in size. They come either from the input terminal or else from a multivibrator (valve V_1) which produces standard pulses of adjustable amplitude and recurrence frequency, for testing. After being fortified by a cathode follower (valve V_2) those which are larger than a certain preset value (adjustable through R_1) trigger the valve pair 3-4 whereby valve 4 is rendered non-conducting for about 100 μ sec. At the

same time, as the potential of the control grid of V_5 rises with the pulse, the difference between it and the potential at A is amplified by V_6 and causes V_7 to produce current which tends to abolish this potential difference. Thus A follows the pulse until it reaches its maximum; thereafter D_2 ceases to conduct, and C_1 remains charged to the amplitude of the input pulse until valve V_4 becomes again conducting. In this way each input pulse (provided it is large enough) produces at the point A a voltage equal to its own peak voltage, remaining constant for about 100 μ secs. and then returning to zero. R_1 is adjusted so as to exclude noise pulses, yet to include all pulses which we want to analyse. The

Fig. 4.



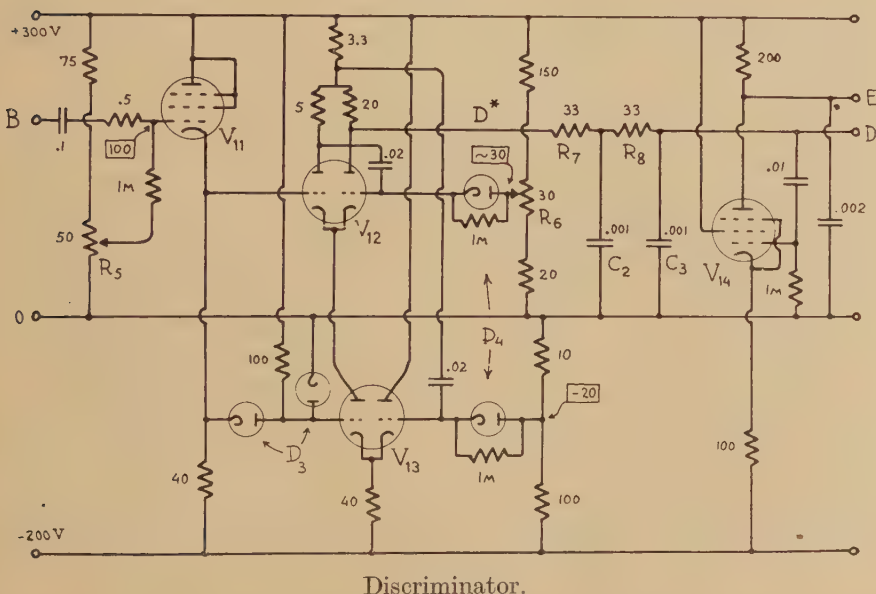
Amplifier and biased amplifier.

meter M_1 averages the current through V_3 and thus indicates the rate at which pulses pass this hurdle: this rate should not exceed about 200 pulses per second or else some bias levels will shift.

4.2. (See fig. 4.) Valves V_8 and V_9 form an amplifier with a gain of about 4 (adjustable through R_2). The first half of valve V_{10} is a biassed cathode follower (which will not draw grid current, even for large pulses), feeding the second half, a triode amplifier of gain 5. The (negative) bias has coarse and fine adjustment (R_3 and R_4) and is indicated on the meter M_2 . Pulses below a certain minimum size (which depends on the bias) are not amplified by this arrangement; of larger pulses, the portion exceeding the minimum size is linearly amplified and appears at the point B, now as negative pulses.

4.3. (See fig. 5.) After passing through valve V_{11} which serves to adjust (through R_5) the D.C. level, the pulses are supplied, in parallel, to the double triodes V_{12} and V_{13} . V_{12} forms a trigger circuit which will produce a certain negative potential on point D^* if the potential on its left-hand grid drops below a certain level v_1 , adjustable through R_6 . However, if the pulse is so large that it drops below v_2 , then V_{13} is triggered as well; the current in V_{12} is thereby turned off and point D^* becomes positive again. In this case only a very brief negative pulse is produced, which is filtered out by the low-pass network $R_7C_2R_8C_3$. Thus a negative pulse of standard size, somewhat delayed and rounded off by the low-pass network, is produced at point D every time the input pulse has an amplitude between v_1 and v_2 . These "control pulses"

Fig. 5.



Discriminator.

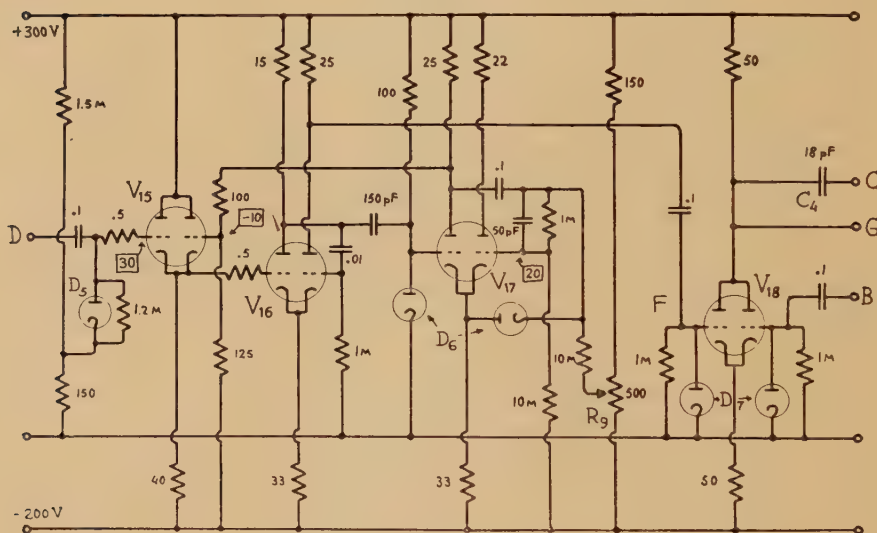
can be counted by an external scaler connected to the terminal E . They serve, furthermore, to open a gate (see 4.5) which admits the pulse proper to the output valve.

4.4. (See fig. 6.) The waiting time T is determined by the time constant (adjustable through R_9) of the trigger circuit formed essentially by valve V_{17} . When triggered, this circuit renders conducting the right-hand half of valve V_{15} , thus preventing further control pulses from getting through until the waiting time is over. If the control pulse does get through it is sharpened and reversed by the trigger circuit V_{16} . Its leading edge places positive charge on the left-hand grid of valve V_{17} ; its trailing edge triggers it and "shuts the door behind itself", for a time sufficient to allow another ball to be placed in position to be fired.

Thus a negative control pulse arrives at point F only if the pulse at point B has an amplitude between v_1 and v_2 , and if the time elapsed since the arrival of the last control pulse is at least T. Valve 18 acts as a gate which allows the pulse from point B to pass on only if a control pulse arrives at the same time at F. (C_4 is a neutralizing condenser.)

4.5. (See fig. 7.) The output pulse, taken from the anodes of V_{18} and hence positive once more, now has to be lengthened to about 20 millisecs., longer than the longest time required by the billiard cue to complete its motion towards the ball. For this, the pulse is made to charge the condenser C_5 (by means of the cathode follower valve 19, and the diode D_{8A}) while triggering the double triode V_{20} , which discharges C_5

Fig. 6.



Time veto and gating circuits.

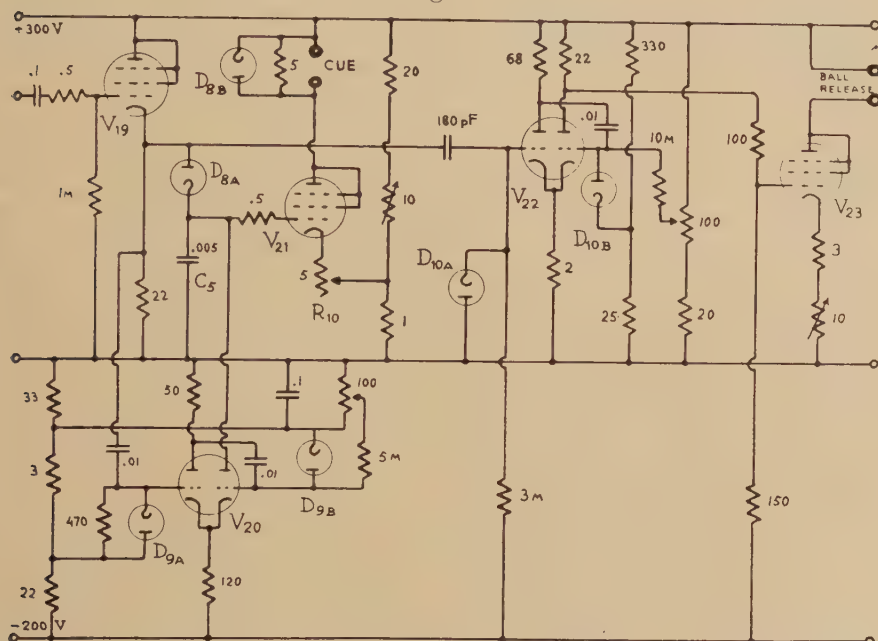
on returning to its untriggered condition. The lengthened pulse is fed to the output valve V_{21} , while the (unlengthened) pulse triggers V_{22} , producing a standard square pulse which, through V_{23} , operates the ball release.

OPERATION.

In order to get reproducible results it is important to keep both the balls and the board very clean. The balls are washed periodically in acetone, while the board is wiped with dry cotton wool to remove any dust. The distance of the tip of the cue from the resting steel ball must be sufficient (about 3 mm.) for the ball to be projected into the furthest groove without driving the output valve V_{21} into grid current.

A number of electronic adjustments have to be made before the kick-sorter can be used. R_2 is first adjusted so that an amplification factor of 4 is obtained between the input pulse and the pulse appearing at the input to the biased amplifier (V_{10}). M_2 will then indicate how much voltage the bias removes from the original pulse height. Next R_6 (section 4.3) is adjusted so that the range of pulses admitted corresponds to 5 volts at the input terminals. When these adjustments have been made it is necessary to arrange for the smallest pulse to fire its balls into groove 1 and the largest one into groove 30. This requires a combination of adjustments of R_5 and R_{10} . R_5 adjusts the ratio of the smallest to

Fig. 7.



Final pulse lengthener and output valves.

largest pulse passed, R_{10} just varies the absolute magnitude of the output pulse. R_5 and R_{10} have to be adjusted alternately by successive approximations.

When clean the kick-sorter will remain stable to one channel after the initial warming up period and will fire between 80 per cent and 90 per cent of the balls into one groove with a standard pulse, the remaining balls being distributed over the two adjacent grooves.

One of us (S. G. F. F.) wishes to thank the Department of Scientific and Industrial Research for a maintenance grant.

REFERENCES.

- HUTCHINSON, G. W., and SCARROTT, G. G., 1951, *Phil. Mag.*, **42** (in the press).
WILKINSON, D. H., 1950, *Proc. Camb. Phil. Soc.*, **46**, 508.

LXIV. *A Localizing Geiger Counter.*

By S. G. F. FRANK,
Cavendish Laboratory, Cambridge*.

[Received March 15, 1951.]

SUMMARY.

The constant speed with which the discharge spreads along the wire in a Geiger counter is used to localize ionizing particles. Signals are obtained from the wire and also from two electrodes near its ends; from these signals a pulse is derived whose amplitude indicates the position of the initial ionizing event. Provision is made for stabilizing the speed of spread.

THIS instrument determines the position of the initial ionizing event along the length of a Geiger counter, with an error of less than 1 cm. Its operation is based on the fact that the discharge in a Geiger counter spreads along the central wire in both directions with a constant velocity of about 10 cm. per micro-second. The time which elapses between the start of the discharge and its arrival at one end of the counter is therefore proportional to the distance of the original ionizing event from that end of the counter. Furthermore the sum of the times taken by the discharge to reach both ends of the counter should be independent of the position of the ionizing event, and this serves as a check on the correct operation of the counter.

To obtain all the required information about the discharge, two small auxiliary cathodes of about 1 cm. length and 2 mm. diameter are placed at the two ends of the anode. Their potential is adjusted to that of the equipotential which they occupy in the counter. At the start of the discharge a sharp negative pulse is obtained from the anode by differentiation, using a 1000 ohm resistance earthed through a $0.25\ \mu\text{F}$. condenser. Two positive pulses are obtained directly from the two auxiliary cathodes when the discharge reaches the two ends of the counter. All three pulses are fed into head amplifiers, which produce positive output pulses. These are then amplified by identical wide-band amplifiers which operate three fast trigger circuits (see fig. 1). The trigger circuit (b) actuated by the anode produces a *negative* square wave lasting about 20 microseconds. The trigger circuits (a) and (c) actuated by the auxiliary cathodes produce similar *positive* pulses lasting about twice as long. Pulses from the triggers (a) and (b) pass through an "interval converter" which generates a signal p_1 whose amplitude is proportional to the time interval between the onset of the pulses from

* Communicated by Professor O. R. Frisch, F.R.S.

(a) and (b) and hence to the distance of the ionizing event from the "upper" end of the counter. In the same way a pulse p_2 is obtained, proportional to the distance of the ionizing event from the other end of the counter.

Fig. 2 shows the electronics in the blocks (a) and (1). The first pentode (head amplifier) is placed close to the counter; the next three pentodes

Fig. 1.

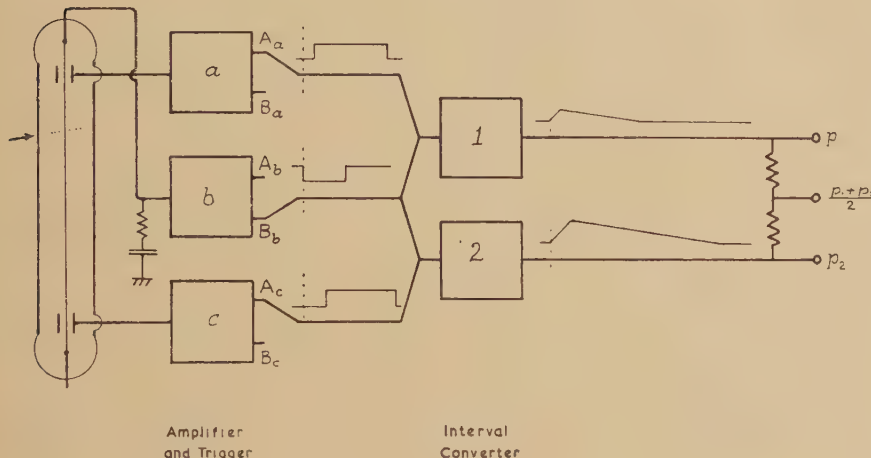
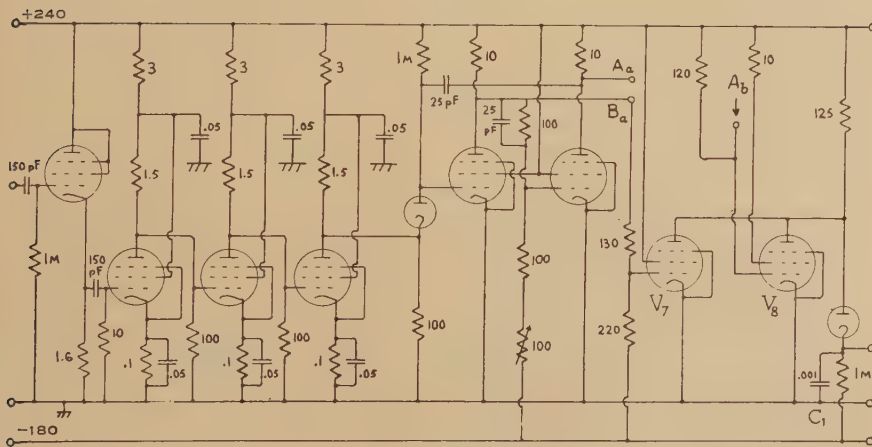
Interval
Converter

Fig. 2.



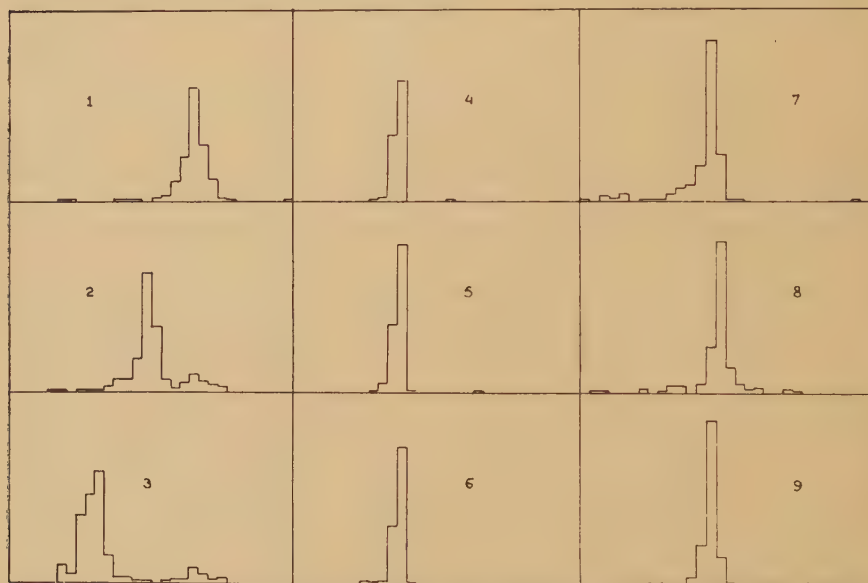
form a fast amplifier which is coupled through a diode to the trigger circuit, comprising the next two pentodes. The last two pentodes and the last diode form the interval converter (1), which works as follows. The pulse from trigger (b) cuts off the valve (8); this allows the condenser C_1 to charge up through a diode and a $125\text{ k}\omega$ resistor until the positive pulse from (a) brings valve (7) into conduction. The voltage

in C_1 is kept small compared to 240 volts, and therefore rises linearly in the time between pulse (a) and pulse (b). Thereafter C_1 is discharged (much more slowly) through a 1 megohm resistor to the bias line.

The electronics in block (c) is entirely similar; in block (b) it differs in that the first pentode is used not as a cathode follower but as a phase inverter, with an anode resistor of $1.6\text{ k}\omega$, and that the required positive signal for both interval converters comes from point A, not B, as shown in fig. 1.

The propagation velocity of the discharge increases with increasing over-voltage. It is thus possible to control the over-voltage of the counter in such a way as to keep $p_1 + p_2$ constant. This stabilizes the

Fig. 3.



Pulse size distributions obtained from localizing counter. Diagrams 1, 2, 3 : pulse p_1 , with β -source at 5 cm., 12 cm. and 19 cm. respectively, from "lower" end of counter.

Diagrams 4, 5, 6 : pulse $\frac{1}{2}(p_1 + p_2)$ for the same source positions as in diagrams 1, 2 and 3 respectively.

Diagrams 7, 8, 9 : pulse p_1 with α -source at 2, 12 and 22 cm. from end of counter. A bias of 6.9, 4.9 and 2.9 V. respectively was used to keep the group near the centre; 1 volt bias means a shift of six channels.

constant of proportionality relating both p_1 and p_2 to the position of the ionizing event, and also serves to keep the counter in the correct operating condition. To get the sum of the two pulses they are applied to the two ends of a resistor, from the centre of which a pulse equal to $\frac{1}{2}(p_1 + p_2)$ is then obtained. The circuit used to control the over-voltage is similar to that designed by D. H. Wilkinson (1950) for the stabilization of proportional counters.

The counter used had brass walls with an internal diameter of about 3·8 cm., and an active length of about 25 cm. ; it was fitted with a narrow mica window extending over the whole of its active length, had a tungsten anode of 0·1 mm. diameter, and was filled with 10 cm. pressure of argon and 1·5 cm. of alcohol vapour. To test it a beam of β -particles about 2 mm. wide was directed at the counter window at various points along the counter. The pulses were analyzed with a 30-channel kick-sorter (Frank, Frisch and Scarrott 1951) and the results are shown in fig. 3. The small subsidiary group shown on diagrams 2 and 3 is thought to be due to spurious counts originating at that point of the counter.

The spread of the individual pulse groups is much greater than that of the groups due to p_1+p_2 (see diagrams 4, 5 and 6) ; hence it could not have been due to any shortcomings of the instrument, but perhaps to scattering of the incoming β -particles at the window. To test this another similar counter was made with a thin enough window to admit α -particles which would be scattered very much less. Indeed the groups were very much sharper, as shown on diagrams 7, 8 and 9. In this case one channel width on the kick-sorter corresponds to about 8 mm. along the Geiger counter, and it is seen that localization is possible with a standard error of less than 1 cm.

My thanks are due to Professor Frisch who suggested this work, to Mr. G. G. Scarrott for his advice about the electronics, and to the Department of Scientific and Industrial Research for a grant.

REFERENCES.

- FRANK, S. G. F., FRISCH, O. R., and SCARROTT, G. G., 1951, *Phil. Mag.*, **42**, 603.
WILKINSON, D. H., 1950, *J. Sci. I.*, **27**, 36.

LXV. *The Development of Deformation Textures in Metals.—Part II. Body-Centred Cubic Metals.*

By E. A. CALNAN and C. J. B. CLEWS,
National Physical Laboratory *.

[Received February 19, 1951.]

§1. INTRODUCTION.

THE aim of the present treatment is to explain the development of deformation textures in polycrystalline aggregates from the behaviour of their single crystals, while at the same time attempting to overcome certain difficulties and limitations of previous methods. Its application to face-centred cubic metals led to the prediction of the polycrystalline stress-elongation curve, and, in a qualitative fashion, to the preferred orientations resulting from tension, compression, rolling, and wire drawing operations, (Calnan and Clews 1950, subsequently referred to as Part I.). It was shown that these predictions are in reasonable accord with experimental observations, although the latter are by no means comprehensive.

It has been shown (Mises 1928, Taylor 1938) that, in the idealized case of homogeneous deformation, multiple slip, *i.e.* slip on three or more systems, must take place in order to preserve the external form of the specimen and to maintain cohesion at the grain boundaries. It is now postulated that for this multiple slip to occur the stress system within a grain or part of a grain must be such as to give equal resolved shear stresses on all the operative slip systems. The simplest stress system satisfying this condition is a single tensile stress, previously referred to in Part I. as the effective stress, T_e , lying, in the case of a face-centred cubic metal, in a [100], [110] or [111] direction. In the initial condition with perfectly annealed material, at the instant of application of a small applied tensile stress, T_a , the effective stress direction is coincident with the direction of this applied stress. As soon as elastic deformation takes place intergranular stresses generally come into play. If the applied stress is then increased and slip does not occur when the applied stress resolved on the most favourable slip system reaches the critical value for slip, then T_e must have moved away from T_a in such a direction as to reduce the resolved shear stress on this system. With further increase in the applied stress, provided no slip has occurred, T_e continues to move until it reaches one of the minimum positions of resolved shear stress, which are, of course, the points of multiple slip already referred to above. Having arrived at such a position, no further movement of T_e is possible and there must be slip on all the symmetrically disposed equivalent systems when the critical stress is reached. Slip will frequently occur, however, before this condition is attained; there will be single slip if T_e is within the reference

* Communicated by the Authors.

stereographic unit triangle, or duplex slip if T_e is on a boundary between two equivalent slip systems. The operation of slip relieves the intergranular stresses and the whole sequence above recommences. Thus the deformation of a single grain or part of a grain within the polycrystalline mass is visualized as a discontinuous process made up of elements of multiple, duplex, and single slip. It is clear that inhomogeneous deformation is implicit in this treatment.

Due to the symmetrical disposition of the equivalent slip systems at the positions of multiple slip there is no grain rotation and the development of preferred orientation thus depends on the rotations resulting from single and duplex slip. Consequently, in order to produce the high degree of preferred orientation observed after extensive deformation, there must be a considerable amount of single and duplex slip, although some multiple slip is necessary to retain both cohesion at the boundaries and specimen shape.

These concepts, described in greater detail in Part I., have now been applied to the more complex case of the deformation of a body-centred cubic metal where slip can occur on systems of the types $\{110\}\langle111\rangle$, $\{112\}\langle111\rangle$, or $\{123\}\langle111\rangle$. Andrade and his co-workers (1940), who have made an extensive study of the slip systems in body-centred cubic metals, find that the slip direction $\langle111\rangle$ is invariate but that the slip plane depends on the temperature in such a way that it is the same for many metals for the same ratio of test temperature, T , to melting temperature, T_m (Table I.).

TABLE I.
Slip Planes in Body-Centred Cubic Metals.

Metal	Slip plane	T/T_m
Mo, W, Na	112	0.08 to 0.24
β -brass, Mo, Na	110	0.26 to 0.50
Na, K	123	0.80 to 0.87

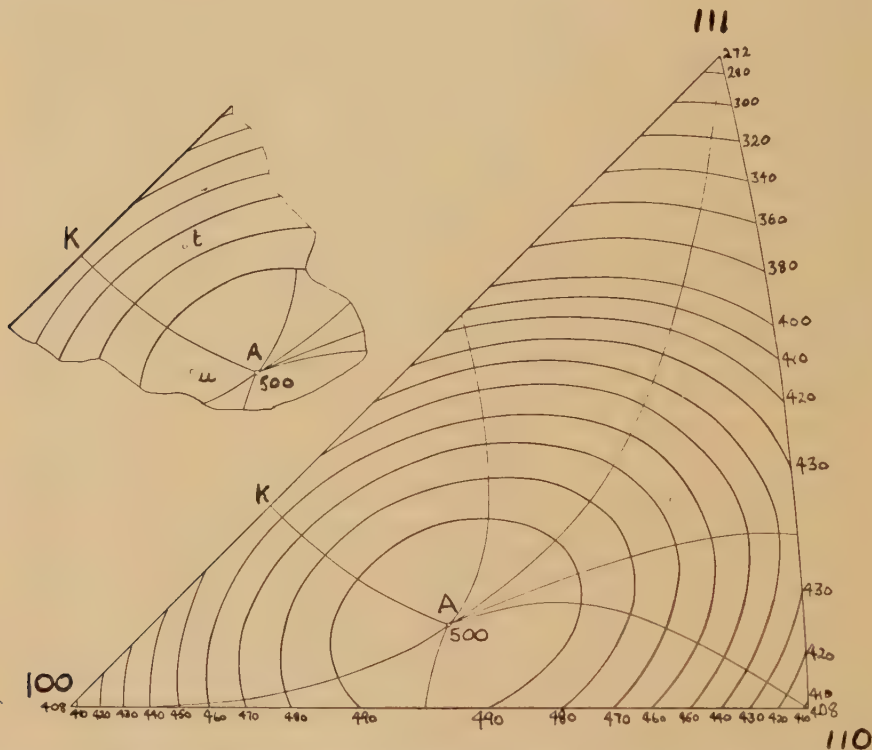
The systems operative in α -iron have been studied by Barrett, Ansel and Mehl (1937 a), who find that slip takes place on all three planes at temperatures between $20^\circ C.$ and $-195^\circ C.$ Silicon ferrite, deformed at low temperatures or containing more than 4 per cent silicon, slips only on $\{110\}$ planes. In conditions where all three planes are operative, however, the ratio of the critical shear stresses for $\{110\}$, $\{112\}$, and $\{123\}$ slip, determined by Smoluchowski and Opinsky (1950), is 100 to 103 to 105.

Deformation textures have been derived for each of the three slip planes operating independently, for the three systems simultaneously operative with equal critical shear stresses, and for the three systems with critical shear stresses in the ratios referred to above.

§ 2. MAXIMUM RESOLVED SHEAR STRESS DIAGRAMS.

Values of the function $\cos \chi \cos \lambda$, where χ and λ are respectively the angles which the slip direction and the slip plane normal make with any particular direction of applied stress, have been tabulated at 1° intervals over ranges of α and β from 0° to 90° ; α is the angle of co-latitude and β the angle of longitude of the pole of the stress direction on a standard stereographic projection. They have been calculated to three figures on Hollerith machines by the Mathematics Division of the National Physical Laboratory.

Fig. 1,



Maximum resolved shear stress contours, to three decimal places, plotted on a standard stereographic unit triangle for the systems $\{110\}\langle 111 \rangle$ and $\{111\}\langle 110 \rangle$. Some lines of quickest descent from the maximum at A are also shown.

Contour diagrams of these functions for $\{110\}$, $\{112\}$ and $\{123\}$ systems have been published previously by Fahrenhorst and Schmid (1932). The justification for reproducing the diagrams based on these new tables lies not only in their greater accuracy but also in that they reveal some features overlooked in these earlier diagrams.

$\{110\}\langle 111 \rangle$ and $\{111\}\langle 110 \rangle$ Systems.

From the point of view of the evaluation of the function $\cos \chi \cos \lambda$ these two systems are of course identical, although they are different

crystallographically. The system $\{111\}\langle110\rangle$, *i.e.* slip on $\{111\}$ planes in $\langle110\rangle$ directions, has been considered in Part I. The related system $\{110\}\langle111\rangle$, slip on $\{110\}$ planes in $\langle111\rangle$ directions, is required in the present discussion. The maximum resolved shear stress contours are shown in fig. 1. The most favourable system, that corresponding to these maximum resolved shear stress values, is the $(101)[1\bar{1}\bar{1}]$ throughout the unit triangle. Along the edges of the unit triangle the maximum resolved shear stress is found on two symmetrically placed systems, while at the corners of the triangle the maximum value is on four, six or eight equivalent systems (Table II.).

TABLE II.
Most Favourable $\{110\}\langle111\rangle$ Slip Systems.

	Slip systems	Number
Unit triangle	$(101)[1\bar{1}\bar{1}]$.	1
Boundary $[100][110]$	$(101)[1\bar{1}\bar{1}]$, $(10\bar{1})[111]$.	2
Boundary $[100][111]$	$(101)[1\bar{1}\bar{1}]$, $(110)[1\bar{1}\bar{1}]$.	2
Boundary $[110][111]$	$(101)[1\bar{1}\bar{1}]$, $(011)[1\bar{1}\bar{1}]$.	2
Point $[110]$	$(101)[1\bar{1}\bar{1}]$, $(10\bar{1})[111]$, $(011)[1\bar{1}\bar{1}]$, $(011)[111]$.	4
Point $[111]$	$(101)[1\bar{1}\bar{1}]$, $(10\bar{1})[1\bar{1}\bar{1}]$, $(011)[111]$, $(011)[1\bar{1}\bar{1}]$, $(110)[111]$, $(110)[1\bar{1}\bar{1}]$.	6
Point $[100]$	$(101)[1\bar{1}\bar{1}]$, $(10\bar{1})[1\bar{1}\bar{1}]$, $(110)[1\bar{1}\bar{1}]$, $(110)[1\bar{1}\bar{1}]$, $(10\bar{1})[111]$, $(10\bar{1})[1\bar{1}\bar{1}]$, $(110)[111]$, $(1\bar{1}\bar{0})[11\bar{1}]$.	8

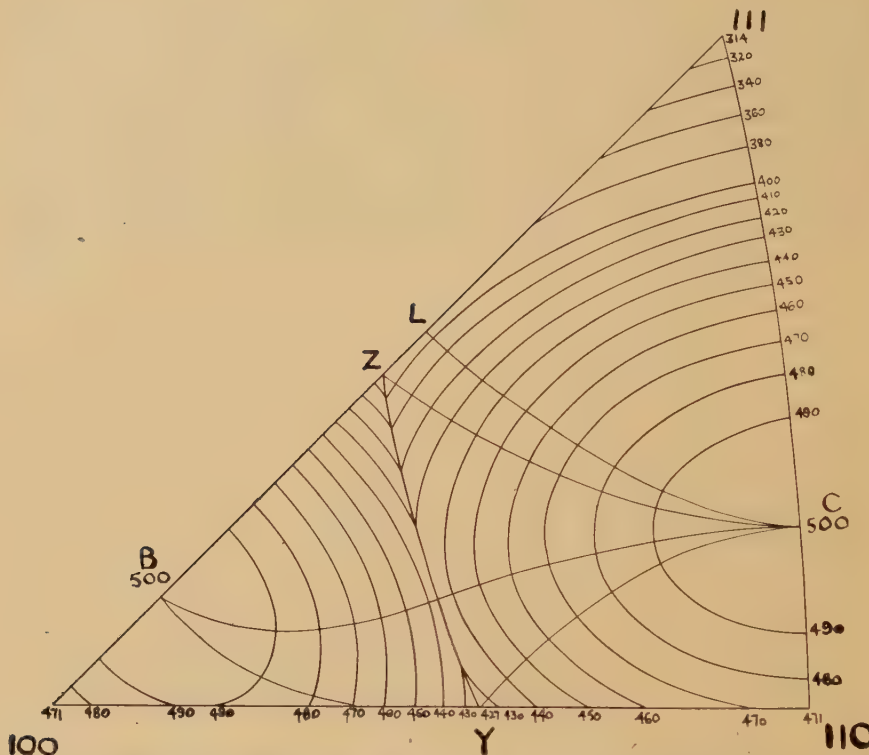
$\{112\}\langle111\rangle$ System.

The maximum resolved shear stress contours for the $\{112\}\langle111\rangle$ system are shown in fig. 2. This case is not as simple as the previous one, in that the same slip plane and direction are not the most favourable throughout the unit triangle. In the area $[100]YZ$ the operative plane and direction are $(2\bar{1}\bar{1})$ and $[111]$ respectively, while in the area $[111][110]YZ$ they are (112) and $[11\bar{1}]$. Along the line YZ the resolved shear stresses for these two systems are equal. The most favourable slip planes and directions at triangle edges and corners are listed in Table III. It should be noted that the maximum number of most favourable equivalent systems is four, occurring at $[100]$ and Y .

The position of the boundary YZ between the two systems may be determined geometrically as follows. Consider the general case of two slip systems $(p_1q_1r_1)[p_2q_2r_2]$ and $(p_3q_3r_3)[p_4q_4r_4]$. At any point of indices h, k, l the resolved shear stress on the system $(p_1q_1r_1)[p_2q_2r_2]$ is equal to $\cos \chi \cos \lambda$, where χ and λ are respectively the angles which the slip direction $[p_2q_2r_2]$ and the slip plane normal $[p_1q_1r_1]$ make with the direction $[hkl]$. $\cos \chi \cos \lambda$ is therefore equal to

$$\frac{hp_1+kq_1+lr_1}{\sqrt{(p_1^2+q_1^2+r_1^2)}\sqrt{(h^2+k^2+l^2)}} \cdot \frac{hp_2+kq_2+lr_2}{\sqrt{(p_2^2+q_2^2+r_2^2)}\sqrt{(h^2+k^2+l^2)}} = P. \quad \dots \quad (1)$$

Fig. 2.



Maximum resolved shear stress contours for the system $\{112\}\langle 111 \rangle$, showing some lines of quickest descent from the maxima at B and C, and the boundary YZ between regions of different operative slip planes and directions.

TABLE III.
Most Favourable $\{112\}\langle 111 \rangle$ Slip Systems.

	Slip systems	Number
Area $[100]YZ$	$(2\bar{1}1)[111]$.	1
Area $[111][110]YZ$	$(112)[11\bar{1}]$.	1
Boundary $[110]Z$	$(2\bar{1}1)[111]$.	1
Boundary $[110][111]$	$(112)[11\bar{1}]$.	1
Boundary $[100]Y$	$(2\bar{1}1)[111]$, $(211)[11\bar{1}]$.	2
Boundary $[110]Y$	$(112)[11\bar{1}]$, $(112)[111]$.	2
Boundary $[111]Z$	$(112)[111]$, $(121)[1\bar{1}1]$.	2
Boundary YZ	$(2\bar{1}1)[111]$, $(112)[11\bar{1}]$.	2
Point $[110]$	$(112)[11\bar{1}]$, $(112)[111]$.	2
Point Z	$(112)[11\bar{1}]$, $(121)[1\bar{1}1]$, $(2\bar{1}1)[111]$,	3
Point $[111]$	$(112)[11\bar{1}]$, $(121)[1\bar{1}1]$, $(211)[111]$.	3
Point $[100]$	$(2\bar{1}1)[111]$, $(211)[11\bar{1}]$, $(211)[11\bar{1}]$, $(211)[111]$.	4
Point Y	$(2\bar{1}1)[111]$, $(2\bar{1}1)[11\bar{1}]$, $(112)[11\bar{1}]$, $(112)[111]$.	4

There is a similar expression, Q , for the resolved shear stress on the other system, and the boundary is given by $P=Q$, *i.e.* the equation

$$\begin{aligned} & h^2(Rp_1p_2 - p_3p_4) + k^2(Rq_1q_2 - q_3q_4) + l^2(Rr_1r_2 - r_3r_4) \\ & + hk(Rp_1q_2 + Rp_2q_1 - p_3q_4 - p_4q_3) \\ & + hl(Rp_1r_2 + Rp_2r_1 - p_3r_4 - p_4r_3) \\ & + kl(Rq_1r_2 + Rq_2r_1 - q_3r_4 - q_4r_3) = 0, \quad \dots \dots \dots \quad (2) \end{aligned}$$

where

$$R = \frac{\left((p_3^2 + q_3^2 + r_3^2)(p_4^2 + q_4^2 + r_4^2) \right)^{\frac{1}{2}}}{\left((p_1^2 + q_1^2 + r_1^2)(p_2^2 + q_2^2 + r_2^2) \right)^{\frac{1}{2}}}.$$

This equation is homogeneous in the second degree and therefore is the equation of a cone. In the special case where the determinant

$$A = \begin{vmatrix} (Rp_1p_2 - p_3p_4) & \frac{1}{2}(Rp_1q_2 + Rp_2q_1) & \frac{1}{2}(Rp_1r_2 + Rp_2r_1) \\ & -p_3q_4 - p_4q_3 & -p_3r_4 - p_4r_3 \\ \frac{1}{2}(Rp_1q_2 + Rp_2q_1) & (Rq_1q_2 - q_3q_4) & \frac{1}{2}(Rq_1r_2 + Rq_2r_1) \\ -p_3q_4 - p_4q_3 & & -q_3r_4 - q_4r_3 \\ \frac{1}{2}(Rp_1r_2 + Rp_2r_1) & \frac{1}{2}(Rq_1r_2 + Rq_2r_1) & (Rr_1r_2 - r_3r_4) \\ -p_3r_4 - p_4r_3 & -q_3r_4 - q_4r_3 & \end{vmatrix} \quad \dots \dots \quad (3)$$

vanishes the equation corresponds to a pair of planes.

There is a further boundary corresponding to the equation

$$P = -Q, \quad \dots \dots \dots \quad (4)$$

which is also homogeneous in the second degree. The physical significance of this second boundary is that here the resolved shear stresses on the two systems are numerically equal but of opposite sign. The full expansion of (4) and its determinant differ from (2) and (3) only in that product terms with suffixes 3 and 4 are reversed in sign. The intersections of the cones, or pairs of planes, with the edges [100][111], [100][110], and [110][111] of the reference unit triangle may be determined by substituting $l=k$, $l=0$, and $h=k$ respectively in (2) and (4). In the case of pairs of planes these intersections are sufficient to define the planes and hence the boundaries in the triangle. The form of the boundaries within the unit triangle in the case of the cones may be determined by numerical solution in this region, and confirmed by the resolved shear stress tables.

Applying these general results to the determination of the boundary YZ in the $\{112\}\langle 111 \rangle$ system, equation (2) takes the form

$$h^2 - hk - 2k^2 - 3lk + l^2 = 0, \quad \dots \dots \dots \quad (5)$$

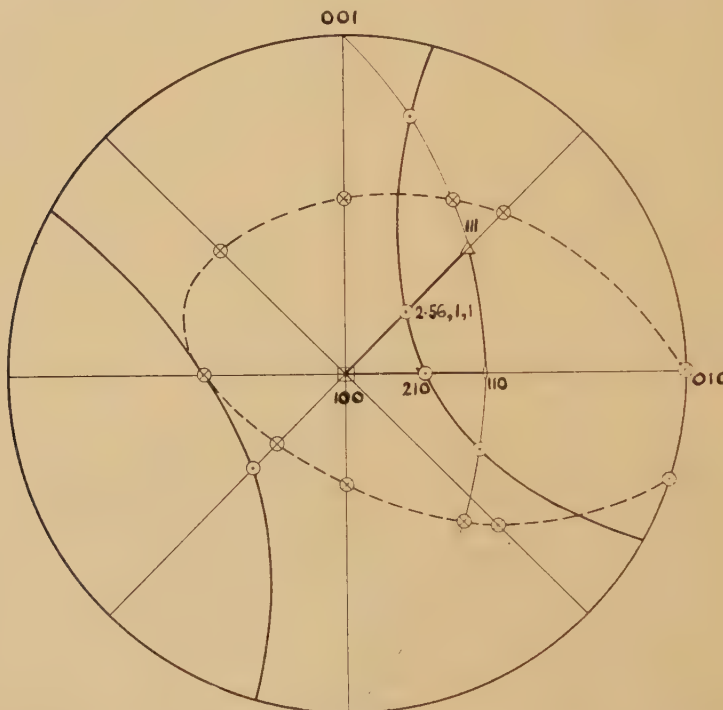
which, since the determinant (3) does not vanish, represents a cone. The solutions of (5) for the conditions $l=k$, $l=0$, and $h=k$ are respectively, $h=2.56k$ or $h=-1.56k$, $h=2k$ or $h=-k$, and $h=-1.78l$ or $h=0.28l$. A similar procedure for equation (4) shows that this boundary cone intersects $l=k$ at $h=0.59k$ and $h=-2.26k$, $l=0$ at $h=0$ and $h=-k$, and $h=k$ at $h=0.63l$ and $h=-0.80l$. These points of intersection are shown on

a standard stereographic projection in fig. 3. Thus the point Y is [210] and Z is [2·56, 1, 1]. Fig. 2 has been drawn to be consistent with this information.

$\{123\}\langle 111 \rangle$ System.

The $\{123\}\langle 111 \rangle$ system is more complex than either of those already discussed, since it involves three different most favourable slip systems within the unit triangle. The maximum resolved shear stress contours are shown in fig. 4 and the most favourable systems are listed in Table IV.

Fig. 3.



Standard stereographic projection showing the traces of the boundary cones corresponding to equation (2) for the systems $(2\bar{1}1)[111]$ and $(112)[11\bar{1}]$ equal in magnitude and sign (full line), and equation (4) for these systems equal in magnitude and opposite in sign (broken line).

It is interesting to note that the corner points have the same number of equivalent systems as the $\{110\}\langle 111 \rangle$ case, and in addition there are six equivalent systems at X and four at Y.

Consider now the boundary XY between the systems $(3\bar{1}2)[11\bar{1}]$ and $(213)[11\bar{1}]$. Equation (2) reduces to a pair of planes

$$h+k-l=0, \quad \dots \dots \dots \dots \quad (6a)$$

$$h-2k-l=0, \quad \dots \dots \dots \dots \quad (6b)$$

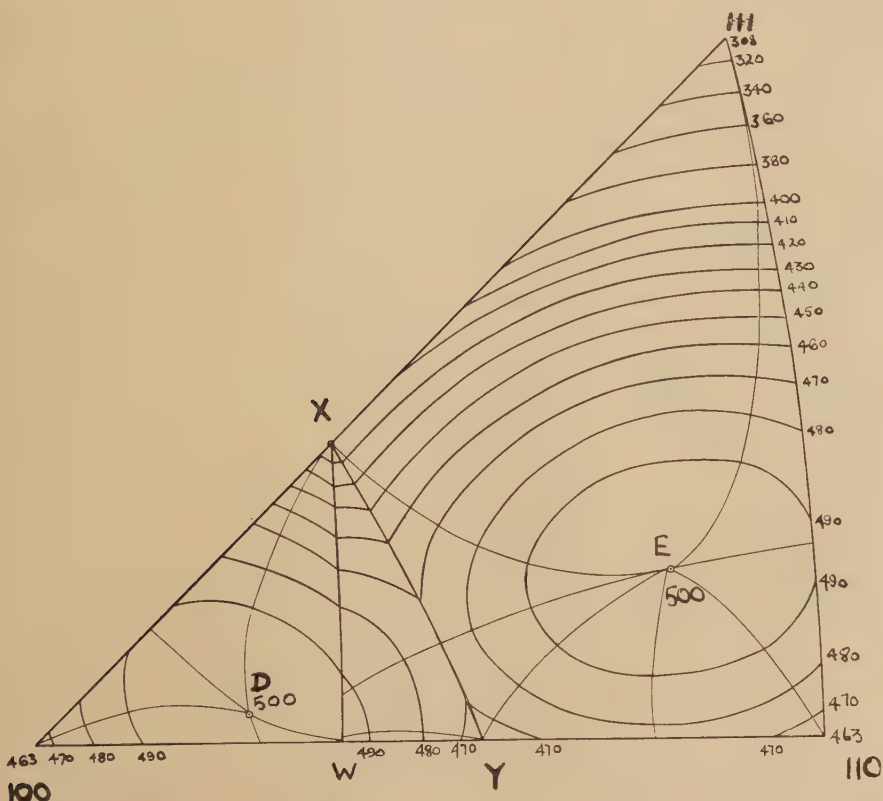
while equation (4) also reduces to two planes

$$h+k-l=0, \quad \dots \dots \dots \quad (7a)$$

$$h+l=0, \quad \dots \dots \dots \quad (7b)$$

It will be seen that the two cones degenerate into *three* distinct planes. Moreover, this degeneracy will always occur when the two slip systems under consideration have a common pole. The only plane which intersects the edges of the unit triangle is (6b), from which it may be deduced

Fig. 4.



Maximum resolved shear stress contours for the system $\{123\}\langle 111 \rangle$, showing some lines of quickest descent from maxima at D and E.

that X is [311] and Y is [210], and further that the boundary is the great circle from [101] through these points to [111]. For the other pair of slip systems, $(3\bar{1}2)[111]$ and $(3\bar{1}2)[1\bar{1}1]$, (2) and (4) become respectively

$$3kl-hl=0, \quad \dots \dots \dots \quad (8)$$

and $3h^2+2hk-k^2-2l^2=0. \quad \dots \dots \dots \quad (9)$

The cone (9) does not intersect the reference triangle edges and may be neglected. (8) obviously represents a pair of planes $l=0$ and $h=3k$, the traces of which are [100]Y and XW, where X is [311], Y is [210], and W is [310]. These boundaries are the parts of great circles.

Three Active Systems.

(a) *Equal Critical Shear Stresses.* The simplest case to consider when the systems $\{110\}\langle 111 \rangle$, $\{112\}\langle 111 \rangle$, and $\{123\}\langle 111 \rangle$ are all possible slip systems is when the critical resolved shear stresses for the activation of these systems are equal. An indication of the most favourable systems may be obtained by the superposition of the shear stress contour diagrams for the individual systems, figs. 1, 2, and 4. The exact positions of the boundaries between the systems may be found by the method of the preceding sections. As may be expected, the system of boundaries within the unit triangle is relatively complicated (fig. 9).

TABLE IV.

Most Favourable $\{123\}\langle 111 \rangle$ Slip Systems

	Slip systems	Number
Area $[100]WX$	$(3\bar{1}2)[111]$.	1
Area WXY	$(3\bar{1}2)[11\bar{1}]$.	1
Area $[110][111]XY$	$(213)[11\bar{1}]$.	1
Boundary $[100]Y$	$(312)[111]$, $(3\bar{1}2)[11\bar{1}]$.	2
Boundary $Y[110]$	$(213)[11\bar{1}]$, $(213)[111]$.	2
Boundary $[110][111]$	$(213)[11\bar{1}]$, $(123)[11\bar{1}]$.	2
Boundary $[111]X$	$(213)[11\bar{1}]$, $(231)[111]$.	2
Boundary $X[100]$	$(3\bar{1}2)[111]$, $(32\bar{1})[111]$.	2
Boundary WX	$(312)[111]$, $(3\bar{1}2)[11\bar{1}]$.	2
Boundary XY	$(213)[11\bar{1}]$, $(312)[11\bar{1}]$.	2
Point Y	$(213)[11\bar{1}]$, $(213)[111]$, $(3\bar{1}2)[111]$, $(3\bar{1}2)[11\bar{1}]$.	4
Point $[110]$	$(213)[11\bar{1}]$, $(21\bar{3})[111]$, $(12\bar{3})[111]$, $(123)[11\bar{1}]$.	4
Point X	$(312)[111]$, $(32\bar{1})[111]$, $(213)[11\bar{1}]$, $(3\bar{1}2)[111]$, $(321)[111]$, $(231)[111]$.	6
Point $[111]$	$(213)[11\bar{1}]$, $(123)[11\bar{1}]$, $(312)[111]$, $(321)[111]$, $(132)[111]$, $(231)[111]$.	6
Point $[100]$	$(3\bar{1}2)[111]$, $(32\bar{1})[111]$, $(312)[11\bar{1}]$, $(3\bar{2}1)[11\bar{1}]$, $(312)[111]$, $(321)[11\bar{1}]$, $(31\bar{2})[111]$, $(32\bar{1})[111]$.	8

(b) *Unequal Critical Shear Stresses.* The preliminary results of Smoluchowski and Opinsky (1950) suggest that the critical shear stresses of the three systems are not equal. This case may be dealt with in the same straightforward manner with (2) and (4) modified to

$$P = \pm \frac{C_p}{C_q} Q, \quad \dots \quad \dots \quad \dots \quad \dots \quad (10)$$

where C_p and C_q are respectively the critical resolved shear stresses on the systems corresponding to the terms P and Q . The changes in the positions of the boundaries for the observed critical shear stress ratios may be seen by comparison of figs. 9 and 11.

§ 3. TENSION AND COMPRESSION TEXTURES.

Slip on {110}⟨111⟩ System.

Although the resolved shear stress contours are the same for the {110}⟨111⟩ system and for the {111}⟨110⟩ system discussed in Part I., the textures developed under tension and compression are interchanged. This is because under tension the stress direction tends to move towards the operative slip direction, the ⟨111⟩ in the {110}⟨111⟩ case, and the ⟨110⟩ in the {111}⟨110⟩ case, while under compression the stress direction moves towards the pole of the operative slip plane, the ⟨110⟩ and the ⟨111⟩ respectively. The directions of the rotations corresponding to single and duplex slip on the {110}⟨111⟩ system in various parts of the unit triangle may be derived from a consideration of the operative slip systems listed in Table II. These are shown diagrammatically in figs. 3 and 6 of Part I. which now refer to *compression* and *tension* respectively. From these components, bearing in mind the relative probability of single and duplex slip, the general trends of rotation throughout the unit triangle are obtained. For example, at a point t (fig. 1) it will be seen from the contours that the path of the effective stress, T_e , is first for a short distance to an adjacent point on the [100][111] boundary and thence for a much greater distance along the boundary to [111]. Thus it is reasonable to suppose that, in general, slip will occur more frequently when T_e is situated on the boundary than when it is between the point t and the boundary: that is to say, duplex rotation is the more probable. For a point u in the area [100]AK near to A it will be deduced from similar considerations that single crystal rotation occurs more frequently. This leads to a *tension* texture as shown in fig. 8, Part I., and a *compression* texture as shown in fig. 5, Part I. Although minor components are predicted in these textures as a result of the sluggishness of rotations in the neighbourhood of the points of multiple slip, such components may well be absent after extremely severe deformation.

The tension texture is principally a [110] texture with a spread between [311] and [110], which decreases with increasing deformation. There are no experimental data available for textures resulting from pure tension and discussion of this texture will be deferred.

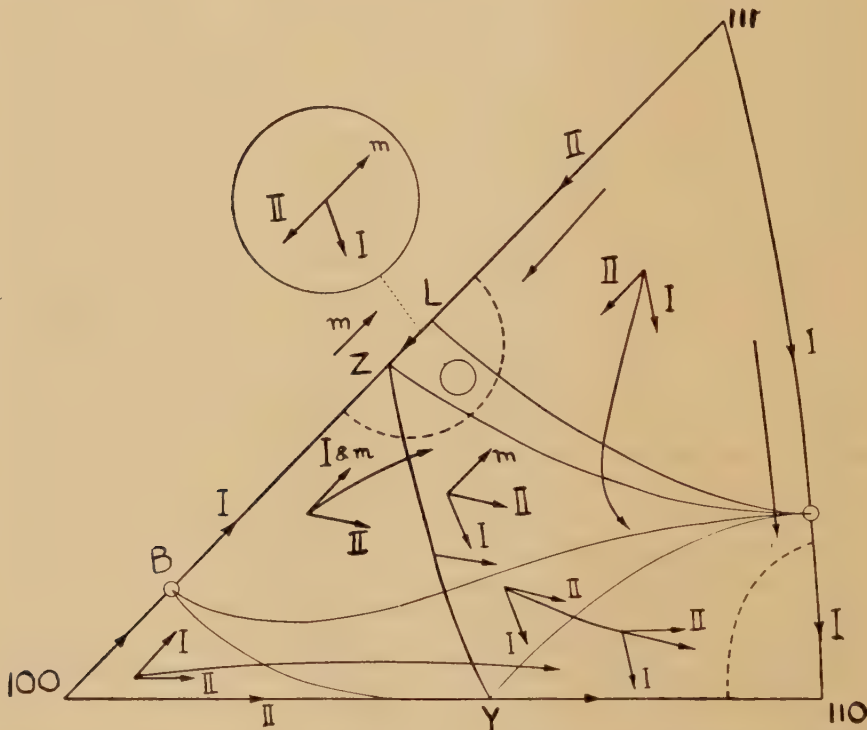
The compression texture is [111], [211] and [100], the last being the weakest component. Again it is probable that the [100] and [111] components decrease in importance with increasing deformation.

Slip on the {112}⟨111⟩ System.

The single, duplex and multiple slip systems operative for the {112}⟨111⟩ system are listed in Table III., and with the aid of these the general trend of crystal rotations in a specimen under tension may be derived (fig. 5). It is clear from this diagram that the texture will be mainly [110]. An interesting situation arises, however, in the region near to the minimum point, Z, in the resolved shear stress diagram. When the effective stress, T_e , reaches Z slip occurs on three equivalent systems which are

not symmetrically disposed, resulting in rotation in the direction $Z \rightarrow [111]$. The part of this region lying in the triangle LCZ shows a complex behaviour, since the multiple and duplex rotations are in opposite directions quite distinct from the single crystal direction. Considering a single grain, or part of a grain, undergoing deformation, at some stages of the process it may suffer rotations corresponding to multiple slip and at other stages the reverse rotations corresponding to duplex slip. This clearly leads to a subsidiary texture which may persist until a very late stage in the deformation. Superimposed on these conflicting rotations

Fig. 5.

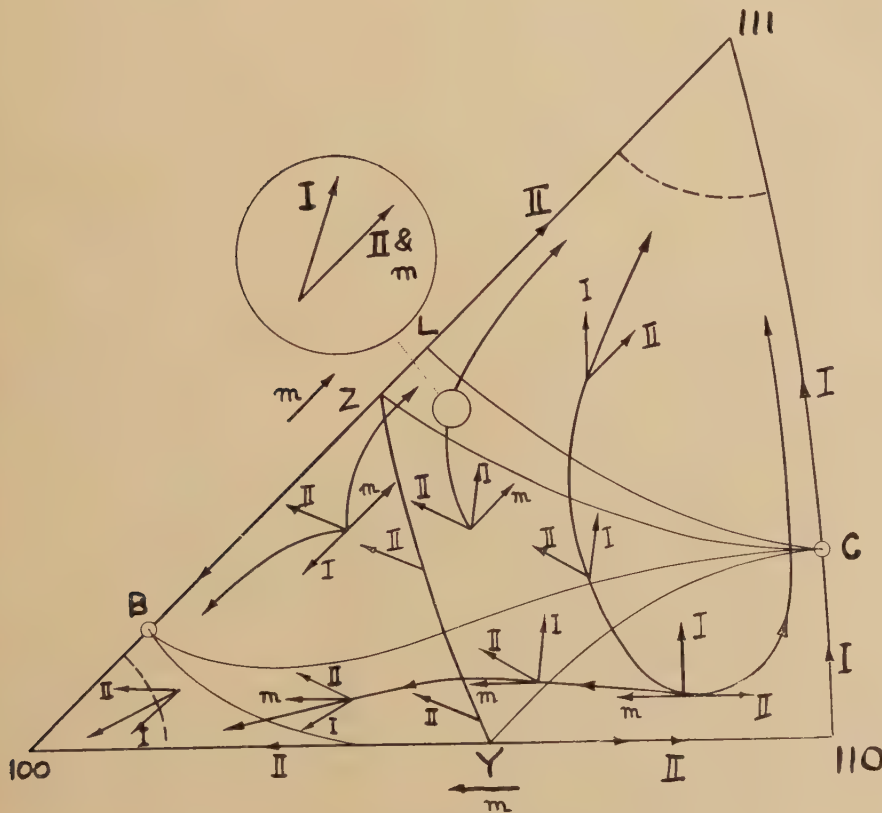


{112}⟨111⟩ system. Tension rotations and texture. Regions of preferred orientation bounded by broken line. I, direction of single crystal rotation; II, direction of duplex rotation; m , direction of rotation due to multiple slip on unsymmetrically disposed systems.

there is a general drift towards $[11\bar{1}]$, the operative single crystal slip direction, which augments the $[110]$ texture at the expense of this subsidiary texture. The point Y is also a minimum of resolved shear stress and a point at which multiple but unsymmetrically disposed slip occurs. Here, however, the multiple and duplex slip directions are the same, and the general trend of rotations towards the $[110]$ as deduced from the duplex rotations is unaltered. The deformation texture is not modified therefore by the presence of this point of multiple slip.

The behaviour under compression is illustrated in fig. 6, and it may be seen that there is a double [111], [100] texture. In the main, orientations within the area [111][110]YZ rotate towards [111] while those in the area [110]YZ move towards [100], so that the former texture predominates. The unsymmetrically disposed multiple slip systems at Y and Z modify this to a small extent, but do not give rise to subsidiary textures as in the case of tension. This is because, under compression, in the regions where the multiple and duplex rotations are opposed,

Fig. 6.



{112}{111} system. Compression rotations and texture.

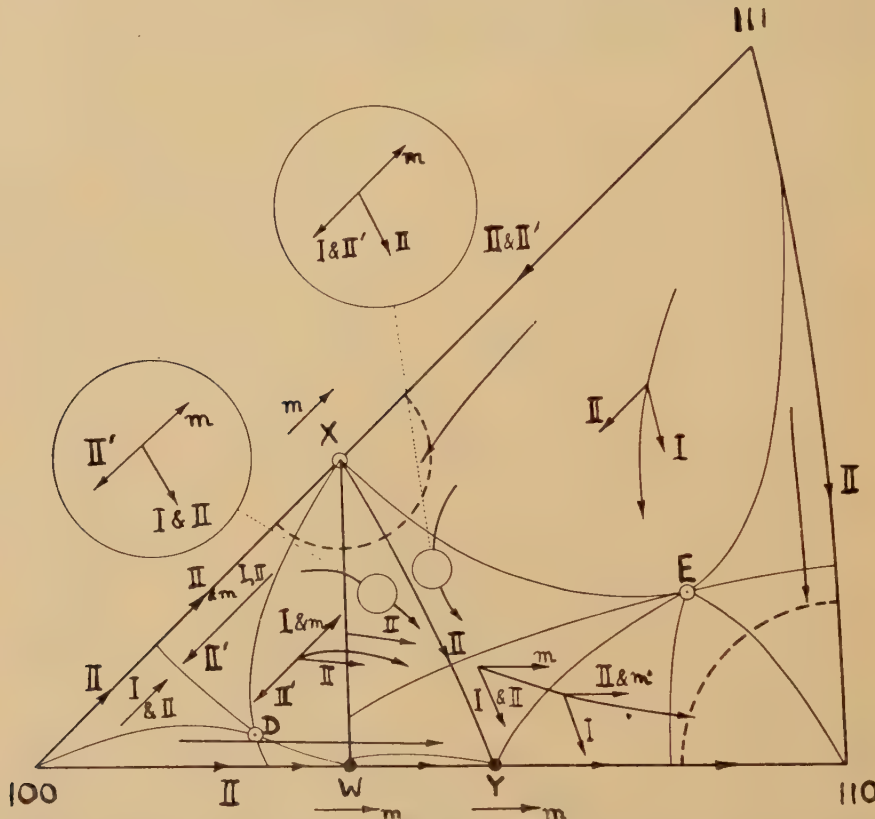
operation of a given rotation leads to a new orientation which favours further rotation of the same kind, whereas under tension operation of a given type of rotation leads to a new orientation which favours rotation in the reverse direction.

Slip on the {123}{111} System.

From an examination of fig. 7 showing the grain rotations to be expected when slip takes place on the {123}{111} system under tension it is evident that the principal texture is [110]. The rotations near to X, [311],

are complicated by the multiple slip at X, and they give rise to a subsidiary [311] texture which may be expected to persist until a late stage in the deformation process. The compression case is illustrated in fig. 8. Here there is a double [111], [100] texture, with [111] as the main component, and a subsidiary transitional texture around [311].

Fig. 7.



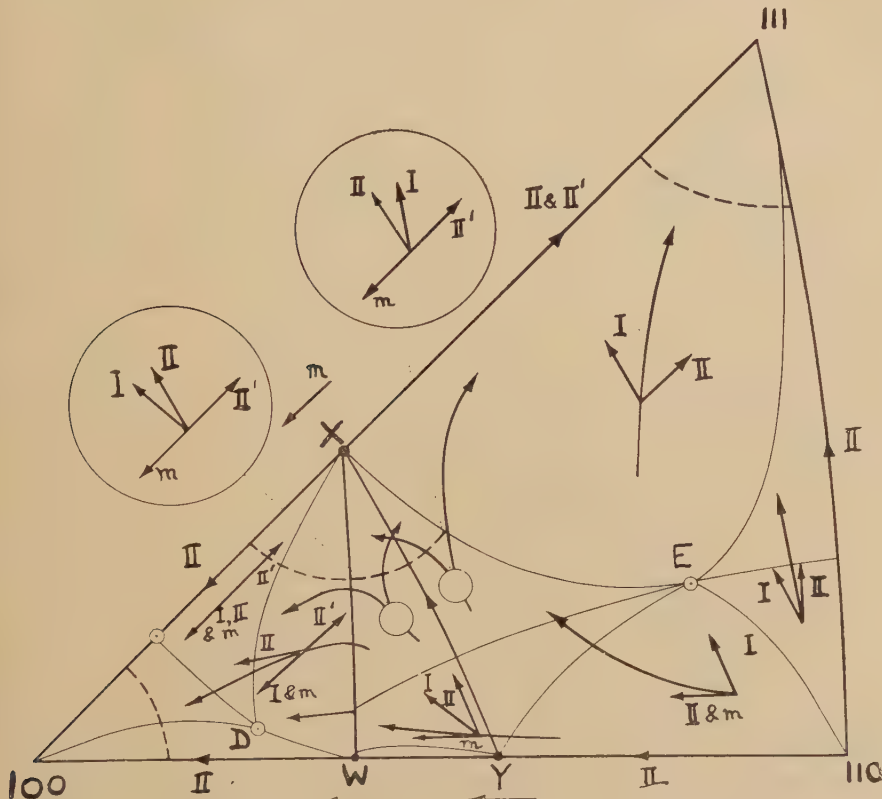
{123}⟨111⟩ system. Tension rotations and texture. I, II, and m have the same significance as in previous figures. II' indicates a further possible duplex rotation.

Slip on Three Systems.

(a) *Equal Critical Shear Stresses.* The rotations leading to the development of the principal tension texture, [110], and the subsidiary texture around [411] are shown in fig. 9. The subsidiary texture is due to the opposing influence of multiple and duplex rotations in this region. Since unsymmetrical multiple slip occurs at both the points U and V the subsidiary texture is rather more extensive than in previous cases. The compression texture is shown in fig. 10, with [111] as the main component, [100] as a minor component, and [411] as a transitional subsidiary component.

(b) *Unequal Critical Shear Stresses.* Comparison of figs. 9 and 11 shows that the differences in rotations and the textures developed are relatively small despite the considerable changes in magnitude of the areas over which the individual slip systems operate: It appears that both the tension subsidiary texture and the compression [100] minor component are slightly reduced.

Fig. 8.



{123}{111} system. Compression rotations and texture.

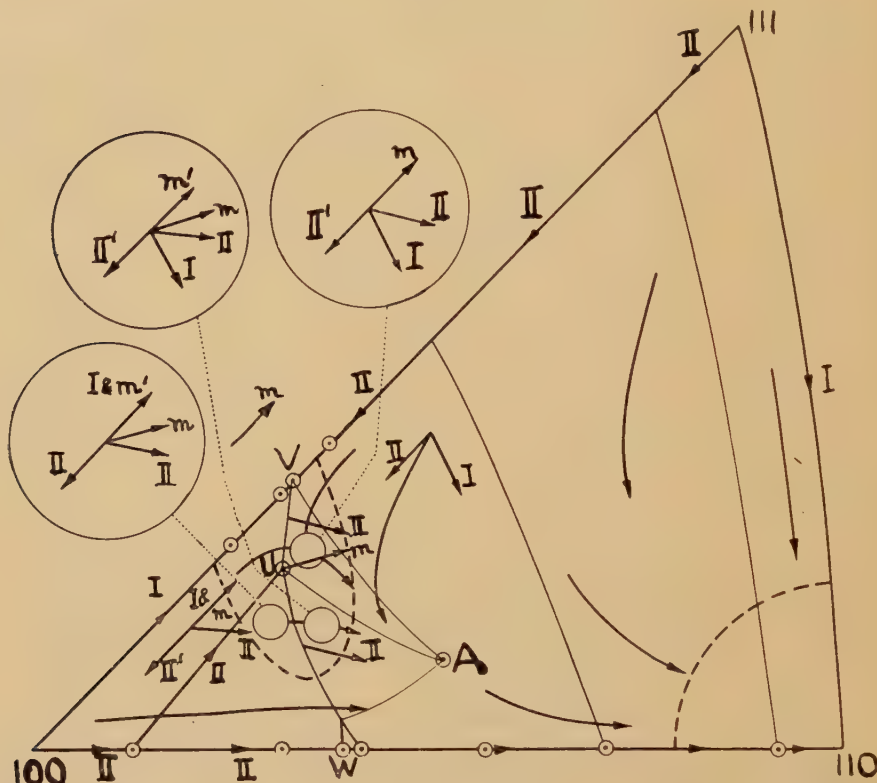
§ 4. ROLLING AND DRAWING TEXTURES.

The rolling and drawing textures resulting from slip on any one or combination of the systems discussed may be derived in the manner described briefly in Part I. For example, with slip on three systems giving compression textures [111], [100], and [411], and tension textures [110] and [411], the [111] and [110] compression end points and the [110] tension end point may be simultaneously satisfied. The [411] transitional texture in compression satisfies both the tension end point [110] and, to a close approximation, the tension transitional texture at [411] as well as any spread from this point towards the [110]. It is therefore reasonable

to suppose that, although the [411] components are transitional both in tension and compression, they persist in the rolling texture which therefore includes, in order of decreasing magnitude, (411)[110 \leftarrow 411], (111)[110], and (100)[110].

The rolling textures to be expected from slip on the various systems are listed in Table V.

Fig. 9.



Three systems ; equal critical shear stresses. Tension rotations and textures.

I, II, II' and m have the same significance as in previous figures. m' is a further possible direction of rotation due to multiple slip on unsymmetrically disposed systems.

TABLE V.
Rolling Textures.

System	Textures in order of decreasing magnitude
{110}⟨111⟩	(211)[110 \leftarrow 311], (111)[110], (100)[110].
{112}⟨111⟩	(111)[110 \leftarrow 211], (100)[110].
{123}⟨111⟩	(311)[110 \leftarrow 311], (111)[110], (100)[110].
Three systems	(411)[110 \leftarrow 411*], (111)[110], (100)[110].

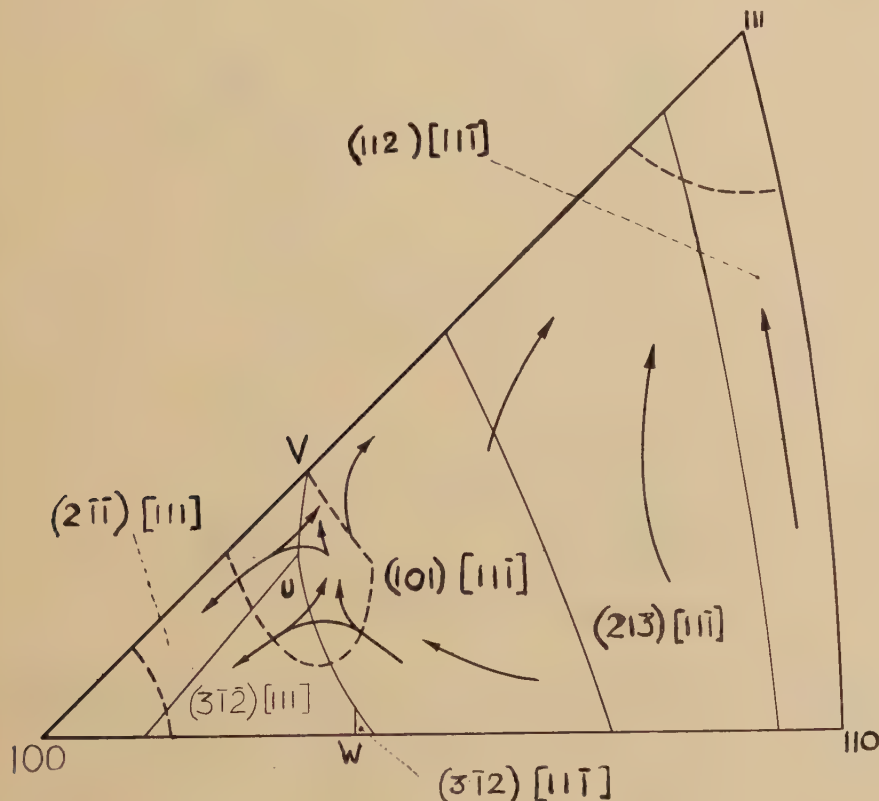
* (411)[411] is not strictly a texture but (411)[511] is and the angular difference between the two is a matter of only about 3°.

The methods of Part I. may also be applied to wire drawing textures. These lead in all cases, after severe deformation, to a simple [110] fibre texture.

§ 5. DISCUSSION.

The most striking feature of the tension and compression textures derived above is their similarity for all the slip systems considered ; it is only in the transitional components that they differ.

Fig. 10.



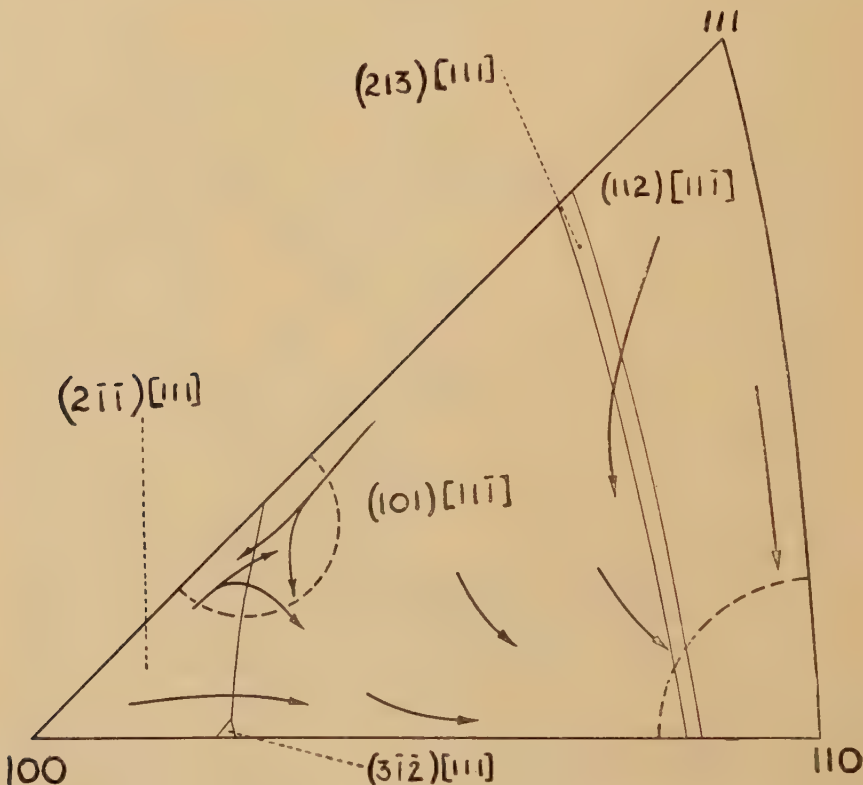
Three systems ; equal critical shear stresses. Compression texture and operative slip systems.

As for the face-centred cubic metals there are no data on pure tension textures. For compression, the experimental observations by Heger (1941) on an iron alloy containing 4.6 per cent silicon, which deforms on $\{110\}\langle111\rangle$, showed a double fibre texture with [111] and [100] parallel to the axis of compression. The only other compression data available are for α -iron, where all three systems are active. Here again a double [111], [100] fibre texture was found with the [100] component the weaker (Barrett 1939). This double texture, with [100] the weaker, is predicted by the present treatment in all cases. It is expected, however, that

with only the $\{110\}\langle111\rangle$ system operative a [211] texture develops at the expense of the double texture after severe deformation. This has not yet been confirmed by experiment.

In view of its industrial importance there is a considerable amount of experimental information on rolling textures in iron and steel, and a large measure of agreement from observer to observer. The most careful studies would appear to be those carried out in the Carnegie Institute of

Fig. 11.

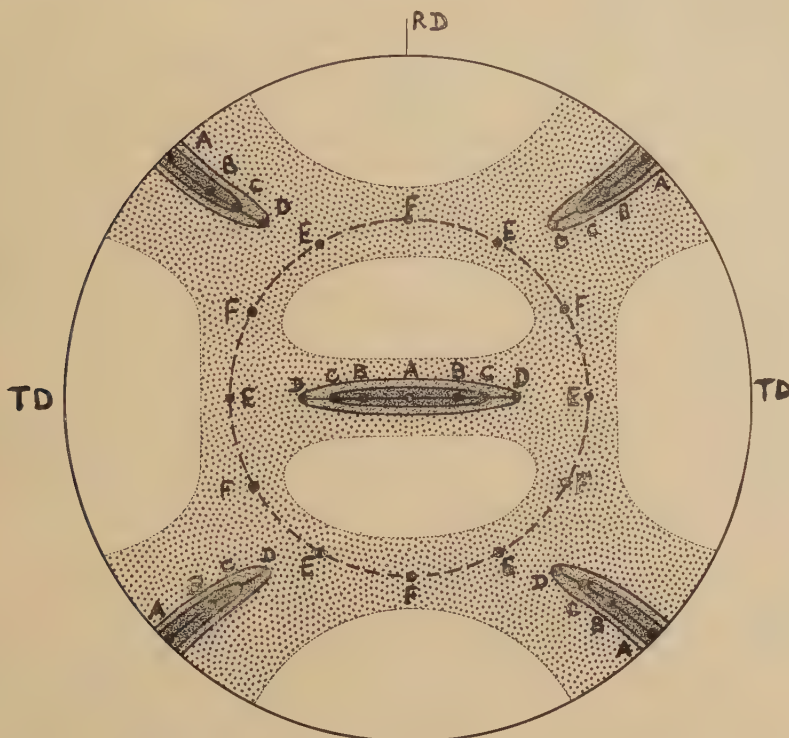


Three systems ; unequal critical shear stresses. Tension texture and operative slip systems.

Technology (Gensamer and Mehl 1936; Barrett, Ansel and Mehl 1937 b; Barrett and Levenson 1941). They have examined the textures of rolled silicon iron alloy which deforms on $\{110\}\langle111\rangle$, and α -iron which deforms on the three systems. A typical (100) pole figure is reproduced in fig. 12. They concluded that there are two continuous sets of end points : (1) a set including the textures $(100)[110]$, $(511)[110]$, $(311)[110]$, and $(211)[110]$ indicated by the points A, B, C and D respectively, which have the $[110]$ direction parallel to the rolling direction and the (100) plane at any angle up to 45° or 55° from the rolling plane ; and (2) a set of orientations including the textures $(111)[110]$, E, and $(111)[211]$, F, which have the (111) plane in the plane of the sheet and all possible positions of the rolling

direction in this plane. It was further found that, with $\{110\}\langle111\rangle$ slip or slip on all three systems, the only difference in the pole figures was that in the former case the scatter of (100) planes about the rolling axis was 55° to 60° compared with 40° to 45° for the three systems. It is obvious that no one of the predicted textures listed in Table V. can account for these continuous ranges of orientation.

Fig. 12.



(100) pole figure for rolled iron showing various ideal orientations : A, $(100)[110]$; B, $(511)[110]$; C, $(311)[110]$; D, $(211)[110]$; E, $(111)[110]$; F, $(111)[211]$. Heavy full lines represent a continuous set containing A to D. Circle in broken line is a second continuous set containing E and F. (Barrett and Levenson.)

The introduction of a further simple assumption not only overcomes this difficulty but also explains the characteristically wavy slip lines in α -iron. It is that the ratio of critical shear stresses for the three slip systems varies from one part of a grain to another such that the polycrystalline aggregate may be considered as composed of units, some deforming on each one of the three systems and some on all three systems. From the considerable movement of the boundaries in figs. 9 and 11 it is evident that the variations of the ratios of critical shear stress from one region to another in a grain need not be large. The rolling texture of iron will thus include all those orientations listed in Table V., that is, those orientations illustrated by Barrett and Levenson (1941), with the trifling exception

that $(411)[110]$ replaces $(511)[110]$. Moreover, the major textures of Table V. give the stronger set of components A to D, referred to in the preceding paragraph, with the exception of $(100)[110]$ which is predicted as a weaker texture. This is probably a small point as the spread from the $(411)[110]$ on either side of the centre of the pole figure may well maintain this orientation. On the other hand it may be pointed out that Kurdjumow and Sachs (1930) did indeed find a saddle at the centre of their (100) pole figure.

The careful experimental work of Gough (1928) showed that at low deformations the wavy slip bands in single crystals of iron can be resolved into short separate traces of slip planes of the now accepted forms. This he interpreted as duplex slip on the two planes nearest to the plane of highest resolved shear stress, but he was unable to explain why the deformation takes place by small elements of slip alternating from one plane to another rather than the production of two interlacing sets of straight slip bands. On the present assumption, however, the small segments of a wavy slip band correspond to parts of the crystal in which the different ratios of critical resolved shear stress produce different most favourable systems.

The compression and tension textures predicted here now need reconsideration when applied to α -iron. The main textures are unaltered, but there are additional transitional subsidiary textures corresponding to slip on each of the three individual systems, *i.e.* main tension texture $[110]$ with subsidiary textures $[211]$, $[311]$ and $[411]$, and main compression textures $[111]$, $[100]$ and subsidiary textures $[211]$, $[311]$, and $[411]$. These subsidiary textures are likely to coalesce into a general spread of orientation between $[100]$ and $[111]$.

The objection may be raised that in an iron alloy containing 4.6 per cent silicon the slip lines are usually very much straighter than in α -iron. Consequently this material must deform on a single system shown to be the $\{110\}\langle 111 \rangle$, and so could not attain the full rolling texture observed. However, Barrett, Ansel and Mehl (1937) have suggested that after severe deformation the same slip mechanism may operate in this alloy as in α -iron, which presumably implies that the effect of the silicon in solid solution in raising the critical shear stresses on the $\{112\}\langle 111 \rangle$ and the $\{123\}\langle 111 \rangle$ systems, although appreciable in the early stages, may be comparatively small after severe work-hardening with these as latent systems. The straight slip lines, of course, relate to observations on material after deformation slight in comparison with the rolling reductions under consideration. Furthermore, the predominance of the $\{110\}\langle 111 \rangle$ system may be expected to increase the component corresponding to this system in the final texture, the $(211)[110 \leftarrow 311]$ causing a greater spread of orientation along the equator of the (100) pole figure which has been confirmed experimentally. Thus it appears that the $\{110\}\langle 111 \rangle$ system plays a greater part in the deformation of this alloy especially in the earlier stages, and even in the later stages of deformation when the other systems are active in producing the full rolling texture.

Finally, it may be remarked that the predicted simple [110] fibre texture in cold-drawn wires is amply confirmed by experiments on all body-centred cubic metals so far examined.

§ 6. CONCLUSIONS.

The qualitative treatment of the development of deformation textures in face-centred cubic metals described in Part I. has been extended to those of body-centred cubic structure. The main features of tension, compression, rolling and drawing textures have been satisfactorily predicted. The detailed examination of the rolling textures of iron alloys presents some difficulty and necessitates the introduction of the further assumption that in adjacent regions within a single metallic grain there are differences in the ratios of the critical shear stresses. This is justified in that it leads to the explanation of wavy slip lines in α -iron, a well established fact, and permits the prediction not only of the complete rolling textures of iron alloys but also some of the minor variations among them.

It seems likely that the general concepts of this theory may be applicable to other aspects of the deformation of both single crystals and polycrystalline aggregates. For example, there appears to be a close connection between the alternative directions of rotation discussed here and the development of deformation bands.

Further accurate experimental work on deformation textures is necessary before the details of the theoretical predictions may be fully tested.

ACKNOWLEDGMENTS.

The authors acknowledge the considerable assistance given by members of the staff of Mathematics Division of the National Physical Laboratory who calculated the Resolved Shear Stress Tables.

The work described above has been carried out as part of the research programme of the National Physical Laboratory, and this paper is published by permission of the Director of the Laboratory.

REFERENCES.

- ANDRADE, E. N. DA C., 1940, *Proc. Phys. Soc.*, **52**, 1.
- BARRETT, C. S., ANSEL, G., and MEHL, R. F., 1937 a, *Trans. A.S.M.*, **25**, 702 ;
1937 b, *Trans. A.I.M.E.*, **125**, 516.
- BARRETT, C. S., 1939, *Trans. A.I.M.E.*, **135**, 296.
- BARRETT, C. S., and LEVENSON, L. H., 1941, *Trans. A.I.M.E.*, **145**, 281.
- CALNAN, E. A., and CLEWS, C. J. B., 1950, *Phil. Mag.*, **41**, 1085.
- FAHRENHORST, W., and SCHMID, E., 1932, *Z. Physik*, **78**, 383.
- GENSAMER, M., and MEHL, R. F., 1936, *Trans. A.I.M.E.*, **120**, 277.
- GOUGH, H., 1928, *Proc. Roy. Soc. A*, **118**, 498.
- HEGER, J. J., 1941, Unpublished Senior Thesis, Carnegie Inst. of Tech. ; cited by
Barrett, C. S., 1943, *Structure of Metals* (New York : McGraw-Hill),
p. 387-388.
- KURDJUMOW, G., and SACHS, G., 1930, *Z. Physik*, **62**, 592.
- MISES, R. v., 1928, *Z. angew. Math. Mech.*, **8**, 161.
- SMOLUCHOWSKI, R., and OPINSKY, A. J., 1950, *Carnegie Inst. of Tech. Conference
on Plastic Deformation of Crystalline Solids* (in press).
- TAYLOR, G. I., 1938, *J. Inst. Metals*, **62**, 307.

LXVI. *Highly Forbidden Transitions in the Decay of Na²⁴.*

By J. F. TURNER and P. E. CAVANAGH *.
Atomic Energy Research Establishment, Harwell.

[Received March 29, 1951.]

ABSTRACT.

A description is given of the use of an organic scintillation counter in conjunction with a thin lens β -spectrometer to detect low intensity, high energy electron groups in the presence of a high background. Evidence for a 4.17 MeV. β -group in the radiations from Na²⁴ has been found, and a value of branching-ratio obtained. Measurements made on the secondary electron spectrum from Na²⁴ show the presence of a high energy γ -ray, possibly from the cross-over γ -transition in Mg²⁴.

§ 1. INTRODUCTION.

THE angular correlation measurements of Brady and Deutsch (1950) suggest that the spins to be associated with the 4.14 MeV., 1.38 MeV., and ground states of Mg²⁴ are 4, 2, 0, respectively, and that both the 2.76 and 1.38 MeV. γ -rays correspond to quadrupole transitions. This assignment, in the case of the 2.76 MeV. γ -ray, is in disagreement with the results of Rae (1949) who, from a measurement of the internal pair production coefficient, deduced that this was a dipole transition. Later measurements by Mims, Halban and Wilson (1950) on annihilation quanta arising from internally produced pairs gave results which were more compatible with a quadrupole transition. Another line of attack on this problem is the investigation of the cross-over γ -transition by Bishop, Wilson and Halban (1950), who measured the energy spectrum of photo-protons in a deuterium filled ionization chamber counter. The crossover γ -ray was not observed, and an upper limit of 3×10^{-7} has been placed on its occurrence. A further investigation is that of Grant (1950) who attempted to measure higher energy β -rays corresponding to highly forbidden transitions to the ground and intermediate states using a thin lens spectrometer, with a coincidence counter pair for recording the focused β -particles. No high energy β -particles were observed and the upper limit placed on the intensity of the 4.14 MeV. β -transition was 1 in 10^4 .

§ 2. THE TECHNIQUE USED.

The present work was pursued independently of that of Grant whose results only came to hand when the investigation was completed. Essentially, it was the same type of investigation as Grant's except that an organic crystal scintillator was used to record the focused β -particles. We

* Communicated by the Authors.

have already given a very brief description of the technique (1950). The spectrum of pulses resulting from the irradiation of the crystal by the almost monokinetic electrons focused by the spectrometer is in the form of a symmetrical peak, with half width determined by the energy of the electrons and the crystal-photo-multiplier combination. In general this will be superimposed on a background due to cosmic radiation, and direct and scattered γ -radiation. Scattered quanta and electrons will cause an increase in the pulse height distribution at small amplitudes. The pulse amplitude corresponding to the peak and the focused momentum will be related in the same way as energy and momentum of an electron. The use of the technique does enable one to pick out those pulses corresponding to electrons of the focused momentum from, in some instances, the much larger number of pulses arising from other causes, but recorded at the same value of coil current.

§ 3. THE EXPERIMENTAL ARRANGEMENT.

The thin lens spectrometer, adapted for ring focusing, gave a resolution of 5 per cent and transmission of 0·4 per cent when used with a 1 cm. diameter source. The sources were compressed blocks of sodium fluoride inside a thin aluminium covering, and with thicknesses ranging from 10 to 40 mg./cm.². The scintillator used was in the form of a clear block of naphthalene + 1 per cent anthracene 5 cm. in diameter and 3·8 cm. thick, grown by Mr. R. F. Jackson, Junior of A.E.R.E. and located outside the spectrometer behind a vacuum tight window of 7 mg./cm.² aluminium. The resolution obtained with this crystal was about 20 per cent for electrons of 1 MeV. The magnetic field due to the main coil was neutralized over the region of the photomultiplier by means of a set of coils carrying the main current, so that the gain was substantially independent of the focused energy. The response from the multiplier was amplified and analysed by means of a five channel Pulse Analyser Type 1074A.

§ 4. THE HIGH ENERGY β -SPECTRUM.

Fig. 1 shows the pulse distribution obtained at values of momentum above that of photoelectrons from the 2·76 MeV. γ -rays, and peaks due to the high energy β -group are clearly visible, superimposed on a background due largely to direct and narrow angle scattered γ -radiation. It was found that the pulse amplitude at the peak was directly proportional to the focused energy, as expected. Moreover a Fermi analysis of the results gave a straight line plot with an end point at 4·17 MeV. (fig. 2) in excellent agreement with the maximum energy of the β -transition to the intermediate state. Measurements extending over several half periods showed that the decay of the high energy β -transitions must be quite close to that of the main transition. An estimate of the relative intensities was made by comparing the slopes of the two Fermi distributions. This gave a value of 3×10^{-5} for the intensity of the 4·14 relative to the 1·38 MeV. β -rays, a result compatible with Grant's.

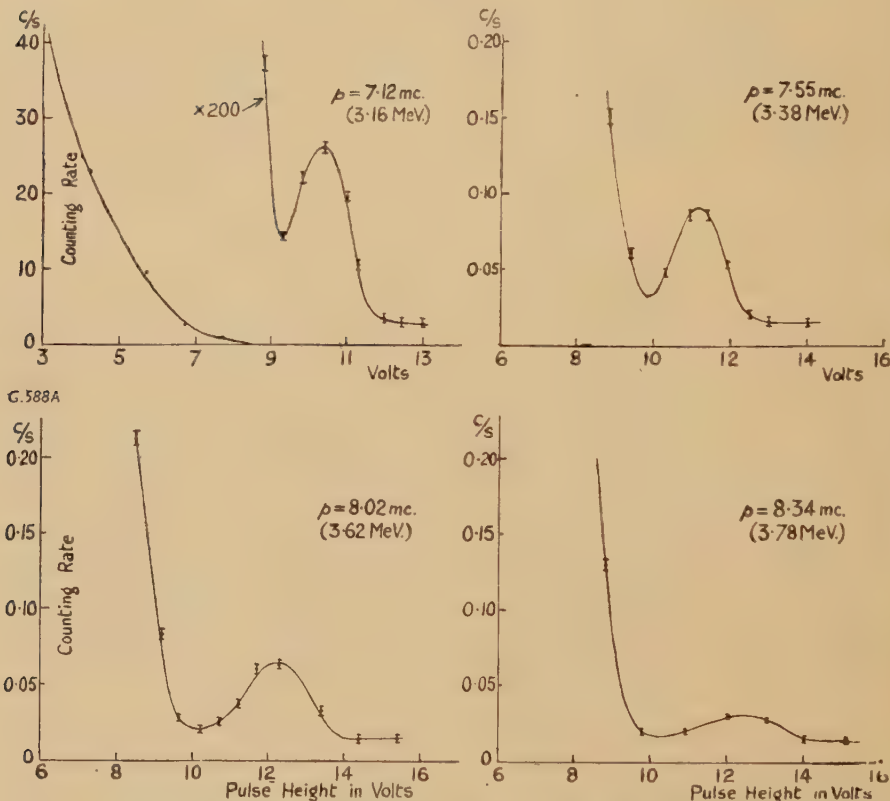
The region beyond the end-point of the 4.14 MeV. β -ray was carefully investigated but no trace of the 5.53 MeV. β -transition to the ground state was found. $f\tau$ values derived for the three transitions are

$$f\tau(1.38 \text{ MeV.}) = 1.22 \times 10^6,$$

$$f\tau(4.14 \text{ MeV.}) = 5.0 \times 10^{12},$$

$$f\tau(5.53 \text{ MeV.}) > 1.2 \times 10^{15}.$$

Fig. 1.



Variation of pulse analyser curves with focused momentum.

The last two may be small by a factor of about two arising out of the assumption of a straight line Fermi plot for the forbidden transitions. The energy of the intermediate transition is in agreement with the order of emission of the two γ -rays, as indicated by the results of inelastic scattering experiments by Beghian, Grace, Preston and Halban (1950) and by Rhoderick (1949).

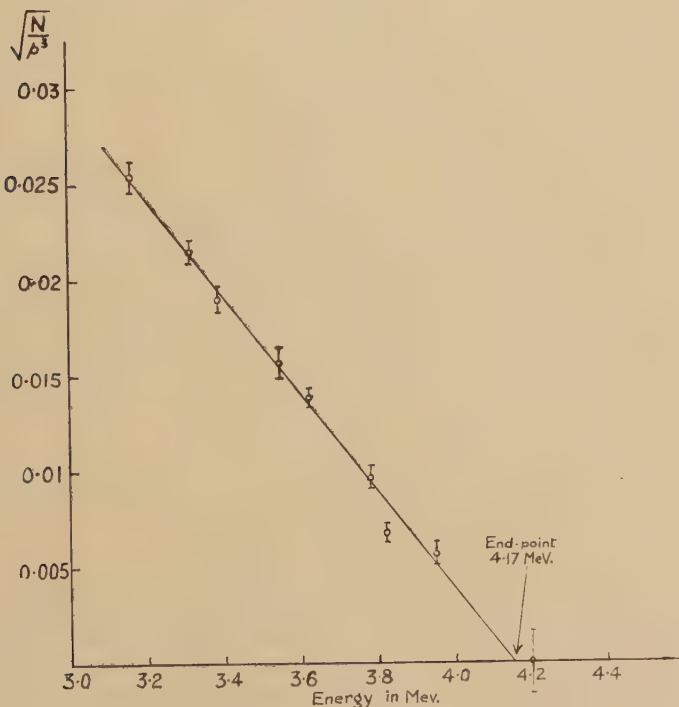
§ 5. THE HIGH ENERGY γ -RADIATION.

It was while performing a further check on the nature of the particles observed that it was noticed that the placing of a thick absorber over the source, so far from eliminating the peak in the pulse distribution due to

high energy β -particles, actually increased its height considerably. There can, we believe, be only one explanation to this phenomenon, and that is that the source emits high energy γ -rays. A later check, however, using as a reference the Compton electrons due to the 2.76 MeV. γ -ray ejected from the bare source, enabled us to show that in this latter case, at any value of the momentum, less than 10 per cent of the counting rate of high energy electrons could be ascribed to a high energy γ -ray, and that the great majority were in fact due to the high energy β -transition.

Measurements were continued with more intense sources, up to 10 mC., better resolution ~ 3.5 per cent and with saturation thicknesses of both lead and copper radiators. The shapes of the secondary electron spectra

Fig. 2.

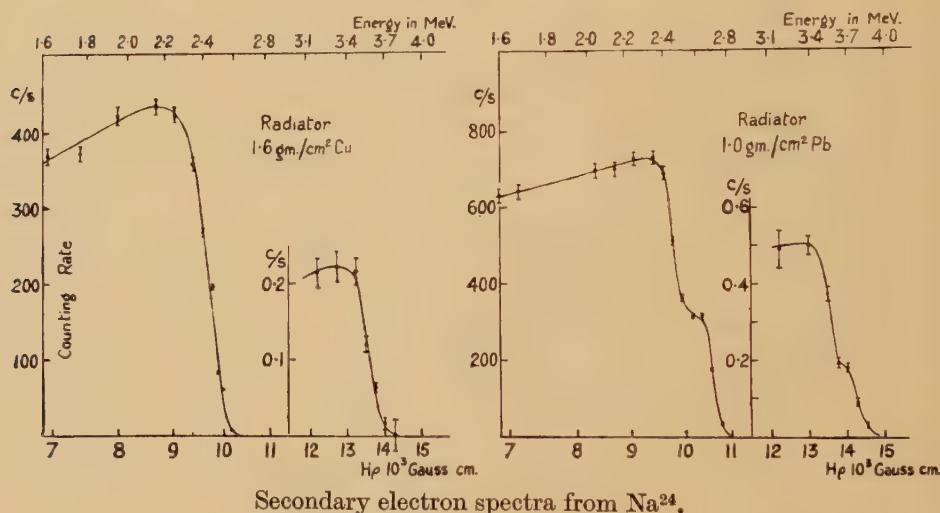
Fermi plot of high energy β -rays of Na²⁴.

obtained (fig. 3) were quite different from the β -ray distribution, and had maxima in about the expected place. Some evidence of a photoline was obtained in the case of a lead radiator, but the value obtained for the energy of the γ -ray from the photoline position, no correction being made for the finite thickness of the radiator, was some 8 per cent lower than the energy expected for the cross-over γ -ray of 4.14 MeV. The value obtained from an extrapolation of the Compton distribution was 4 per cent lower than 4.14 MeV. The values obtained for the energy of the 2.76 MeV. γ -ray

from the Compton distribution and photoline; however, were correct within 1 per cent after applying the 1 per cent correction in the energy of the photoline due to the saturation thickness of radiator, found to be appropriate at lower energies. It is felt, however, that the results are not necessarily incompatible with a γ -ray of energy equal to the cross-over γ -ray, since at 4 MeV., in lead, energy loss of fast electrons by bremsstrahlung, is becoming important, and may effect the shape of both Compton and photoelectric distributions with a thick radiator. However, the possibility remains that the γ -ray is some 4–7 per cent lower in energy than the cross-over, though this does not appear to be likely theoretically.

By comparing the two Compton distributions the relative intensities of the high energy and the 2.76 MeV. γ -rays was determined as 5×10^{-4} , a result completely incompatible with that of the Oxford group. The results

Fig. 3.

Secondary electron spectra from Na^{24} .

of chemical analysis of both the sodium fluoride and a later source of anhydrous sodium carbonate, however, leave little doubt that the γ -ray arises from the neutron irradiation of sodium, and measurements made with sources irradiated under cadmium, and in a lower neutron flux, exclude the possibility of a fast neutron reaction or neutron capture by Na^{24} giving rise to the radiation. This, together with an approximate measurement of half-period makes it reasonably certain that the γ -ray is associated with the decay of Na^{24} .

§ 6. DISCUSSION.

If the high energy γ -ray and the 2.76 MeV. γ -ray do in fact arise from the same level, the use of the Segre-Helmholtz formula, and the relative intensities, indicates that they differ by one order of multipolarity, and that consequently, the parities of the ground and intermediate states of Mg^{24} differ. This demands that the 1.38 MeV. γ -ray be of odd multipole

order, almost certainly dipole, and is incompatible with the angular correlation measurements. In the case, however, where the 2.76 MeV. γ -ray is dipole, since it is known that the probabilities of emission of dipole and quadrupole radiation are about equal, it is possible that the cross-over γ -ray could be octupole. This would require that the β -transition to the intermediate state, with a spin change of 2 and no parity change, should be second forbidden, and does not appear to be at all likely. The interpretation of the $f\tau$ values of the various β -transitions is difficult because of uncertainty in the magnitude of the nuclear matrix elements. However, if the main β -transition is first forbidden, it is probable that the 4.14 MeV. β -ray is at least third forbidden, and the 5.53 MeV. β -ray at least fourth forbidden.

ACKNOWLEDGMENT.

Acknowledgment is made to the Director, A.E.R.E., for permission to publish.

REFERENCES.

- BEGHIAN, L. E., GRACE, M. A., PRESTON, G., and HALBAN, H., 1950, *Phys. Rev.*, **77**, 286.
BISHOP, G. R., WILSON, R., and HALBAN, H., 1950, *Phys. Rev.*, **77**, 416.
BRADY, E. L., and DEUTSCH, M., 1950, *Phys. Rev.*, **78**, 558.
CAVANAGH, P. E., 1950, *Proc. Harwell Nuclear Physics Conference*, p. 98.
GRANT, P. J., 1950, *Proc. Phys. Soc. A*, **63**, 1298.
MIMS, W., HALBAN, H.; and WILSON, R., 1950, *Nature, Lond.*, **166**, 1027.
RAE, E. R., 1949, *Phil. Mag.*, **40**, 1155.
RHODERICK, E. H., 1949, *Nature, Lond.*, **163**, 898.

LXVII. *The Thermal Conductivity of Some Alloys at Low Temperatures.*

By R. BERMAN,
Clarendon Laboratory, Oxford*.

[Received March, 29, 1951.]

ABSTRACT.

The thermal conductivities of German silver, stainless steel and constantan have been determined between 2 and 90° K. and the electronic and lattice components of the conductivity have been calculated.

The electronic conductivity is limited by scattering by "impurities". The lattice conductivity is limited by scattering of the lattice waves by electrons at the lower temperatures and by "impurities" at higher temperatures.

A table is given showing the heat flow along specimens of each alloy resulting from temperature differences commonly met with in practice in low-temperature work.

§1. INTRODUCTION.

Of the various sets of experiments which have been made on the thermal conductivity of alloys at low temperatures the most detailed have been concerned with superconducting alloys. Measurements have been made on other alloys by Karweil and Schäfer (1939), Allen and Mendoza (1948), Wilkinson and Wilks (1949), Schmeissner and Meissner (1950) and by Hulm (1951).

The present experiments, on German silver, constantan and a stainless steel, were made originally because of their practical value and cover a wider temperature range than do any of the previous experiments. The thermal conductivity was measured between 2 and 90° K. and the electrical conductivity at a few temperatures in this interval.

The electronic contribution to the heat conductivity has been estimated and, by subtracting this from the total conductivity, the lattice heat conductivity has been deduced. This is an appreciable fraction of the total conductivity over the temperature range of these measurements. It is shown that up to about 25° K. the lattice conductivity is limited mainly by scattering of the lattice waves by electrons, but that above this temperature "impurity" scattering predominates.

§2. THE EXPERIMENTS.

The apparatus used was the same as that described elsewhere (Berman 1951), in which the temperature drop along the specimens is measured by two gas thermometers. The thermometers were fixed with Wood's metal

* Communicated by Professor F. E. Simon, F.R.S.

to copper bands soldered to the specimens. The measurements of electrical conductivity were made in the same apparatus.

The German silver was in the form of a $\frac{1}{4}$ -inch rod, obtained from Messrs. Rollets, with composition Cu 47 per cent, Pb 2 per cent, Zn 41 per cent, Ni 9 per cent, and was measured as received. The grain size was estimated from a photomicrograph, using a grain contrast etch. The mean diameter was in the region of 0.02 mm.

For the main experiments the length used was 5 cm., but two measurements were also made with a length of 2.5 cm. This was to verify (1) that the length to be assumed for calculating the conductivity is equal to the distance between the centres of the bands soldered to the specimen, and (2) that the corrections for heat losses are as small as had been calculated ($2\frac{1}{2}$ per cent at 95° but less than $\frac{1}{2}$ per cent below 60° K.). The agreement between the two sets of experiments is very close (○ and ○ in fig. 1) and it was not considered necessary to repeat this check for the other alloys.

As the ratio of the room temperature electrical resistance to the residual resistance was very small (1.1) compared with the value found by Allen and Mendoza for a rod of similar composition, the specimen was given a similar heat treatment and heated to a dull red heat for a few minutes and allowed to cool slowly. The resistance ratio was, however, unaltered.

The constantan specimen (Cu 60 per cent, Ni 40 per cent) consisted of 317 enamelled wires of 36 gauge, in parallel. These measurements were made because constantan leads of about this gauge are frequently used in various low-temperature apparatus in which it is necessary to estimate the heat flow down them. The wires were soldered together at their ends and two copper collars were soldered round them at a distance apart of 3.5 cm.

The stainless steel specimen consisted of three rods, of 2 mm. diameter, in parallel. This was an austenitic 18/8 titanium stabilized material of composition Ni 7.9 per cent, Cr 18.9 per cent, Si 0.7 per cent, Ti 1 per cent, C about 0.1 per cent. The austenite grains were estimated to be about 0.01 mm. with some ferrite grains of about 0.002 mm. precipitated in the grain boundaries of the austenite.

§ 3. RESULTS.

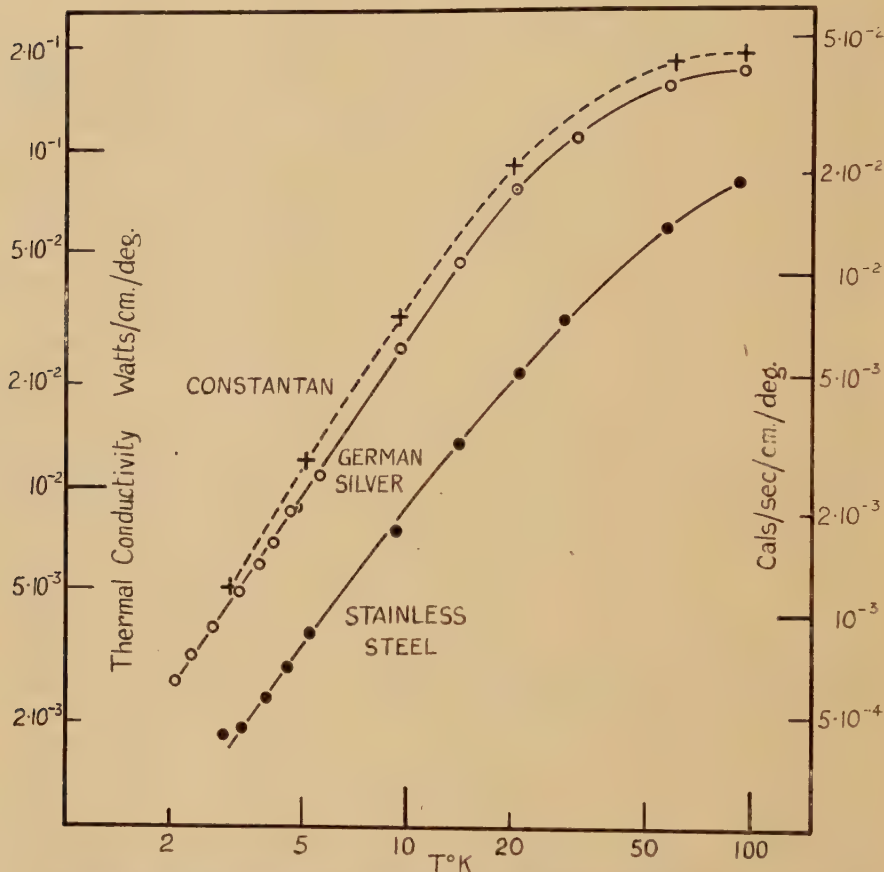
The thermal conductivity and electrical resistivity of these alloys are shown in figs. 1 and 2. For the three alloys the thermal conductivity at the lowest temperatures varies as a power of the absolute temperature slightly greater than 1. At higher temperatures the conductivity becomes less temperature dependent.

These results can be compared with those of other authors. The German silver specimen had a similar composition to both the German silver measured by Allen and Mendoza and the "Silver bronze" measured by Karweil and Schäfer. Allen and Mendoza found, for a specimen with much lower electrical resistivity, that the thermal conductivity, measured between 1.3 and 4° K., was proportional to the cube of the absolute temperature. Hulm has raised some doubts as to the validity of the values

found by these authors. The present results agree well, however, with those of Karweil and Schäfer who measured between 5 and 24° K. The extrapolated value at 113° K. is in good agreement with the value determined by Lees (1908) on a specimen of somewhat different composition which had a similar electrical resistivity.

The values obtained on stainless steel are slightly higher than those of Wilkinson and Wilks between 10 and 20° K. on a specimen of similar

Fig. 1.



Thermal conductivities of German silver, stainless steel and constantan.

composition. They are, as would be expected, considerably lower than those of Karwell and Schäfer who measured a steel with only 1 per cent of "foreign" atoms.

It is of interest to note that below about 20° K. the thermal conductivity of this stainless steel is very similar to that of "contracid", measured by Karweil and Schäfer, and of "chroman B2Mo", measured by Schmeissner and Meissner. The apparent rapid rise of conductivity above 70° K. found by the latter authors for chroman B2Mo has not been found for stainless steel.

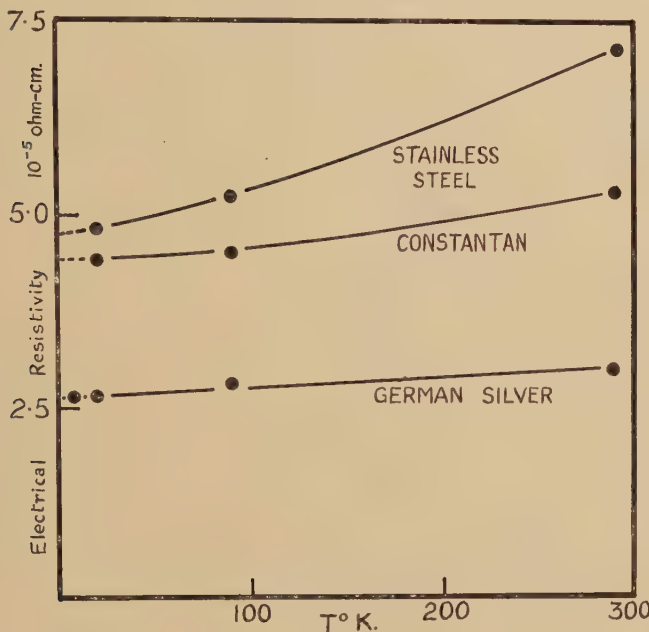
There seem to be no previous measurements on constantan in the temperature range of the present experiments, but the values are similar to those found for another Cu-Ni alloy by Hulm, below 20° K.

§ 4. DISCUSSION OF RESULTS.

The heat conducted by a metal or alloy is the sum of the heat conducted by the electrons and by the lattice. The heat conductivity, K , can therefore be written

$$K = K_e + K_g,$$

Fig. 2.



Electrical resistivities of German silver, stainless steel and constantan.

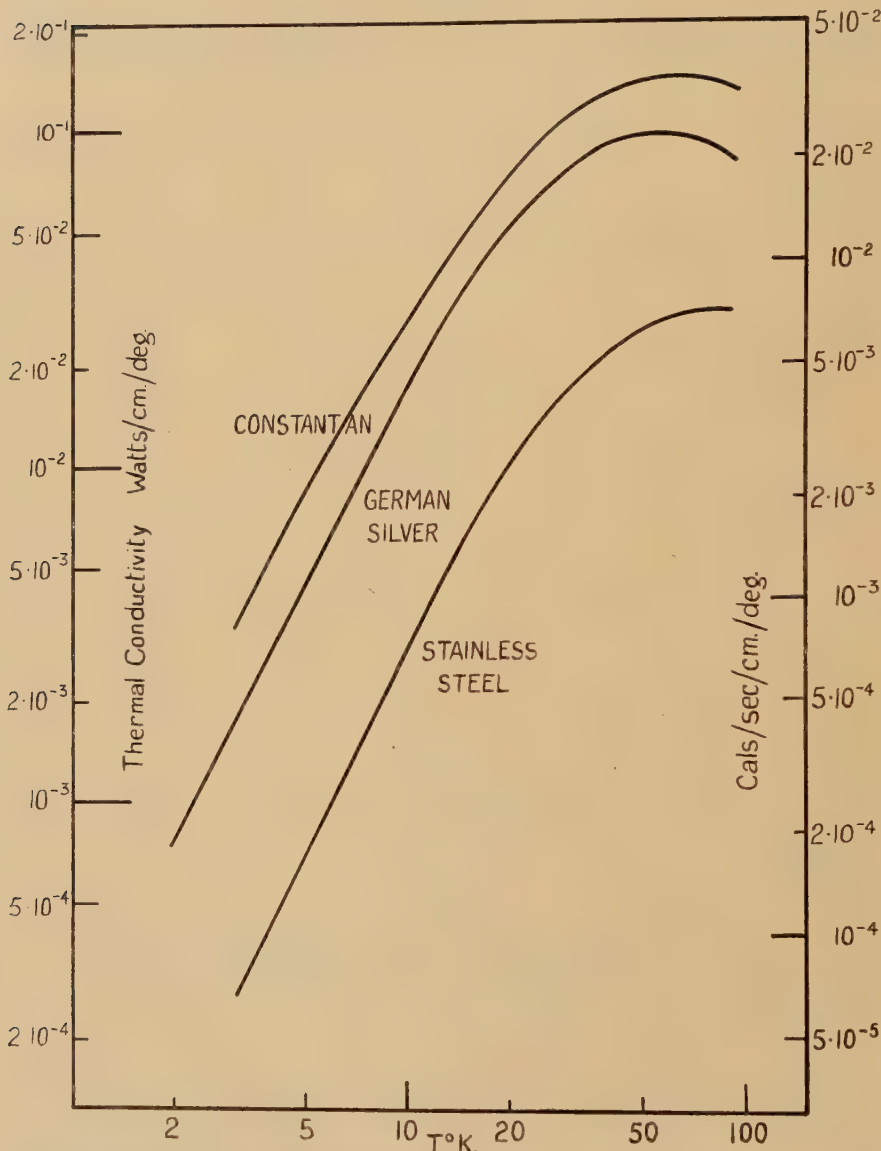
where K_e is the electronic heat conductivity and K_g the lattice conductivity. These two components are determined by the processes which scatter electrons and phonons (lattice waves) respectively and give rise to heat resistance.

Heat conducted by the electrons.

The electronic thermal resistivity, $W_e (=1/K_e)$, is, to a first approximation, the sum of the "ideal" resistance W_i , due to the thermal vibrations of the atoms, and the resistance due to the aperiodicity of the lattice field produced by the presence of "impurities". According to Makinson (1938) the ideal resistance of a metal at low temperatures should be proportional to the square of the absolute temperature. Although this ideal thermal resistance is not simply related to the ideal electrical resistivity, the thermal resistance which is due to impurities should be directly related to

the residual electrical resistance, ρ_0 , by the Wiedemann-Franz-Lorenz law and is therefore equal to $\rho_0/L_0 T$, where L_0 is the Lorentz constant ($\frac{1}{3}(\pi k/e)^2 \equiv 2.45 \times 10^{-8}$ Watt-ohm/deg.²). From measurements by

Fig. 3.



Calculated lattice thermal conductivities in German silver, stainless steel and constantan.

Grüneisen and Goens (1927) of the thermal conductivity of copper and iron it is possible to estimate the order of magnitude of W_i for the alloys measured. Using the extrapolated values of ρ_0 from fig 2, W_i is about

1 per cent of ρ_0/L_0T for German silver and constantan at 90° K. and about 2 per cent for stainless steel.

As W_i decreases with decreasing temperature while ρ_0/L_0T increases, the electronic resistance can be ascribed to impurity scattering over the range of the present experiments. The electronic conductivity is therefore L_0T/ρ_0 , and the lattice conductivity, K_g , must be $K = L_0T/\rho_0$.

Heat conducted by the lattice.

The lattice conductivity for the three alloys is shown in fig. 3. Up to about 20° K. it is proportional to T^2 , but above this temperature it increases more slowly and reaches a maximum value. In the case of German silver, the lattice conductivity decreases with increasing temperature at the highest temperatures at which measurements were made.

In the same way as the electronic thermal resistance can be considered as the sum of the resistances due to different scattering processes, so the thermal resistivity of the lattice, W_g , is due to several processes which scatter the momentum of the phonons. The resistances due to these causes are not strictly additive but there are temperature regions in which one process is dominant and may be identified by the temperature variation of the resistance.

W_U is the resistance due to "Umklapp" processes by which the phonons mutually interact. At low temperatures $W_U \propto T^\nu e^{-\theta/2T}$, where ν is a constant and θ is the Debye characteristic temperature (Peierls 1929).

W_D is the resistance due to small scale lattice defects and impurities. At low temperatures $W_D \propto T$ but is less temperature dependent at high temperatures.

W_B is the resistance due to scattering of phonons at the grain boundaries and is proportional to T^{-3} (Casimir 1938).

These three scattering processes are also present in dielectric crystals, and the temperature dependence of the resistances due to them have been verified in other experiments (Berman 1951). In metals and alloys there is an additional resistance due to scattering of phonons by electrons; this resistance may be written as W_E and should be proportional to T^{-2} at low temperatures according to Makinson.

For German silver the lattice resistivity, $1/K_g$, has been analysed into these various components, as shown in fig. 4.

W_U is estimated roughly from measurements on dielectrics having a similar value for θ (~ 300 ° K.). W_U is of the order of 10 per cent of the total lattice resistance at 95° K. and this ratio falls off very rapidly with decreasing temperature.

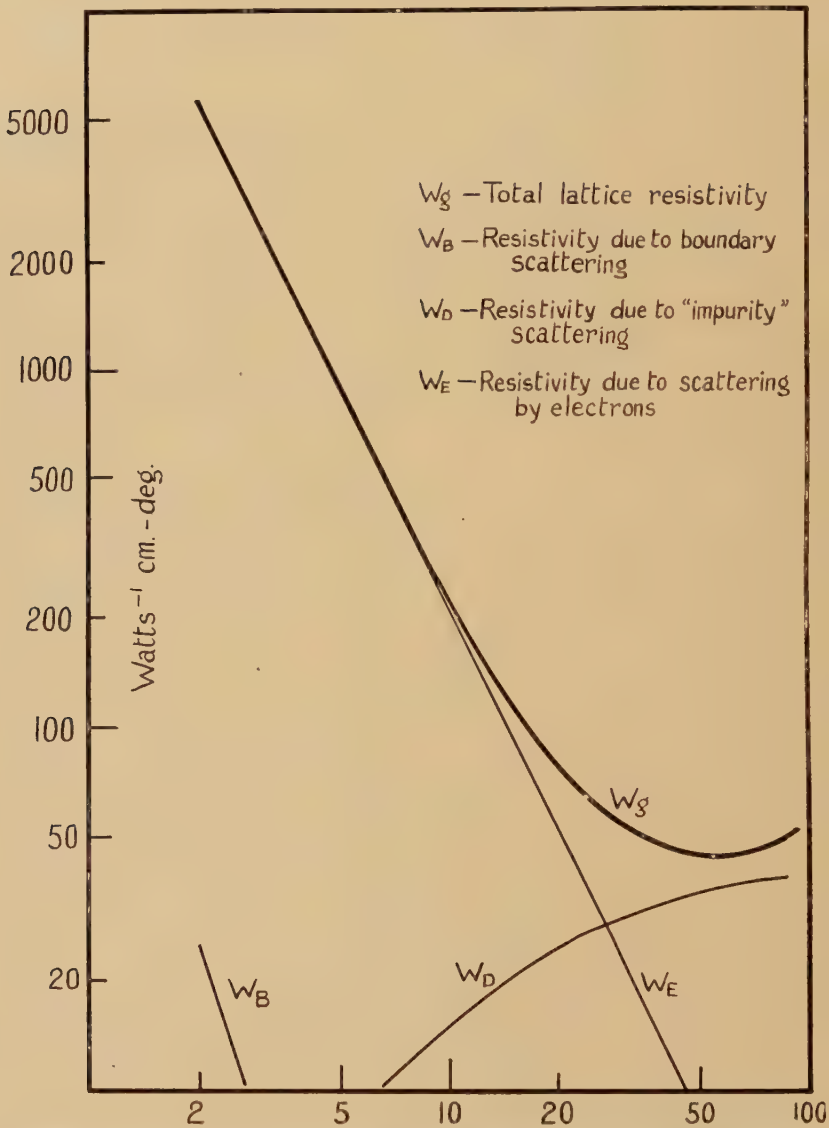
W_B is calculated from Casimir's formula

$$W_B \simeq 4.5 \times 10^{-6} \theta^2 / r T^3 \text{ Watts}^{-1} \text{ cm.-deg.,}$$

where r is the linear dimension of the grains. Taking θ as 300° K. and r as 0.02 mm., W_B is about 25 Watt $^{-1}$ cm.-deg. at 2° K., which is only $\frac{1}{2}$ per cent of the total resistance at this temperature. At higher temperatures this ratio falls off very rapidly.

In the temperature range of the experiments the lattice resistance can therefore be attributed mainly to W_D and W_E . At the lowest temperatures W_g is seen to be proportional to T^{-2} ; this is the temperature dependence of the lattice resistance, W_E , due to scattering of phonons by electrons.

Fig. 4.



Estimated contributions to the lattice thermal resistivity in German silver from scattering of phonons by electrons, "impurities" and grain boundaries.

Assuming that W_E follows the same relation to higher temperatures, W_D can be deduced, since $W_g = W_U + W_E + W_D$. In agreement with theory, W_D is found to be proportional to T at the lowest temperatures but to become less temperature dependent at higher temperatures.

§ 5. CONCLUSIONS.

In the alloys measured the heat conducted by the electrons and by the lattice are of the same order of magnitude. The electronic conductivity is limited by scattering due to the aperiodicity of the lattice, and the "ideal" resistance due to thermal vibrations is negligible below 100° K. The lattice conductivity appears to be limited mainly by scattering of the lattice waves by the electrons at the lower temperatures, and by the "impurities" at higher temperatures.

In the case of German silver if the effect of the electrons were removed the heat conducted by the lattice would increase to a value which, below 4° K., would be determined by the boundary scattering and not by the percentage of "impurity" in the alloy.

Mendelssohn and Olsen (1950) have found that, in contrast to the behaviour of most metals, for some alloys of lead and for columbium the heat conductivity is greater in the superconducting state than in the normal state. To explain this they postulate a circulation heat flow analogous to that which has been used to account for the high heat conductivity of liquid helium II. Hulm (1950) has suggested that for these specimens the lattice conduction is appreciable and increases when the specimen becomes superconducting owing to the reduction in the number of electrons capable of scattering the lattice waves. If this is so, then, although the electronic conductivity decreases, the total conductivity in the superconducting state may be higher than in the normal state.

For the metals and alloys on which such experiments have been made, the impurity concentrations are much smaller than in German silver, so that the thermal resistance due to them will also be smaller. For relatively large grains (1/10 to 1 mm.) therefore, the lattice resistance due to even 1 per cent of impurity would be less than the resistance due to boundary scattering at 2° K. If at this temperature the electrons no longer take part in both heat conduction and in scattering of lattice waves, then the total conductivity would increase by a large factor.

It would therefore be of interest to determine the electronic and lattice conductivities, in the normal state, and the grain sizes of specimens which show the behaviour found by Mendelssohn and Olsen. It might then be possible to decide whether it is necessary to postulate a new heat transport mechanism to explain their results.

APPENDIX.

In the design of low temperature apparatus it is often necessary to calculate the heat flow, along tubes or wires, between parts which are at very different temperatures. If the temperatures at the end of a specimen 1 cm. long are T_1 and T_2 , the heat flow per unit area per second is equal to $\int_{T_1}^{T_2} K dT$ and may be considered as $(T_2 - T_1)\bar{K}$, where \bar{K} is the "mean" conductivity in the temperature interval T_1 to T_2 .

For convenience, the following table gives the heat flowing along specimens of German silver and stainless steel, 10 cm. long and 1 sq. mm. cross sectional area, and along a constantan wire of 36 gauge (2.9×10^{-2} mm.²), also 10 cm. long, when the temperatures at the ends vary from 80° to 0° K.

Rate of Heat Flow along Specimen—in watts.

Temperatures at ends of Specimen °K.		German Silver 10 cm. long 1 mm. ² cross-section	Stainless Steel 10 cm. long 1 mm. ² cross-section	Constantan 36 gauge (2.9×10^{-2} mm. ²) 10 cm. long
T ₂	T ₁			
80	20	8.0×10^{-3}	3.0×10^{-3}	2.7×10^{-4}
60	20	4.8×10^{-3}	1.7×10^{-3}	1.6×10^{-4}
20	4	5.8×10^{-4}	1.7×10^{-4}	2.1×10^{-5}
10	4	9.3×10^{-5}	3.1×10^{-5}	3.5×10^{-6}
4	1	1.0×10^{-5}	4.2×10^{-6}	3.5×10^{-7}
1	0	4.0×10^{-7}	1.8×10^{-7}	1.0×10^{-8}

As these heat flows are often of interest in the determination of the volumes of liquid hydrogen and liquid helium which they cause to be evaporated, it should be noted that 1 watt evaporates about 100 c.c. of liquid hydrogen per hour and about 1 litre of liquid helium per hour.

ACKNOWLEDGMENTS.

I should like to thank Professor F. E. Simon, F.R.S., for his continued interest in the work, also Dr. J. W. Christian for the grain size determinations.

REFERENCES.

- ALLEN, J. F., and MENDOZA, E., 1948, *Proc. Camb. Phil. Soc.*, **44**, 280.
 BERMAN, R., 1951, To be published in *Proc. Roy. Soc. A*.
 CASTIMIR, H. G. B., 1938, *Physica*, **5**, 495.
 GRÜNEISEN, E., and GOENS, E., 1927, *Z. Phys.*, **44**, 615.
 HULM, J. K., 1950, *Proc. Roy. Soc. A*, **204**, 98; 1951, *Proc. Phys. Soc. B*, **64**, 207.
 KARWEIL, J., and SCHÄFER, K., 1939, *Ann. Phys., Lpz.*, **36**, 567.
 LEES, C. H., 1908, *Phil. Trans. Roy. Soc. A*, **208**, 381.
 MAKINSON, R. E. B., 1938, *Proc. Camb. Phil. Soc.*, **34**, 474.
 MENDELSSOHN, K., and OLSEN, J. L., 1950, *Proc. Phys. Soc. A*, **63**, 2, 1182.
 PEIERLS, R., 1929, *Ann. Phys. Lpz.*, **3**, 1055.
 SCHMEISSNER, F., and MEISSNER, H., 1950, *Z. angew. Phys.*, **2**, 423.
 WILKINSON, K. R., and WILKS, J., 1949, *J. Sci. Instrum.*, **26**, 19.

LXVIII. *Observation of Cosmic Ray Events in Nuclear Emulsions Exposed in a Glacier at 3550 m.*

By J. B. HARDING*,
Imperial College, London †.

[Received March 7, 1951.]

ABSTRACT.

Photographic emulsions have been exposed at various depths under ice at 3550 m. The variation in the numbers of slow μ -mesons with depth is in fair agreement with a predicted variation.

From the variation of the numbers of "stars" with depth, the best estimate for the absorption mean free path of the star producing radiation is 170 ± 10 gm./cm.².

The variation of the numbers of π^+ -mesons with depth is consistent with an absorption path length for nuclear interaction corresponding to a few times the geometric value. A large upward stream of π -mesons has been observed and possible interpretations are discussed.

§1. INTRODUCTION.

In previous notes (Harding *et al.* 1949 a and b) we have reported results on the absorption of the star producing radiation and on the variation of the number of π -mesons with depth in ice. In order to improve the statistics and the geometry, the experiment at the Jungfraujoch 3550 m. has been repeated. Experimental results for stars and mesons will be given.

§ 2. EXPERIMENTAL DETAILS.

In order to obtain good geometry a steel pipe ($2\frac{1}{8}$ -in. internal diameter, $\frac{3}{16}$ -in. wall thickness) closed at the lower end was sunk vertically to a depth of 9 m. into a glacier. Boxes of plates coated with Ilford G.5 "Nuclear Research" emulsion 200 μ thick were exposed vertically at depths down to 5 m. for 89 days. The pre- and post-exposure amounted to about four days spent mainly at sea level. Plates were also exposed at depths of $6\frac{1}{2}$ and $8\frac{1}{2}$ m., but these emulsions were poured at the Jungfraujoch under a large thickness of rock. The pre- and post-exposure of these plates amounted to 2 hours at 3550 m. The spaces between the boxes in the top 3 m. of pipe were filled with cylinders of paraffin wax, density 0.9 gm./c.c., which should produce nearly the same effects on cosmic ray particles as ice itself.

* Present address, Atomic Energy Research Establishment, Harwell.

† Communicated by Sir George Thomson, F.R.S.

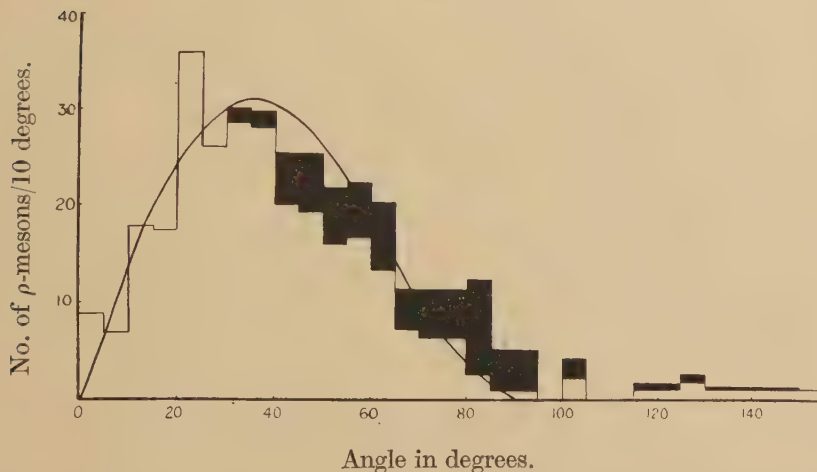
TABLE I.

		0	45	90	135	180	225	270	360	450	585	765
1.	Depth in gm./cm. ² ice
2.	Stars observed	905	455	470	530	543	238	262	114
3.	Stars/c.c./day	$\{$	16.2 ± 0.5	10.6 ± 0.5	6.6 ± 0.3	5.3 ± 0.2	3.8 ± 0.16	2.8 ± 0.15	1.8 ± 0.11
4.	Star rate corrected for pre-exposure $\{$	16.2 ± 0.5	10.6 ± 0.5	6.6 ± 0.3	5.3 ± 0.2	3.8 ± 0.16	2.8 ± 0.15	1.8 ± 0.11	1.02 ± 0.1	0.48 ± 0.05	0.18 ± 0.03	0.07 ± 0.02
5.	No. of π^+ -mesons - 0-60°	1	10	16	20	16	10	9	3	4
6.	60-90°	2	4	10	10	7	3	5	3	1
7.	90-120°	10	9	4	10	4	2	7	1	0
8.	120-180°	8	3	3	8	2	1	3	2	1
9.	No. of π^+ -mesons 0-60°	1	12	18	27	16	12	8	5	2
10.	60-90°	8	7	11	15	9	5	9	6	3
11.	90-120°	14	5	6	9	4	4	6	1	3
12.	120-180°	10	7	6	9	6	4	7	2	2
13.	[π^+ -mesons (0-60°)/stars] 100	..	$\{$	0.022 ± 0.016	0.48 ± 0.11	0.68 ± 0.12	0.89 ± 0.13	0.59 ± 0.10	0.92 ± 0.21	0.80 ± 0.17	0.96 ± 0.17	0.84 ± 0.28
14.	ρ -mesons/c.c./day 0-90°	..	$\{$	2.56 ± 0.21	2.70 ± 0.25	2.35 ± 0.18	2.50 ± 0.16	2.03 ± 0.12	2.08 ± 0.14	2.03 ± 0.12	1.41 ± 0.12	1.30 ± 0.12
15.	90-180°	..	$\{$	0.26 ± 0.06	0.23 ± 0.07	0.19 ± 0.06	0.16 ± 0.04	0.16 ± 0.04	0.14 ± 0.13	0.16 ± 0.13	0.09 ± 0.03	0.07 ± 0.02
16.	μ -mesons/c.c./day 0-90°	..	$\{$	2.50 ± 0.23	2.48 ± 0.28	2.09 ± 0.20	2.28 ± 0.16	1.94 ± 0.13	1.99 ± 0.15	1.37 ± 0.13	1.28 ± 0.13	1.16 ± 0.08
17.	90-180°	..	$\{$	0.04 ± 0.08	0.08 ± 0.08	0.07 ± 0.07	0.07 ± 0.05	0.12 ± 0.04	0.08 ± 0.04	0.06 ± 0.03	0.06 ± 0.02	0.03 ± 0.02

§ 3. EXPERIMENTAL RESULTS.

In Table I. the frequency of occurrence of the various events are shown. We have assumed that the density of ice was uniform and equal to 0.9 gm./c.c. Only ρ -mesons of projected lengths greater than $130\ \mu$ have been recorded; a ρ -meson being defined as one that does not produce a visible star nor that gives rise to a secondary meson. The numbers of π^+ -mesons which stop in the emulsions and are travelling at angles $0-60^\circ$, $60-90^\circ$, $90-120^\circ$, $120-180^\circ$ with the downward vertical at their points of entry, are given. All errors given represent standard deviation, based on the numbers of events recorded. Non-uniformity of the emulsion thickness may introduce additional errors of about 5 per cent. A random sample of plates were searched twice and by this means the overall efficiency for recording stars was estimated as 97 per cent, while for ρ -mesons the efficiency was about 80 per cent.

Fig. 1.



Angular distribution of ρ -mesons. The shaded areas must be added to the observed distribution (unshaded histogram) in order to correct for loss of tracks at large zenith angles caused by the thinness of the emulsion.

The angular distribution of ρ -mesons arriving at the plate is shown in fig. 1. This distribution has been obtained by measuring 100 mesons at each of the following depths:—0, 180 and 585 gm./cm.². Since mesons making large zenith angles have a smaller chance than those of small zenith angles of producing a track of at least $130\ \mu$ (and therefore of being recorded), this distribution is weighted to small angles. By considering the distribution in the angle of dip for various zenith angles approximate correction factors have been obtained and the corrected distribution is shown by the addition of shaded areas. The curve in this figure represents a $\cos^2 \theta$ distribution per unit solid angle.

The ρ -mesons that we observe represent three types of events:—

(a) 28 per cent of π^- -mesons leave no visible star on coming to rest in the emulsion (Bradner 1949) and these will be recorded as ρ -mesons.

(b) Some will be μ^+ -mesons produced from decay at rest of π^+ -mesons in the immediate neighbourhood of the emulsion, the π^+ -mesons having been locally created.

(c) The majority are the μ^+ -mesons which form the hard component of cosmic rays.

We shall now estimate the quantities (a) and (b) and obtain by subtraction those mesons which form the hard component.

For every 100 π^- -mesons which produce stars,

$$28 \left(\frac{100}{100-28} \right) = 39 \pi^- \text{-mesons}$$

stop in the emulsion and fail to produce stars. Only 80 per cent of the π^- -mesons which produce stars have ranges exceeding 130μ and there is no reason to suppose that this ratio will be different for those π^- -mesons which produce no visible star. Because of searching inefficiency only 80 per cent of ρ -mesons of lengths greater than 130μ are recorded. Therefore for every 100 π^- -mesons which produce stars $39 \times 0.8 \times 0.8 = 25 \pi^-$ -mesons will be recorded as ρ -mesons.

It is estimated that for every 100 π^+ -mesons stopping in the emulsion, $37 \mu^+$ -mesons (of length greater than 130μ) will also stop in the emulsion due to the decay at rest of π^+ -mesons in the surrounding material which is assumed to have the same stopping power as the emulsion itself. The slightly (~ 20 per cent) lower stopping power of glass, which, with the emulsion of the neighbouring plates, forms the bulk of the surrounding material, will only produce a second order correction. From range measurements on the μ^+ of $\pi-\mu$ events, it is estimated that we record only about 80 per cent of the π^+ -mesons which stopped in the emulsion and as stated above, the searching efficiency for ρ -mesons of length greater than 130μ was also about 80 per cent. Thus for every 80 π^+ -mesons observed to stop in the emulsion approximately $37 \times 0.8 = 30 \mu^+$ -mesons are observed as ρ -mesons.

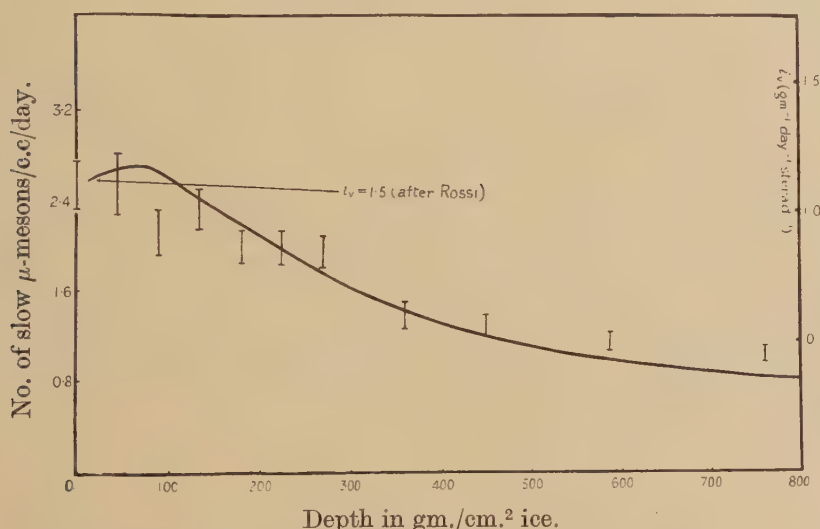
Therefore, for every 180 π -mesons (80 π^+ - and 100 π^- -mesons) observed to stop, $30 + 25 = 55$ mesons are recorded as ρ -mesons, and must be associated with the π -mesons rather than with the μ^+ -meson of the hard component. By subtracting $55/180 \sim 30$ per cent of the numbers of π -mesons at any depth from the numbers of ρ -mesons observed, we are left with the numbers of μ -mesons of the hard component. The values are shown in rows 16 and 17 of Table I. It is seen that only about 4 per cent of the μ -mesons travel upwards, and this upward stream can reasonably be attributed to Coulomb scattering.

Working from the energy spectrum of μ -mesons at sea level, and the variation of the μ -meson intensity with altitude, Sands (1950) has derived the expected form of the differential range distribution of μ -mesons in

air at mountain altitudes. The experimental results for the numbers of μ -mesons (Table I. row 16) travelling downwards and coming to rest in the emulsion, are plotted against depth of ice in fig. 2. Sands' curve, in arbitrary units, has been corrected for the different medium (ice instead of air) and is shown in this figure. Thus assuming no μ -mesons are produced in the ice, other than by the decay of π -mesons, the variation with depth in ice of the number of slow mesons, is in fair agreement with the predicted variation.

As regards the absolute flux of μ -mesons, Rossi (1948) has given the absolute value i_ν of the differential range spectrum at 10 gm./cm.² at various atmospheric depths, *i. e.* the number of μ -mesons/day/steradian in the vertical direction, which stop in one gram of air at various depths in

Fig. 2.



the atmosphere. At 3550 m. $i_\nu = 1.5 \text{ gm.}^{-1} \text{ diem.}^{-1} \text{ sterad.}^{-1}$. This fixes the ordinate of Sands' curve. In order to compare our intensity with Rossi's value we have to correct for

- (a) the angular distribution of the mesons ($\cos^2 \theta$ per sterad),
- (b) loss due to thin emulsions. We have recorded only mesons of length $\geq 130 \mu$ whereas we require the numbers of mesons of length greater than zero,
- (c) relative stopping powers per gram of air and emulsion (1 gm. air $\equiv 1.7$ gm. emulsion $\equiv 0.43$ c.c. emulsion),
- (d) correction factor for searching efficiency is $1/0.8$.

We have recorded μ -mesons arriving at the plate and coming from the upper hemisphere. It is to be expected that a photographic emulsion records the "integrated intensity" of slow mesons, *i. e.* the number of

mesons recorded depends on the volume, but not the shape of the emulsion. Correction (*a*) is straightforward inasmuch as we have to compare the integrated intensity per sterad around the vertical with that of the upper hemisphere-correction factor is

$$\lim_{\epsilon \rightarrow 0} \frac{\int_0^\epsilon 2\pi \cos^2 \theta \sin \theta d\theta / \int_0^\epsilon 2\pi \sin \theta d\theta}{\int_0^{\pi/2} 2\pi \cos^2 \theta \sin \theta d\theta} = \frac{3}{2\pi}.$$

Scattering, when once the mesons have entered the emulsion, will make their distribution more nearly isotropic and thus we obtain a factor to correct for (*b*) in the manner described by Lattes *et al.* (1947). The factor so obtained is 1.7 and we feel confident that this is correct to ~ 20 per cent. We can now convert our intensities to Rossi's units by multiplying by $3/2\pi \times 1.7 \times 0.43 \times 1/0.8 = 0.44$. The right-hand ordinate scale of fig. 2 is given in these units. It is seen that the experimental figures are approximately 25 per cent lower than those obtained from counter experiments, and the reason for such a discrepancy may be partly in correction factor (*b*) and partly in (*a*). Although the observed angular distribution of ρ -mesons more nearly obeys a $\cos^2 \theta$ than a $\cos^3 \theta$ distribution, part of these mesons are μ^+ -mesons formed in the immediate neighbourhood of the emulsion. These should be isotropic. Hence the μ -mesons of the hard component should be more strongly collimated. A $\cos^3 \theta$ distribution, as has been suggested by Krauchaar (1949), would result in a correction factor for (*a*) of $4/2\pi$ instead of $3/2\pi$. Thus the discrepancy with counter experiments is not necessarily significant. From Sands' curve, it would seem that the flux of fast μ -mesons under 760 gm./cm.² of ice is $\sim 1000/\text{cm.}^2/\text{day}$.

Stars.

Owing to the long exposure and to low development, the recording of tracks of particles at minimum ionization was not reliable. This introduces a small uncertainty, which should be the same at all depths, in the classification of a star. We have recorded stars which have (*a*) at least one track longer than 60μ (*b*) at least three tracks with grain-densities greater than 30 grains/100 μ , *i.e.* $\sim 1\frac{1}{2} \times$ minimum, (*c*) a spur of less than 10μ was not counted as a track. The number of stars per c.c. of emulsion per day are plotted on a logarithmic scale against depth in fig. 3.

If the star producing radiation is coming vertically downward and is absorbed with a mean free path α , then the intensity at a depth x is given by

$$I = I_0 e^{-x/\alpha}. \quad \dots \quad (1)$$

The results do not fit such a relationship too well, though the best value of α for the first 300 gm./cm.² of ice would be 130–140 gm./cm.². There is a discrepancy with our earlier results (Harding *et al.* 1949 a)

from which a value of $\alpha=200 \text{ gm./cm.}^2$ was obtained. The difference can only be explained by poor geometry, *e.g.* large holes in the ice in the first experiment.

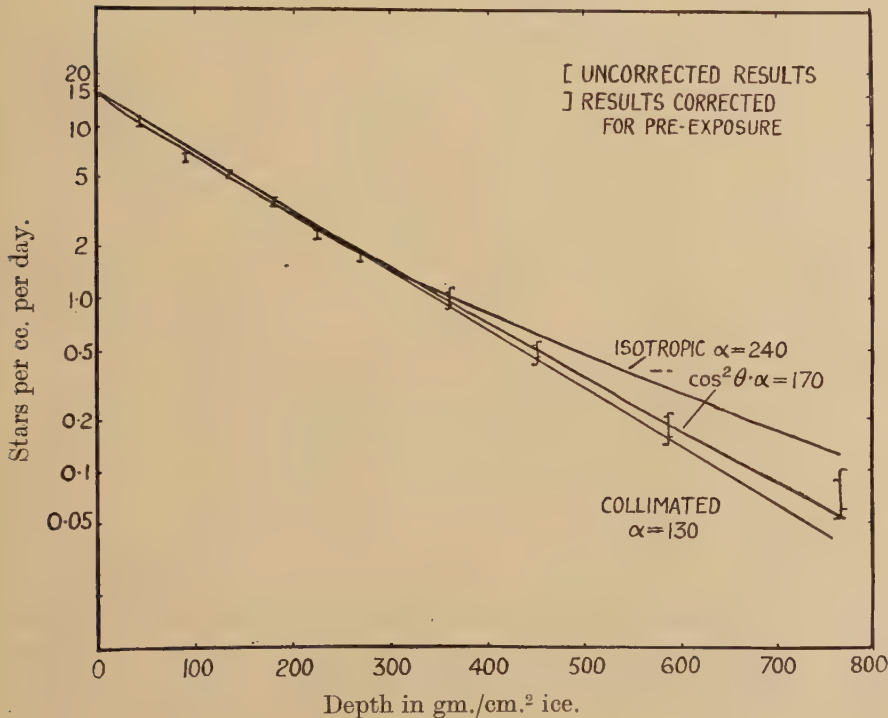
It may be argued that, because of an angular distribution of the star producing radiation, we should not expect exponential absorption. For an isotropic distribution at the ice surface of primaries, which are assumed to travel in straight lines, we would expect (see Rossi 1948)

$$\frac{I}{I_0} = e^{-x/\alpha} - (x/\alpha) Ei(-x/\alpha) \quad \dots \dots \dots \quad (2)$$

or for a $\cos^2 \theta$ distribution per unit solid angle

$$\frac{I}{I_0} = e^{-x/\alpha} \left(1 - \frac{1}{2}(x/\alpha) + \frac{1}{2}(x/\alpha)^2 - \frac{1}{2}(x/\alpha)^3 Ei(-x/\alpha)\right) \dots \dots \quad (3)$$

Fig. 3.



In order to obtain agreement between the experimental results and a theoretical curve over the first 300 gm./cm.² in the case of equation (2). There is then poor agreement for depths beyond 450 gm./cm.². In the case of equation (3), if we take $160 < \alpha < 180 \text{ gm./cm.}^2$ good agreement is obtained between the theoretical curve and the experimental points even down to 765 gm./cm.² of ice.

So far we have taken an exceptionally simple picture of the star production process inasmuch as we have assumed that all stars are produced by one component which is incident on the ice surface with

a certain ($\cos^2 \theta$) angular distribution. It seems likely that the star producing particles are not absorbed in a single nuclear encounter, or, what probably comes to the same thing, that in producing a star, the primary also produces one or more particles which can then act as primary particles for further stars, *i.e.* a cascade process. Provided these secondary particles have the same mean free path for star production and are produced at any depth with an angular distribution similar to that of the primary particles at that depth, then the above equations should equally apply for such a cascade process, but α no longer represents the absorption path length of the star producing radiations.

It is thought that the nucleonic component is mainly responsible for the production of stars. However George *et al.* (1950) have suggested a cross-section, σ , per nucleon for star production by μ -mesons of approximately 10^{-29} cm.². They have therefore shown ~ 0.1 stars/c.c./day should be produced in emulsion at 3550 m. This of course is negligible compared with the 16 stars/c.c./day observed at the ice surface. Production of fast μ -mesons in the ice is negligible and hence at 760 gm./cm.² of ice there are ~ 1000 fast μ -mesons crossing a square centimetre/day (see above). Thus the expected number of stars per c.c. per day produced by μ -mesons is $1000N\rho\sigma$ where N =Avagadro's number and ρ =density of emulsion. This comes to 0.024 stars/c.c./day which is approximately one-third of the observed number at the lowest point. About 15 per cent of the stars at 585 gm./cm.² of ice could be formed by μ -mesons. Thus even making allowance for stars formed by mesons, the experimental points still lie on a curve given by equation (3) with $\alpha=170\pm 10$ gm./cm.².

It is concluded that the experimental results are consistent with the assumption that the majority of stars are produced by primaries (nucleons) having an incident distribution $\cos^2 \theta$ per steradian and an apparent absorption mean free path of 170 ± 10 gm./cm.².

π -Mesons.

In a previous note (Harding and Perkins 1949 b) we obtained the variation in the number of π -mesons with depth in ice, and concluded that they were produced with a mean range ~ 100 gm./cm.² ice. Since then, an energy spectrum for the production of π -mesons in photographic emulsion has been obtained by Camerini *et al.* (1950). If we assume that this spectrum can be used to represent the production spectrum *in ice* we can obtain certain limits for λ , the absorption mean free path in nuclear interactions for fast π -mesons in ice.

It is assumed :—

- (a) the rate of production of mesons at a given depth is proportional to the star intensity at that depth,
- (b) mesons travel in straight lines,
- (c) the energy, or range distribution of mesons at production is independent of angle. Thus $q(R) dR . f(\theta) d\theta$ is the probability that

a meson is produced with a range R to R+dR at θ to $\theta+d\theta$ with the downward vertical. The spectrum $q(R) dR$ is obtained from Camerini's spectrum using a theoretical range-energy relation.

Let $P(x, \theta) d\theta$

$$= \frac{\text{No. of mesons stopping at depth } (x, dx) \text{ travelling at angle } (\theta, d\theta)}{\text{No. of stars at depth } (x, dx)},$$

where the star intensity (see above) can be approximated by

$$I/I_0 = e^{-x/\alpha}.$$

Let $g(R) dR$ be the probability that a meson of range R gm./cm.² ice will not decay in flight, i. e.

$$g(R) = \exp \left[- \int_0^R \frac{E_0 dR'}{c \beta \tau_0 (E + E_0)} \right]$$

E being the kinetic, and E_0 the rest energy of a meson. The lifetime τ_0 is taken as $7 \cdot 10^{-9}$ secs.

It can then be shown that

$$P(x, \theta) d\theta \propto \int f(\theta)/\cos \theta \int_{R=0}^{x/\cos \theta} e^{-\frac{R/\cos \theta}{\alpha}} e^{-R/\lambda} g(R) q(R) dR d\theta.$$

Considering mesons in the angular range 0–60°, we can write as a sufficient approximation

$$P(x) \bar{\theta} \propto \int_{R=0}^{x/\overline{\cos \theta}} e^{-\frac{R \overline{\cos \theta}}{\alpha}} e^{-R/\lambda} g(R) q(R) dR,$$

where we take $\overline{\cos \theta}$ as the average value of $\cos \theta$ for mesons arriving at the plate (fig. 5). $\overline{\cos \theta} = 0.77$. We take $\alpha = 130$ gm./cm.². The form of $P(x)$ can be obtained for various values of λ , and these are plotted in fig. 4 together with the experimental results. We have fitted theoretical curves to obtain the best agreement with the experimental points by a method somewhat analogous to least squares. We choose the ordinate scale for the theoretical curves such that $\sum_i e_i^2 / \sigma_i^2$ is a minimum, where

e_i is the difference between the experimental i th point and the curve, and σ_i is the uncertainty of the i th point.

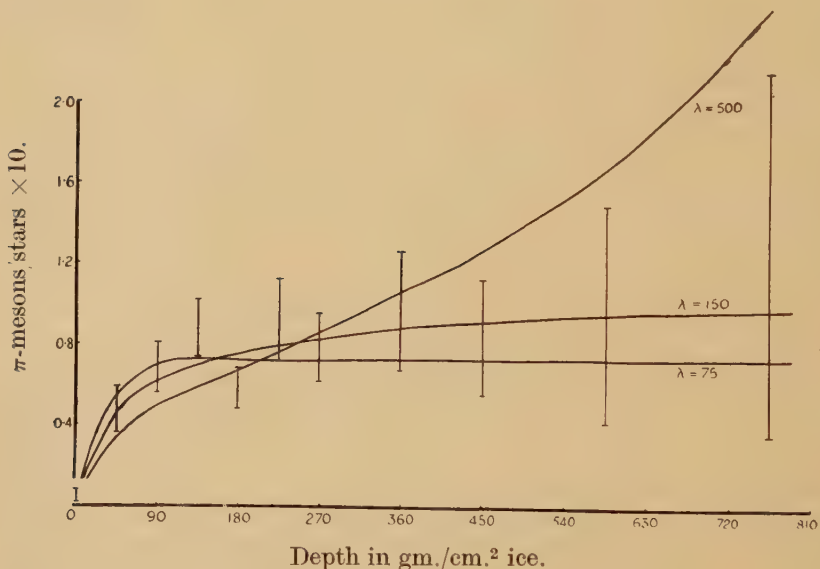
On this criterion, the experimental points best fit the curve for $\lambda = 150$ gm./cm.². The fit is about three times better than for $\lambda = 75$ and 90 times better than for $\lambda = 500$ gm./cm.². We conclude that the variation with depth of the number of π -mesons is consistent with an absorption path length for nuclear interaction corresponding to the geometric, or to a few times the geometric value of 70 gm./cm.² (neglecting the effect of hydrogen). If the proper lifetime of π -mesons is larger than we have assumed, say 10^{-8} instead of $7 \cdot 10^{-9}$ seconds, then small values of λ are still further favoured.

Assuming :—

- (a) mesons are produced only in oxygen in the ice ;
- (b) on the average the same number of mesons are produced in oxygen disintegrations, as in disintegrations of nuclei in photographic emulsion ;
- (c) the rate of nuclear disintegrations (and hence meson production) is proportional to the total geometrical cross-section of the nuclei, then we observe about $1\frac{1}{2}$ times as many mesons stopping as we would expect from a calculation in which a value of $\lambda = 75 \text{ gm./cm.}^2$ was used. This shows that the numbers of mesons observed is of the magnitude expected : no particular significance is attached to the ratio of $1\frac{1}{2}$.

Since equilibrium between mesons and stars seems to be established for depths below 225 gm./cm.^2 ice, we should expect the angular distribution of π -mesons to be constant at these depths. We are therefore justified

Fig. 4.



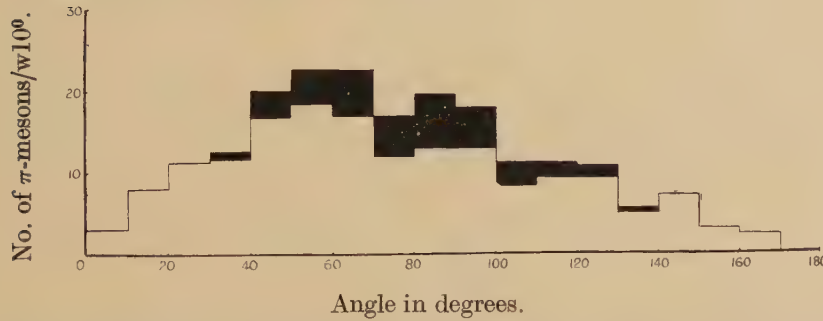
in classing together mesons at all these depths when considering the angular distribution of mesons arriving at the plate. This distribution is shown in fig. 5 in which a correction has been applied (shaded histogram) for loss of steeply dipping tracks. It is seen that approximately one-third of all π -mesons were travelling in an upward direction when coming to rest in the emulsion. Unfortunately, complete data on the angular distribution at production of mesons have not been published. Brown *et al.* (1949) have shown that at 3550 m. in showers of more than five particles 93 per cent of the shower particles (the majority of which are mesons with energies above 60 MeV.) are directed downwards and nearly obey a $\cos \theta \sin \theta d\theta$ distribution. We may assume the lower

energy mesons to be isotropic. From an analysis of stars formed at 70,000 ft. Perkins (private communication) concludes that in light elements about 10 per cent of shower particles travel backwards with respect to the incident star producing radiation. Due to the angular distribution about the zenith of the meson producing radiation (which is likely to be more collimated than the total star producing radiation since higher energy events are involved), the percentage of upward travelling shower particles at production will exceed 10 per cent. A liberal estimate of this percentage would be 20 per cent. We make the following assumption about the angular distribution of mesons at production and will then calculate the expected ratio of the numbers of mesons coming to rest after travelling in an upward cone of 60° to the number of those coming to rest after travelling in a downward cone of 60° .

Assume :—

- (a) Mesons of energy below 60 MeV. are produced isotropically in the laboratory system. These form 12 per cent of the total number of mesons.

Fig. 5.



Angle in degrees.

Angular distribution of π -mesons. Shaded areas represent corrections for loss of steeply dipping tracks.

(b) Twenty per cent of mesons of energy greater than 60 MeV. are produced isotropically in the upper hemisphere.

(c) The remainder of the mesons are produced downward with a $\cos \theta$ distribution per unit solid angle.

Consider one meson produced in the upward 60° cone and one in the downward 60° cone due to group (a) mesons. Then it can be shown that there will be three mesons produced in the upward cone due to class (b) mesons and 18 in the downward cone due to class (c) mesons. With these assumptions we find that four mesons are produced in an upward cone to 19 in the downward cone. However, the downward moving mesons, being produced with higher average energies have longer ranges (electronic stopping) than the upward moving mesons. Therefore they should stand more chance of being lost through nuclear interactions

(for $\lambda = 75$ gm./cm.²). Taking this into account, in a calculation somewhat similar to the above, it is deduced that one slow meson should be observed in the upward cone for every 3·6 in the downward cone. The experimental figure is $1 : 2\cdot7 \pm 0\cdot6$.

The calculations have been carried through on the assumption that mesons travel in straight lines. We have seen that the Coulomb scattering of μ -mesons is small (~ 4 per cent are back-scattered) and the scattering of π -mesons is expected to be of the same order. We therefore conclude that for the given assumptions concerning the angular distribution at production of π -mesons, the observed ratio of the upward to downward flux of π -mesons is not significantly different from the expected ratio. If, however, the results of further experiments should show that π -mesons are more strongly collimated than has been assumed above, then the observed upward flux would suggest that nuclear scattering of π -mesons is an important process. Indeed, preliminary results of Bernadini *et al.* 1950, suggest that π -mesons are scattered in flight through angles of greater than 30° with a cross-section of about one-quarter of the geometrical value. Scattering of this magnitude would lead to almost perfect agreement between the observed and calculated upward flux of π -mesons.

ACKNOWLEDGMENTS.

I should like to express my thanks to Professor Sir George Thomson for guidance during the course of this work and to Dr. E. P. George for an interesting discussion concerning the upward stream of π -mesons.

REFERENCES.

- BRADNER, H., 1949, *Review of Work on Artificially produced mesons* (Berkeley).
- BERNADINI, *et al.*, 1950, *Phys. Rev.*, **80**, 924.
- BROWN, *et al.*, 1949, *Phil. Mag.*, **40**, 862.
- CAMERINI, *et al.*, 1950, *Phil. Mag.*, **41**, 413.
- GEORGE, and EVANS, 1950, *Proc. Phys. Soc. A*, **63**, 1248.
- HARLING, LATTIMORE, LI, and PERKINS, 1949 a, *Nature, Lond.*, **163**, 319.
- HARLING, and PERKINS, 1949 b, *Nature, Lond.*, **164**, 285.
- KRAUSHAAR, W. L., 1949, *Phys. Rev.*, **76**, 1045.
- LATTES, OCCHIALINI and POWELL, 1947, *Nature, Lond.*, **169**, 486.
- ROSSI, B., 1948, *Rev. Mod. Phys.*, **20**, 537.
- SANDS, M., 1950, *Phys. Rev.*, **77**, 180.

LXIX. CORRESPONDENCE.

Meson Production in the Atmosphere.

By J. D. PULLAR and E. G. DYMOND,

Department of Natural Philosophy, University of Edinburgh*.

[Received March 12, 1951.]

THE variation with altitude of the vertical intensity of the penetrating component of cosmic radiation has been measured in a series of balloon flights from Edinburgh, geomagnetic latitude 59° N. A telescope, ABC, of three counters with 8 cm. of lead absorber was used, giving a ground rate of 57.4 ± 0.7 counts per hour. Radio transmission of the counts during flights and of the air pressure record, gave the necessary data. Particular attention has been paid to accuracy of pressure measurement, since the important information is obtained at the lowest pressures. A minimum pressure of 4 mb. (maximum altitude of 124,000 ft.) was reached during these flights.

Curve 1 shows the mean result of seven flights with identical equipments. The intensity, extrapolated to zero pressure, is 23 times the ground value. Pomerantz (1949) has published a similar curve, deduced from a single flight at $\lambda 52^{\circ}$ N. and with 7.5 cm. Pb. His curve, when normalized to ours at the ground, agrees within statistical error at the top of the atmosphere, but is some 25 per cent lower between 200 and 50 mb. At 27 mb. Schein, Jesse and Wollan (1941) found an increase of 16 times over ground rate, which is considerably lower than our result. Lack of published detail, however, prevents accurate comparison with our work.

The counter arrangement ABC measures not only the flux of mesons and primary particles able to penetrate 8 cm. Pb., but also electron showers coming in from the side. The influence of these was measured in two further flights, by counting the fourfold coincidences between counters ABCD. The results are shown in Curve 2. At the lowest pressure of 12 mb. the number of showers is rising very steeply and amounts to 20 per cent of the threefold rate ABC.

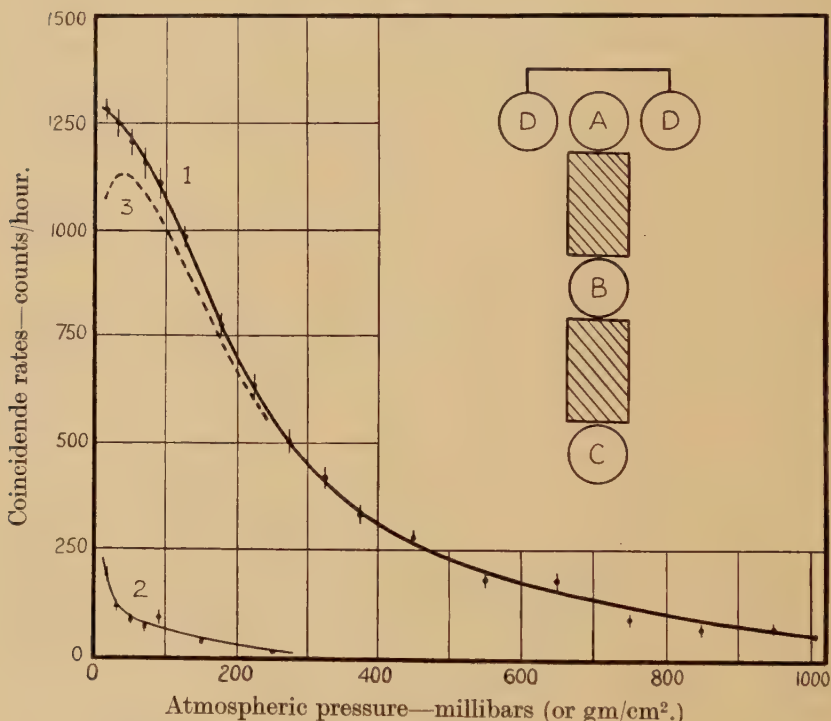
Electronic showers arriving at large angles to the zenith are to be expected at very low pressures. Such showers reach maximum development after traversing 100 gm./cm.^2 of the atmosphere. Measured horizontally the atmosphere has this thickness at a point where the pressure is 2.5 mb., thus the horizontal showers will increase in importance until this value of the pressure is reached. It is of course possible for the fourfold coincidence system ABCD to respond also to vertical showers containing at least one penetrating particle. However, the interaction length of protons is about 70 gm./cm.^2 , so that a sharp rise in counting rate in the uppermost 20 gm./cm.^2 is not to be expected from this cause.

* Communicated by Professor N. Feather, F.R.S.

We are therefore justified in regarding Curve 2 as due to side showers only, and by subtraction from Curve 1 we get the true vertical penetrating flux in Curve 3. This shows a maximum at 35 mb., representing the production of mesons by particles of the primary beam. The agreement of our uncorrected curve with that of Pomerantz (who gave reasons for ignoring the shower correction) appears to be fortuitous.

Extrapolation of Curve 3 back to zero pressure in order to determine the flux of primary penetrating particles remains doubtful until more accurate values of the lateral shower correction are available in the pressure range below 10 mb. Further work is in progress in this direction.

Fig. 1.



Curve 1 : Coincidence rate of ABC.

Curve 2 : Coincidence rate of ABCD (lateral showers).

Curve 3 : Difference of 1 and 2, giving true vertical rate.

REFERENCES.

POMERANTZ, M.A., 1949, *Phys. Rev.*, **75**, 69.

SCHEIN, M., JESSE, W. P., and WOLLAN, E. O., 1941, *Phys. Rev.*, **59**, 615.

Cross-section for the Reaction ${}^9\text{Be}(p, p2n){}^7\text{Be}$ at 156 MeV.

By T. C. RANDLE, J. M. DICKSON and J. M. CASSELS,
Atomic Energy Research Establishment, Harwell*.

[Received March 22, 1951.]

In the course of some experiments to measure neutron production cross-sections a "sandwich" target containing two thick sheets of beryllium and three thin sheets of carbon was bombarded with 171 MeV. protons. The γ -ray activities induced in both the target elements have since been followed for 104 days, using a Geiger counter and a standard geometrical arrangement.

As usual (Dickson and Randle 1950, 1951), the radiation from the carbon part of the target quickly become characteristic of ${}^7\text{Be}$. The cross-section for the formation of this nucleus from carbon is $11.0 \pm 1.0 \times 10^{-27} \text{ cm}^2$. at the effective proton energy of 156 MeV.

The activity of the beryllium part of the target could be analysed into two components, with half-lives of 10 days and 53 days respectively. The first component, which was much the weaker of the two, must have been due to an unidentified impurity. The second component was identified as ${}^7\text{Be}$, which has a half-life of 52.9 days. This assignment was confirmed by investigating the γ -ray energy spectrum 57 days after bombardment, using a scintillation γ -ray spectrometer (Hofstadter and McIntyre 1950). Mr. R. B. Owen, to whom we are indebted for this measurement, reported a single γ -ray energy of 0.48 MeV. The γ -rays emitted in the decay of ${}^7\text{Be}$ have an energy of 0.485 MeV.

A comparison of the activities of the two parts of the target showed that the ratio of the ${}^9\text{Be}(p, 2n){}^7\text{Be}$ cross-section to the ${}^{12}\text{C}(p, 3p3n){}^7\text{Be}$ cross-section is 0.84 ± 0.04 at the effective proton energy of 156 MeV. The ${}^9\text{Be}(p, p2n){}^7\text{Be}$ cross-section is therefore $9.2 \pm 0.9 \times 10^{-27} \text{ cm}^2$.

One of us (J.M.D.) intends to investigate the excitation curve for this reaction, which should prove useful for monitoring high energy proton bombardments of beryllium targets.

We should like to thank Dr. A. Blainey for providing us with the beryllium targets.

REFERENCES.

- DICKSON, J. M., and RANDLE, T. C., 1950, *Nature, Lond.*, **166**, 235.
DICKSON, J. M., and RANDLE, T. C., 1951, Submitted to *Proc. Phys. Soc. A*.
HOFSTADTER, R., and MCINTYRE, J. A., 1950, *Phys. Rev.*, **80**, 631.

* Communicated by the Authors.

The Reactions $^{11}B(\gamma\alpha)^7Li$ and $^{11}B(\gamma T)^8Be$.

By MARGARET E. CALCRAFT and E. W. TITTERTON,
Atomic Energy Research Establishment, Harwell †.

[Received March 16, 1951.]

As a result of experiments with the A.E.R.E. synchrotron, Goward, Titterton and Wilkins (1950) gave evidence for the reaction



and found that at least some of the events observed involved a two-stage process

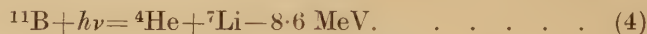


the intermediate nucleus 8Be being formed in the well known 3 MeV. state.

Recent observation of the photodisintegration of Lithium-7 into a triton and an alpha-particle (Titterton 1950) suggests the alternative disintegration scheme



In the case where the 7Li is left in its ground state a two-particle event would result according to the reaction



instead of the three-particle stars of equations (1), (2) and (3). The reaction (4) has not been previously observed.

To obtain information about these possible modes of disintegration Boron loaded E_1 emulsions have been exposed to Lithium gamma-rays from the 440 KeV. ($\gamma\gamma$) resonance. Controlled under-development by the temperature method was employed to achieve discrimination between the distintegration products of reaction (4) if present.

Although the experiment is still in progress and the statistics are poor certain conclusions emerge which are worth reporting at this stage.

First, there is definite evidence for reaction (4) which is identified by the techniques discussed by Titterton (1950). A photomicrograph of one event is given in fig. 1 and the cross-section at 17.6 MeV. is estimated to be 2×10^{-28} cm.². Twelve events have been observed, one of which is due to the 14.8 MeV. γ -rays.

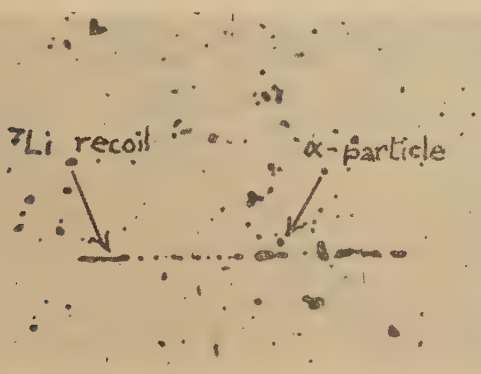
Second, among the 750 three-particle stars which have been observed 50 have been identified as resulting from reaction (1). The usual methods of the momentum and energy balance not only settle the assignment but enable a decision to be made as to which of the three particles is the triton. This is important in attempting to decide between reaction mechanisms indicated by (2) and (3).

† Communicated by the Authors.

Of the 50 events six result from the 14.8 MeV. and 44 from the 17.6 MeV. γ -ray. The cross-section for the reaction at 17.6 MeV. calculated in terms of the $^{12}\text{C}(\gamma, 3\alpha)$ cross-section given by Wäffler and Younis (1949) is $(0.6 \pm 0.3) \times 10^{-28}$ cm.².

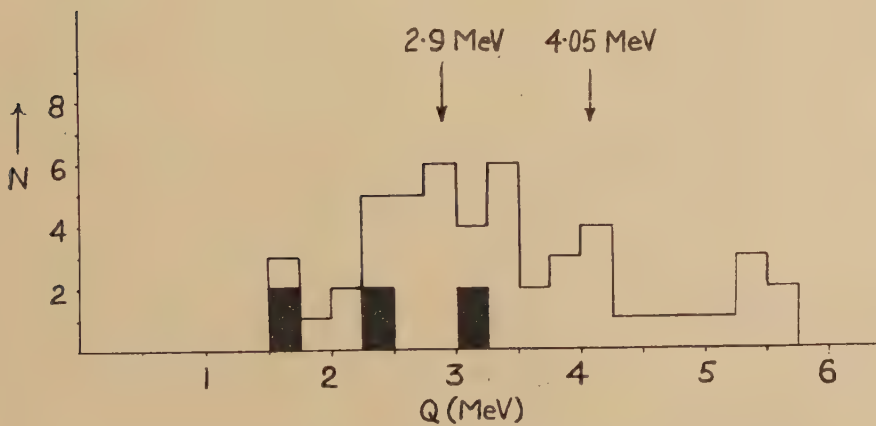
Assuming all events to result according to the mechanism of equation (2) the Q of the break up of the recoiling ^8Be nucleus is calculated in each case and the result plotted in fig. 2. The histogram suggests two broad

Fig. 1.

Photomicrograph of event due to reaction $^{11}\text{B}(\gamma, \alpha)^7\text{Li}$.

Observer : Miss M. Hart.

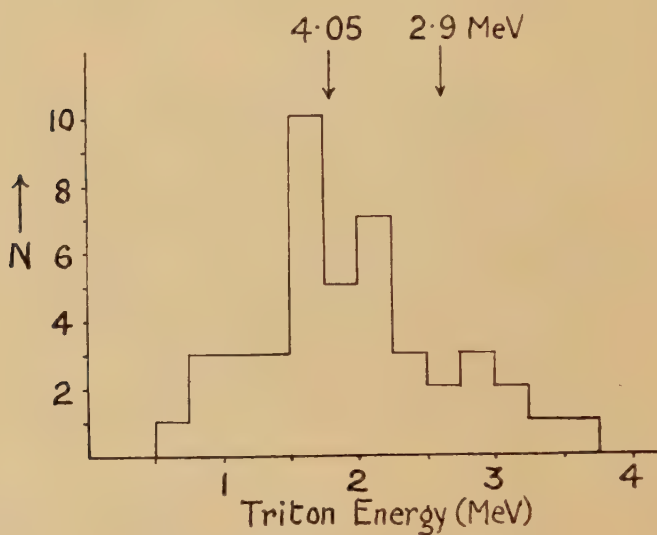
Fig. 2.

Q Value histogram. 6 blacked-out events due to 14.8 MeV. γ -ray as distinct from the others.

unresolved ^8Be levels which can be identified as the well known 2.9 MeV. level and a level at about 4 MeV., evidence for which has been given by Green and Gibson (1949). There is no known level of ^8Be corresponding

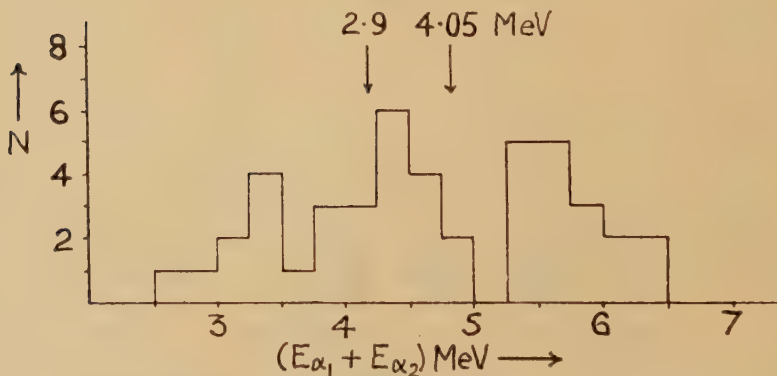
to the small group at 5.5 MeV. In the case of the 2.9 and 4 MeV. levels the appropriate energy of a triton emitted at 90° to the incoming γ -ray and the energy of the corresponding α -particle pair can be calculated from the conservation conditions for the 17.6 MeV. γ -ray. The values obtained are indicated on the histograms given in figs. 3 and 4 which

Fig. 3.



Energy spectrum of emitted tritons.

Fig. 4.

Energy spectrum of α -particle pairs following triton emission.

show the triton energy distribution and the energy distribution of the corresponding pairs of alpha-particles for events due to the 17.6 MeV. γ -ray. In each case the observed distribution is consistent with the presence of events arising from the 2.9 and 4.05 MeV. levels. The groups

are not resolved but the distributions are consistent with the known resolution of the emulsion for low energy particles (Titterton and Brinkley 1949) and the spread due to the angular distribution of the triton relative to the incoming γ -ray, provided this is not markedly anisotropic.

The 2.9 MeV. level of ^8Be is well known and has been much discussed; the 4 MeV. level was observed by Green and Gibson in experiments on the neutrons from the reaction⁷ $\text{Li}(dn)^8\text{Be}$ but they were unable to estimate the width of the state. However, as the only γ -ray observed in the experiments of Bennett *et al.* (1941 and 1947) had an energy of 4.9 MeV. and the corresponding neutron group was observed by Green and Gibson it is reasonable to suppose that the 4 MeV. level leads to a pair of α -particles as indicated by the present experiment and has a width similar to the 2.9 MeV. level. The 4 MeV. level would then have even angular momentum or even parity or both.

The mechanism indicated by equation (3) has been considered in a similar fashion. The known ^7Li level at 7.38 MeV. which breaks up into a triton and an α -particle can be excluded immediately since none of the events show a low energy α -particle as would be necessary from the energetics of the reaction. The question then arises whether there is a lower level of ^7Li which disintegrates by triton emission. The analysis is complicated by the fact that the first α -particle to be emitted is not known and each α -particle must be considered in turn. Two Q values relating to the break-up of ^7Li into a triton and an α -particle (second stage of reaction (3)) are found for each event one of which is correct and the other incorrect. A histogram similar to fig. 2 plotted with the results should show a peak superimposed on a background if a level of ^7Li is involved. In fact, no such peak is observed and the experiment indicates that at least 85 per cent of the events proceed through the mechanism of equation (2).

This result is consistent with recently published level schemes (Hornyak, Lauritsen, Morrison and Fowler 1950) for the mirror pair ^7Li and ^7Be neither of which has a level between the low lying γ -ray emitting states and the states at 7.38 and 7.02 MeV. respectively which are known to be unstable to α -emission.

Our thanks are due to Miss E. M. Chellingworth and Miss M. Hart for microscope work and to Professor O. R. Frisch and Dr. D. H. Wilkinson for permission to use the Cavendish Laboratory H.T. set.

REFERENCES.

- BENNETT, BONNER, RICHARDS, and WATT, 1941, *Phys. Rev.*, **59**, 904; 1947, *Ibid.*, **71**, 11.
- GOWARD, TITTERTON, and WILKINS, 1950, *Proc. Phys. Soc. A*, **63**, 172.
- GREEN, and GIBSON, 1949, *Proc. Phys. Soc. A*, **62**, 407.
- HORNYAK, LAURITSEN, MORRISON, and FOWLER, 1950, *Rev. Mod. Phys.*, **22**, 291.
- TITTERTON, 1950, *Proc. Phys. Soc. A*, **63**, 915.
- TITTERTON, and BRINKLEY, 1949, *A.E.R.E. Report G/R* 326.
- WAFFLER, and YOUNIS, 1949, *Helv. Phys. Act.*, **22**, 614.

Observation of Growth of Cadmium Iodine from Aqueous Solution.

By A. J. FORTY,
H. H. Wills Physics Laboratory, University of Bristol *.

[Received April 23, 1951.]

[Plate XXI.]

ACCORDING to the ideas of F. C. Frank (1949, 1950; see also N. F. Mott 1949), the growth of crystals from vapour or solution can occur by two mechanisms. At high degrees of supersaturation (greater than about 50 per cent), successive growth layers can be added to a perfect flat surface; but for lower values, the free energy of surface nucleation is too high to permit this. At low supersaturation growth can only occur on surfaces where one or more screw dislocations terminate; and the step-lines between growth layers should form spirals ending on the dislocations. Such patterns of monolayer step-lines have been observed by Griffin (1950) on prism faces of natural beryl crystals, using an optical microscope, and on paraffin crystals grown from solution by Dawson and Vand (1951), using the electron microscope.

The appearance of certain faces of cadmium iodide crystals shown in the I.C.I. film on "Crystal Growth" (Bunn and Emmett 1949) suggests that, in addition to these monomolecular steps, steps of much greater height are formed. At present unpublished work by Verma and the author independently, suggests the same thing for carborundum; these steps also form spirals. The spirals must end on a group of dislocations all of the same sign, the total strength or Burger's vector of the groups being considerable.

This letter records a series of photographs (Pl. XXI.) (taken with an optical metallurgical microscope) of the actual growth of a cadmium iodide crystal from aqueous solution, and shows the successive stages in the formation of the growth patterns of this type.

Flakes of cadmium iodide were added to a drop of distilled water on a heated microscope slide until the solution was just under-saturated at 60° C. Rapid crystallization around the edges of a cover slip placed over the drop formed a closed cell. The solution became slightly supersaturated as it cooled, and the growing crystal faces were examined in reflection with an ordinary metallurgical microscope. Step visibility was considerably improved by using a narrow illuminating pencil of light.

A large number of small tabular crystals (about 100 microns across) were observed to grow quickly from the supersaturated solution, usually with the (0001) face parallel to the cover slip. Most of the faces exhibited patterns of diffuse concentric steps and the growth centres could not be

* Communicated by the Author.

Fig. 1.

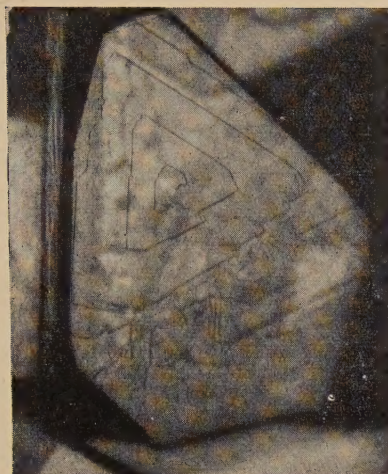


Fig. 2.

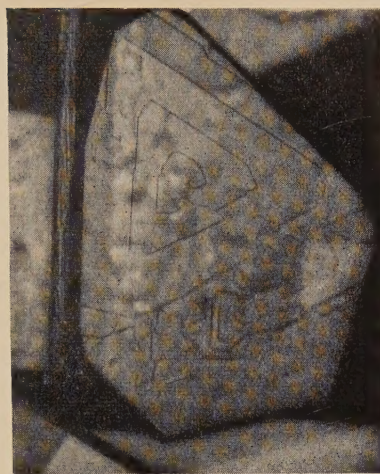


Fig. 3.

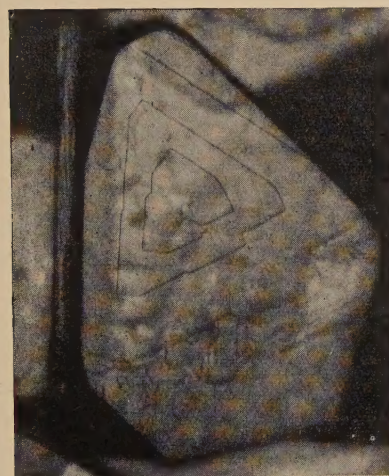


Fig. 4.



Fig. 5.



Figs. 1-5. (600 \times) taken at 60 min. intervals, showing the upward growth of (0001) face of cadmium iodide crystal.

resolved clearly. In some regions of the solution, however, where the supersaturation was probably lower, giving a slower uniform growth, polyhedral layers were observed. The step-lines between these were sharp and sufficiently spaced for resolution of the growth centres, all of which showed patterns based on dislocation systems. A single screw dislocation dominating the growth of a crystal face produced the familiar rotation spiral of step-line attached to it. A pair of screw dislocations of opposite hand, sufficiently close together to form a growing terrace, cooperated to produce a closed-loop pattern. Growth from two dislocations of the same hand gave a pattern of two parallel spirals, while growth from a system of three dislocations (two of one hand and one of the other) was indicated by a closed-loop pattern dominated by a single spiral. More complicated growth patterns have been observed from centres of many dislocations. On some very thin crystal plates, spirals have been observed on both surfaces with their origins one vertically above the other. This shows how a screw dislocation persists through the crystal layer lattice, producing a self-perpetuating step on both faces of the plate as it emerges.

This "spiral growth" of the crystals is observed both for unpurified cadmium iodide and recrystallized cadmium iodide. In all cases, thin hexagonal or triangular plates grow rapidly from the supersaturated solution, and then a number of growth centres appear suddenly, to commence growth in thickness. Usually the growing face is dominated by one or two of the centres.

It is likely that the lateral growth of the plates takes place by two-dimensional nucleation, from a high supersaturation, on the less closely packed ($10\bar{1}0$) of the hexagonal structure. This quickly lowers the effective supersaturation and further growth can only occur by the dislocation mechanism. F. C. Frank (1951) has suggested that the non-uniform distribution of impurities is sufficient to self-stress the thin plates beyond the theoretical yield stress. Buckling, followed by slip, produces the dislocation groups which have large screw components terminating in the (0001) face; the crystal plate now grows in thickness from a low supersaturation.

Photographs 1-5 are part of a sequence taken during the development of a particular crystal face. The step-lines have high visibility and show the trigonal character of the growth layers. The photographs illustrate the outward growth of the natural terrace between a pair of screw dislocations dominating the face, until a closed-loop and a new terrace are generated. The cycle is repeated indefinitely, and the step-lines move outwards in closed-loops as the face develops upwards at the rate of one layer thickness per cycle. The growth of faces dominated by other dislocation systems has been recorded similarly.

By illuminating the microscope with parallel monochromatic light, Fizeau fringes have been produced across this crystal face due to reflections from the glass-solution and solution-crystal surfaces. The thickness of

the growth layers has been calculated to be $750 \text{ \AA.} \pm 100 \text{ \AA.}$ from the fringe displacement across the step-lines ; the steps are big and this accounts for their high visibility.

As already indicated, this is not the growth of a crystal face from a pair of simple screw dislocations having unit Burger's vector, generating unimolecular layers (these would have thickness 6.84 \AA. according to the X-ray data of Bozorth (1922)) as in the case of monolayer growth on beryl. The growth must be initiated from a pair of "dislocation groups", each having a total Burger's vector with a component normal to the face of about 110 thicknesses of the minimum layer. The two groups cooperate to send out single growth layers $750 \text{ \AA.} \pm 100 \text{ \AA.}$ thick. Theoretically a dislocation group can exist of any total strength (*i. e.* any Burger's vector normal to the face) and promote growth in layers of corresponding thickness.

The two dislocation groups are not quite equal in strength and a small step corresponding to their difference extends outwards from the centre, crossing the main loops. At each crossing, the height of the main steps and consequently their rate of advance, changes abruptly, producing a characteristic sequence of pronounced kinks in the loops. Similar rows of kinks are observed in spirals on carborundum which grows in a like manner; cadmium iodide can be used as a model for this type of growth.

A further paper will give a more detailed account of these observations, with evidence that cadmium iodide crystals, like carborundum, can be polytypic.

ACKNOWLEDGMENTS.

I should like to thank Dr. F. C. Frank for his interest in this work and for invaluable discussion. I am grateful for a grant from the Department of Scientific and Industrial Research.

REFERENCES.

- BOZORTH, P. M., 1922, *J. Amer. Chem. Soc.*, **44**, 2232.
- BUNN, C. W., and EMMETT, H., 1949, *Discussion of Faraday Soc.*, **5**, 119 ; and "Crystal Growth", film, shown by I.C.I.
- DAWSON, I. M., and VAND, V., 1951, *Nature, Lond.*, **167**, 476.
- FRANK, F. C., 1949 a, *Discussion of Faraday Soc.*, **5**, 48 ; 1949 b, *Ibid.*, **67** ; 1950, *Phil. Mag.*, **41**, 200 ; 1951, to be published in *Phil. Mag.*
- GRIFFIN, L. J., 1950, *Phil. Mag.*, **41**, 196.
- MOTT, N. F., 1950, *Nature, Lond.*, **165**, 295.
- VERMA, A. R., 1951, to be published in *Phil. Mag.*.